Chapter 3

Results and Discussions

This chapter presents the results and the discussion of the present study. The discussion involving the experimental works will includes the comparison with the numerical simulation. Both of aerodynamics and thermal behaviors will be included. Firstly, the details on the inlet flow behavior have been clarified included the blade profile investigation. The advantage of the CFD simulation enables the prediction of flow structures especially at the region where could not be obtained by the experimental.

3.1 Blade profile verification

The blade profile was verified by determined the static pressure loss on blade PS and blade SS as shown in Figure 38. The loss profile based on the EFD is compared to the CFD for the validation. The loss pick on the blade SS is parallel to the position of blade throat. Predicted loss profile almost in good agreement with the EFD except near the blade TE on blade PS. The difficulty in providing a measurement holes at this small area only allowed a few data can be taken. Furthermore, complexity of the flow due to the wake profile near the blade TE also the reason could be considered.

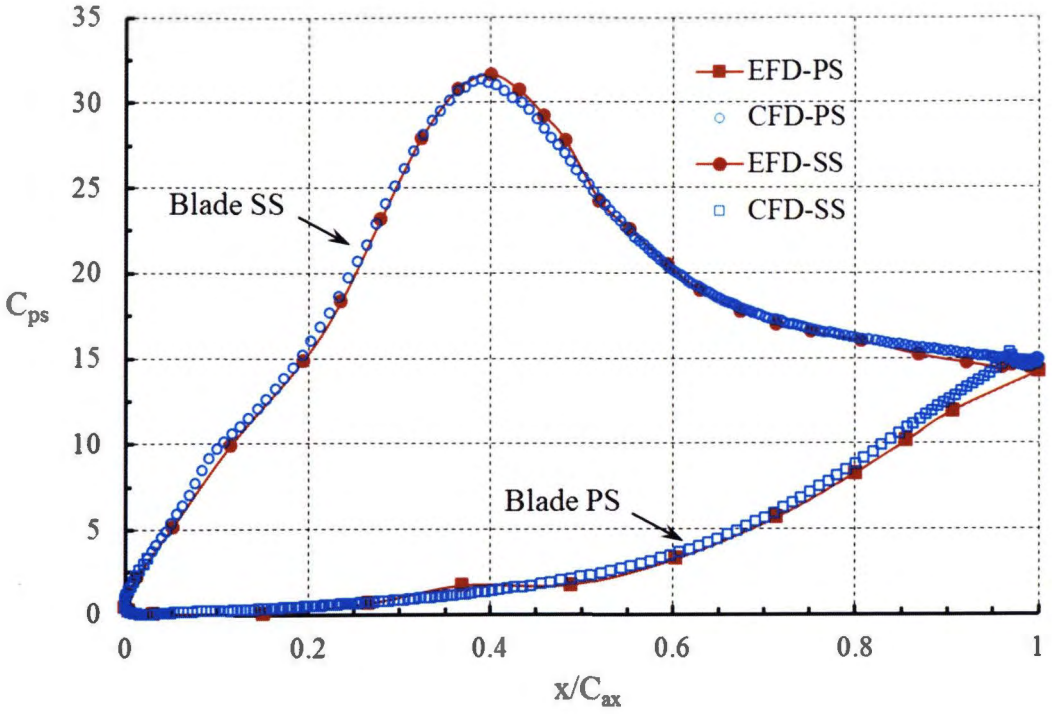

Figure 38 Static pressure loss coefficient on blade midspan

3.2 Inlet flow behavior

A new wind tunnel has been developed to investigate the effect of the leakage. This section will discuss on the inlet flow behavior in order to ensure the uniform flow structure is entering the cascade. Figure 39 illustrates the inlet axial velocity contour for the region from the endwall towards midspan (presented by normalized-span height, z/s) while Figure 40 showing the flow deviation contours (yaw angle). The red vertical dashed-lines in both figures show the position of the blade LE. The figures also indicate the contours for 2.4 pitches duration where the probe was traversed through 3 blades LE in pitchwise direction. Due to the unavailability of the device, the closer region measured at endwall side is approximately, z/s=0.02. The presence of the cascade located to downstream of the measurement plane influenced the incoming V_{ax} as presented in Figure 39. The lower flow velocity was obtained at the region close to the blade LE due to the flow turning influenced by the blockage due to the higher pressure in stagnation region. The higher V_{ax} regions indicates by yellow located closer to the blade PS at y/p=0 ~ 0.3, 0.65~1.3 and 1.75~2.3. In contrast, the lower V_{ax} closer to the blade SS was due to the higher flow deviation as

illustrates in Figure 39. The ununiformed of the flow in pitchwise direction was captured on the left side of Figure 40 at region y/p=0~0.3 with a slightly higher flow deviation was due to the closer distance from the sidewall of the test section which influenced to the flow disturbance. The normalized axial velocity distributions in pitchwise and spanwise direction are shown in Figure 41 and Figure 42, respectively. In addition, the inlet velocity was compared to the profile based on CFD in Figure 42. The thicker boundary layer thickness for EFD is approximately z/s=0.1 (10mm) compared to the CFD which is approximately z/s=0.03 (3.5mm).

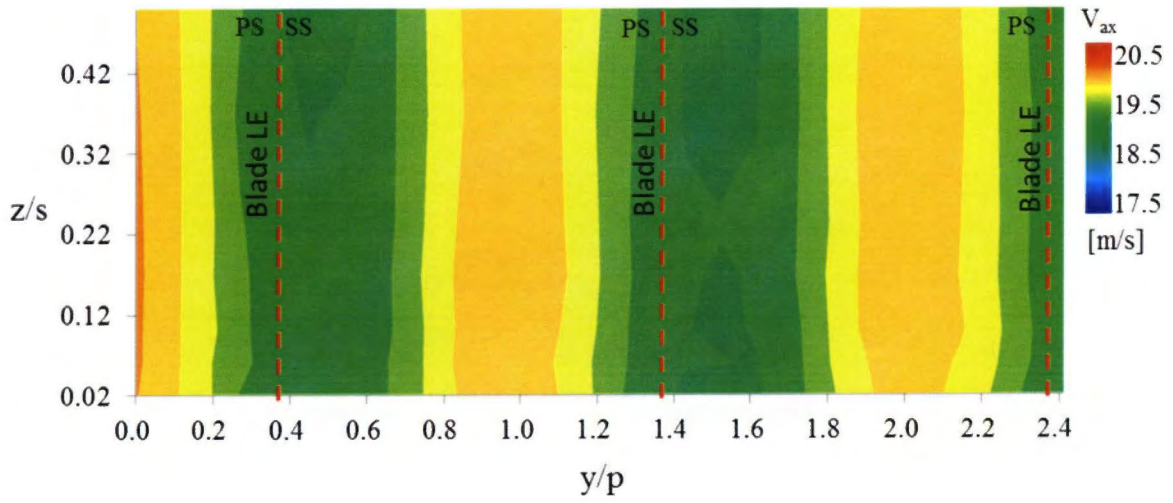

Figure 39 Inlet axial velocity

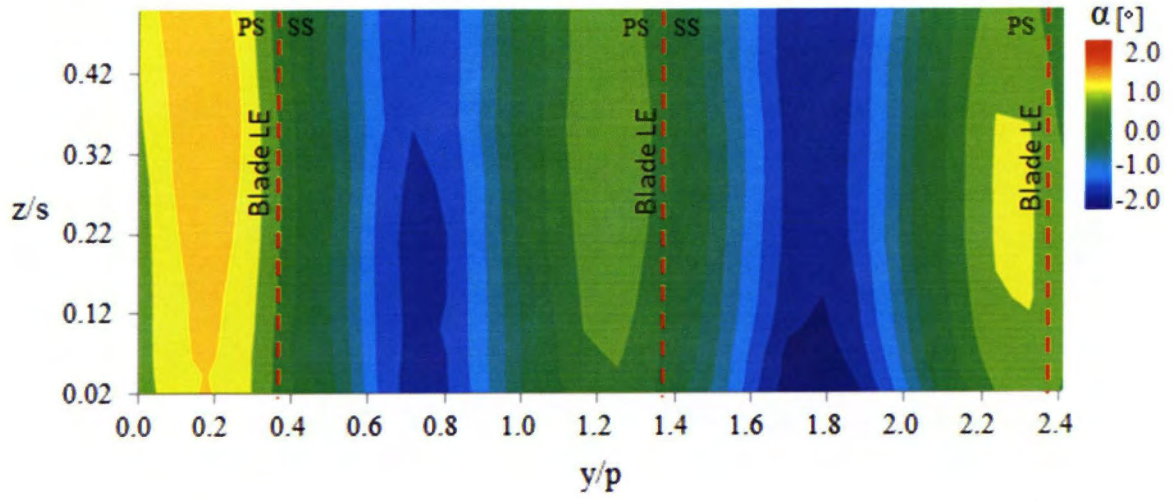

Figure 40 Inlet yaw angle, α

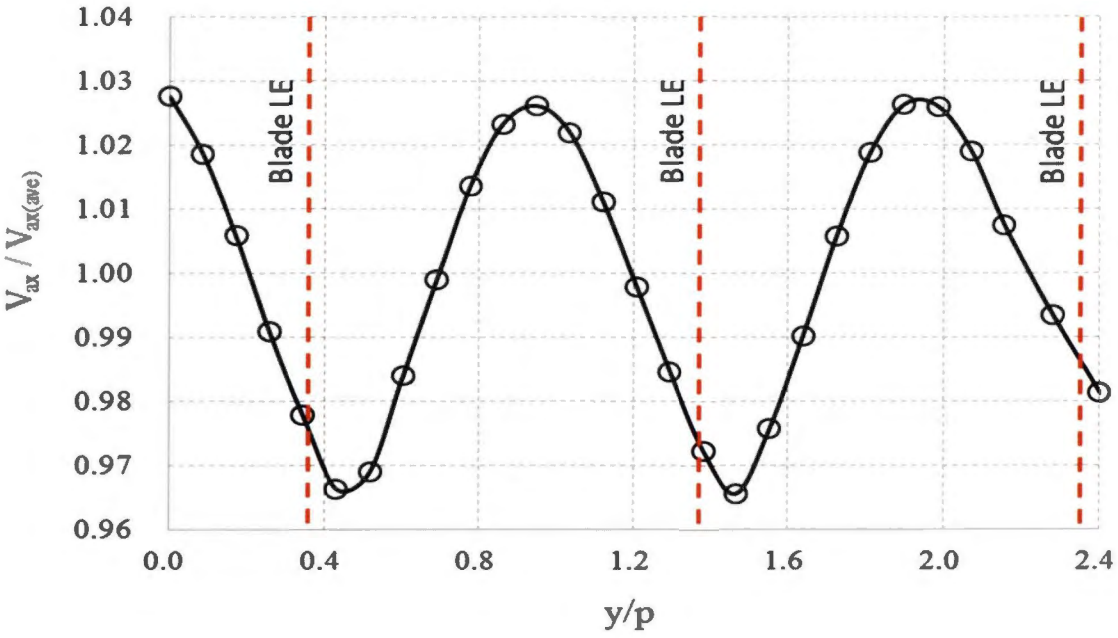

Figure 41 Pitchwise direction normalized inlet axial velocity (span –averaged)

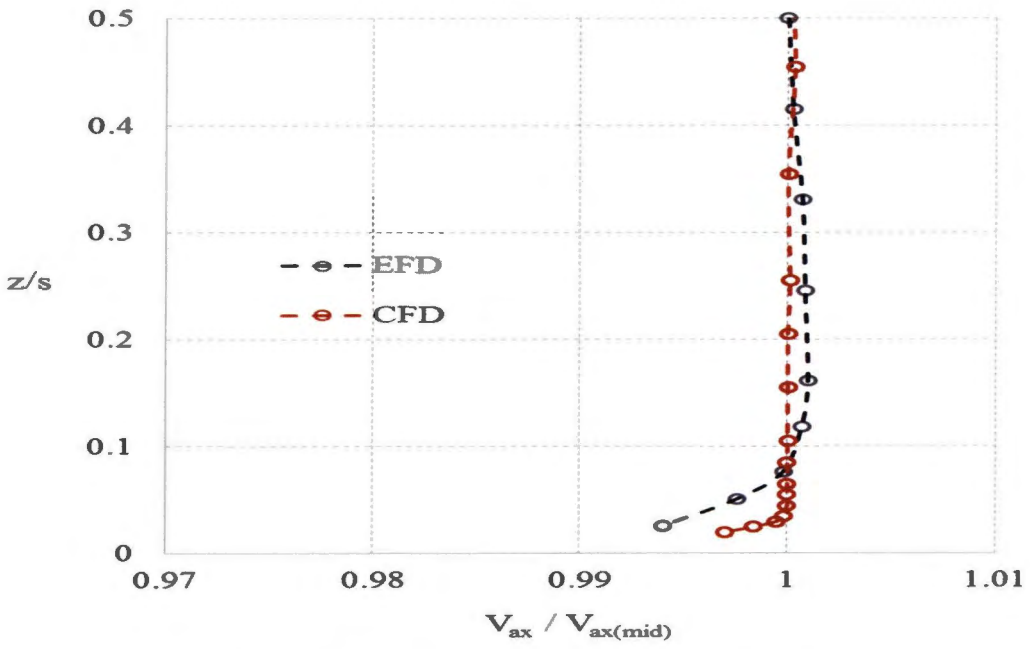

Figure 42 Spanwise direction normalized inlet axial velocity (pitch-averaged)

3.3 Aerodynamics performances at blade downstream

3.3.1 Baseline flow performance (without leakage flow)

The flow at plane $1.25C_{ax}$ has been revealed by conducting the 5-holes probe measurement which enables the three-dimensional flows measuring. The details on the baseline case need to be firstly discussed thus the flow behavior affected by the leakage flow injection could be clearly being observed and compared. Figure 43 presents the total pressure loss coefficients, C_{pt} with secondary velocity vector plotted, vorticity, ζ and secondary kinetic energy coefficient, C_{SKE} in (a), (b) and (c) respectively, for the baseline case obtained by the EFD. The vertical axis of the contour represents the normalized spanwise direction while the horizontal axis is normalized pitchwise direction. The contour in spanwise direction starting from endwall, z/s=0.02 and ended at blade midspan, z/s=0.5. Noted that the nearest position of probe towards endwall is approximately 2 mm which means z/s=0.02. Figure 43 (a) shows the losses contributed by the wake profile which occurs along the spanwise direction in the region of y/p=0.35~0.5. In addition, the contours also characterized by the presence of the passage vortex represented by the first loss core centralized at y/p=0.48 and z/s=0.1. The second loss core also can be seen close to the endwall at y\p=0.38~0.42 which is considered associated with the interaction between boundary layer, wake profile and the corner vortex. The ζ contour plotted at the same plane in Figure 43 (b) explains the cause of the loss which is associated with the passage vortex consists of three ζ regions. The first region indicates in red located at y/p=0.4~0.6 and z/s=0.08~0.12 rotating in anti-clockwise direction. The second ζ region rotating in clockwise direction located at the bottom side of the first region. The flow direction due to these ζ is parallel with the secondary velocity vector plotted in Figure 43 (a). The third ζ region captured close to the endwall region could be considered as the corner vortex rotating in anti-clockwise direction. The magnitude of the rotational energy influenced by the secondary flows describes by C_{SKE} as presented in Figure 43 (c). The appearance of C_{SKE} region as captured in the figure is parallel to the position of the passage vortex which is presented in ζ contour in Figure 43 (b). Thus the contour explains the energy produces by the passage vortex for baseline case.

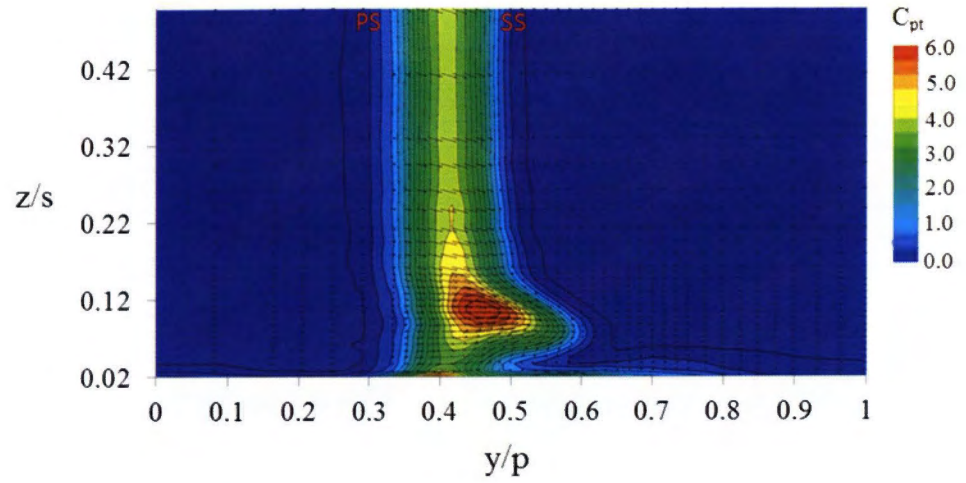

(a) C_{pt}

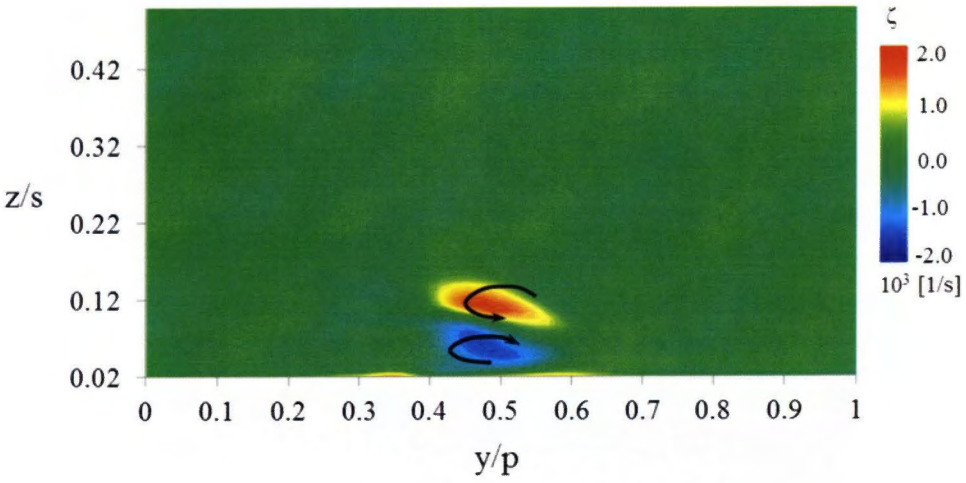

(b) ζ

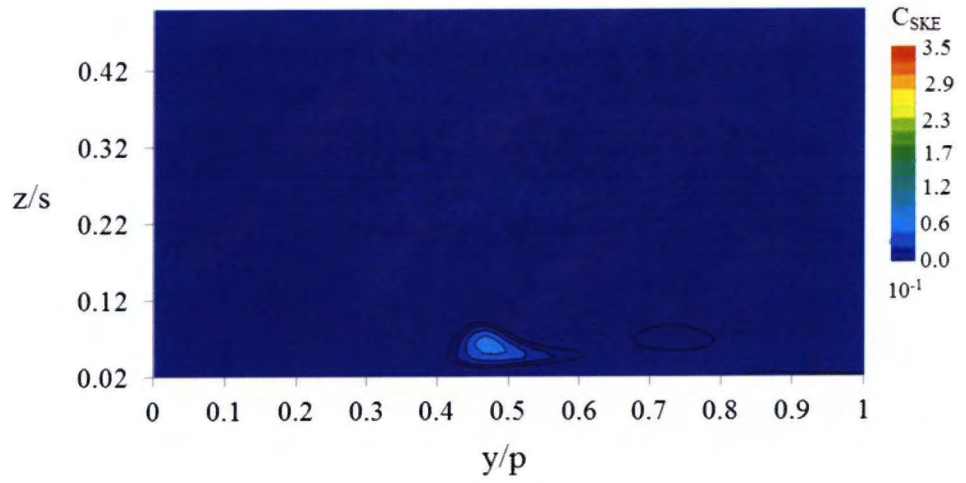

(c) C_{SKE}

Figure 43 Flow behavior at Plane $1.25C_{ax}$ -Baseline case

3.3.2 Leakage flow injection effects

The effects of the leakage flow from the slot which is located -0.63C_{ax} upstream of the blade LE has been investigated by four different injection amounts. The leakage flow amount represented by MFR were ejected approximately 0.75% , 1.25%, 1.75% and 2.25% to describe the case for lower, intermediate, higher and extremely higher ejection. The same contours as discussed in previous section are plotted in Figure 44~Figure 47 for MFR =0.75%, 1.25%, 1.75% and 2.25%, respectively. According to those figures, there are three significant changes has been recognized compared to Figure 43 (a). Firstly, at a lower MFR of 0.75% presented in Figure 44 (a), the shape of the first loss core seems to be slightly changed. As shown in Figure 44 (b), the flow ζ indicated by the blue region which is rotating in clockwise direction increased its strength which might be one of the reasons of the change. However, the position of this core did not show any significant change. Secondly, the second loss core which is located at y/p=0.4 also slightly increased the region. However, the ζ contour as be shown in Figure 44 (b) did not show any significant change in term of the magnitude or region compared to the baseline case. The third change is the most significant effect could be observed when the leakage flow being injected even tough at lower MFR. The additional lost core region on the blade SS side located at y/p=0.55~0.87 and z/s=0.02~0.05 has been captured. Indeed, the additional loss region was likely occurred close to the endwall side. The secondary flow structure was being affected by the leakage flow ejection consequently contributes the additional loss near the blade downstream. This has been proved by the appearance of the newly vorticity contour near this region with a lower strength, see Figure 44 (b). The discussion above is mainly concentrates on the effect of leakage flow on lower injection case. The effects by the different amount of leakage injection was also been revealed.

Figures indicate that the upstream leakage ejection has a significant influence on the secondary flow structures across the MFR value. Increased the MFR from 0.75% to 1.25% did not give a significant effect on the first loss core in term of shape, see Figure 45 (a) but its position slightly shifted towards midspan. This phenomenon could clearly be seen when the MFR continuously be increased to 1.75% and 2.25%, see Figure 46 (a) and Figure 47 (a). The first loss core were shifted from z/s=0.10 to 0.13 for MFR=1.75% as shown in Figure 46 (a) and leakage injection with 2.25% presents the highest position among others approximately z/s=0.15, see Figure 47 (a). This might be considering that the leakage flow injection from

the upstream of the blade LE caused the increase strength of the horse-shoe vortex (HSV) especially on the pressure-side leg horse-shoe vortex (PS-HSV). As a result, the PS-HSV had a higher fluid momentum compared to lower leakage injection or baseline cases to cross the mainstream flow from the blade PS to neighboring blade SS. Finally it developed as a passage vortex near blade TE. At the corner between blade SS and endwall, the passage vortex is expected to be lifted-off the blade surface with a higher position in spanwise direction by the higher fluid momentum thus presenting higher position of the loss core at blade downstream compared to a lower MFR injection. This is parallel to the suggestion made by Sharma and Butler [7]. In addition, not only the position, but also the shape of the loss core seems to be continuously changed. The transformation of the loss core shape can clearly observed at higher MFR of 1.75% and 2.25%. This core tends to change especially on the blade SS where it became oblongated towards pitchwise direction. For the second loss core, the region (red core) in Figure 47 (a) for 2.25% injection became wider in pitchwise direction and the region was expanded approximately from y/p=0.38~0.42 to y/p=0.38~0.55. The loss region became wider was due to the increase strength of the flow ζ near this region as shown by the ζ contours in Figure 44 (b) ~Figure 47 (b). As the MFR being increased, the strength of the corner vortex has been amplified which then contributed to the higher losses. This phenomenon could also influences to the blockage which might be considered to deflect the earlier flow direction slightly upwards. The higher position of first loss core at higher MFR also might be the result from this phenomenon.

The third loss core which was only be captured in the leakage ejection cases also continuously expended the region when the MFR increases. The third loss region which is localized on the blade SS side expanded almost half of the blade pitch for the extremely higher injection in Figure 47 (a). Furthermore, compared to lower injection case, this loss core likely to be lifted-up toward midspan as the same phenomenon has been captured on the first core. As discussed previously, the newly generated flow ζ at this region was being considered to responsible for the additional losses. Since the strength of the ζ in this region is increased when the MFR increases, see Figure 45 (b) ~ Figure 47 (b), the wider loss region was obtained. Additionally, higher strength flow ζ can easily penetrates into mainstream thus resulting higher position in spanwise direction. The increased strength of flow ζ near this region is also clearly be captured by the secondary velocity vector plotted which is centralized at y/p=0.76 and z/s=0.06, see Figure 47 (a). The formation of the vortical

structure in this region explains a significant effects influenced by the leakage flow where the strength of the passage vortex was amplified. Based on Figure 44 (c) ~ Figure 47 (c), C_{SKE} contours are parallel with the above explanation where the increased strength of the passage vortex also can be seen by the increases of the secondary flow energy. As expected, MFR=2.25% provides the highest C_{SKE} magnitude compared to a lower MFR or baseline case. In this case, higher C_{SKE} consequently increase the passage loss associated by the secondary flows.

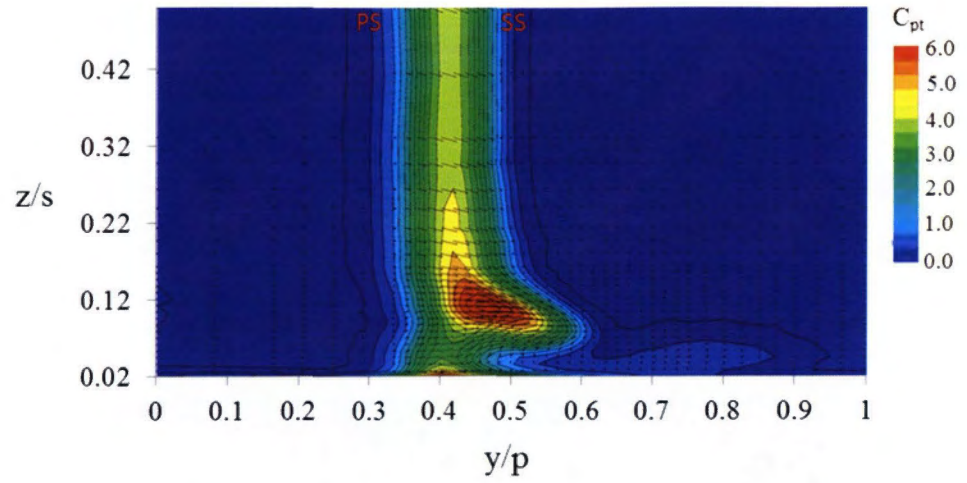

(a)C_{pt}

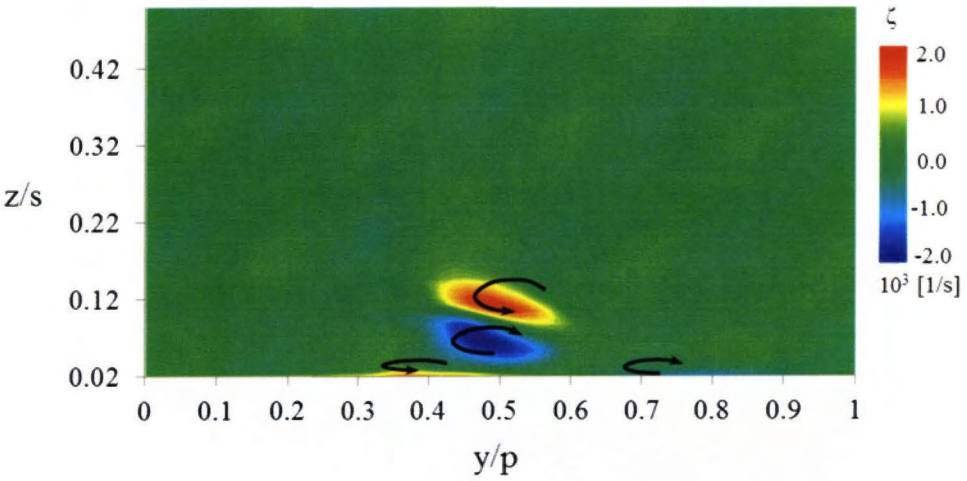

(b) ζ

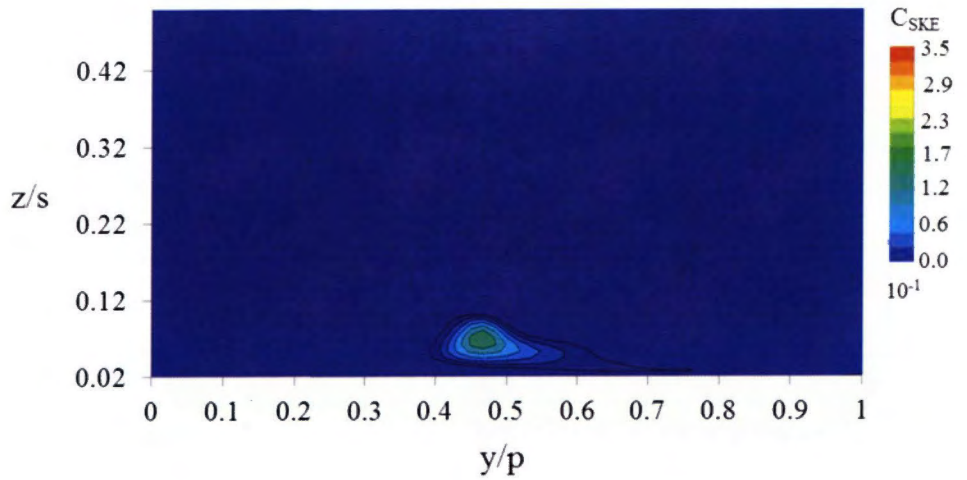

(c)C_{SKE}

Figure 44 Flow behaviour at Plane 1.25C_{ax}-MFR=0.75%

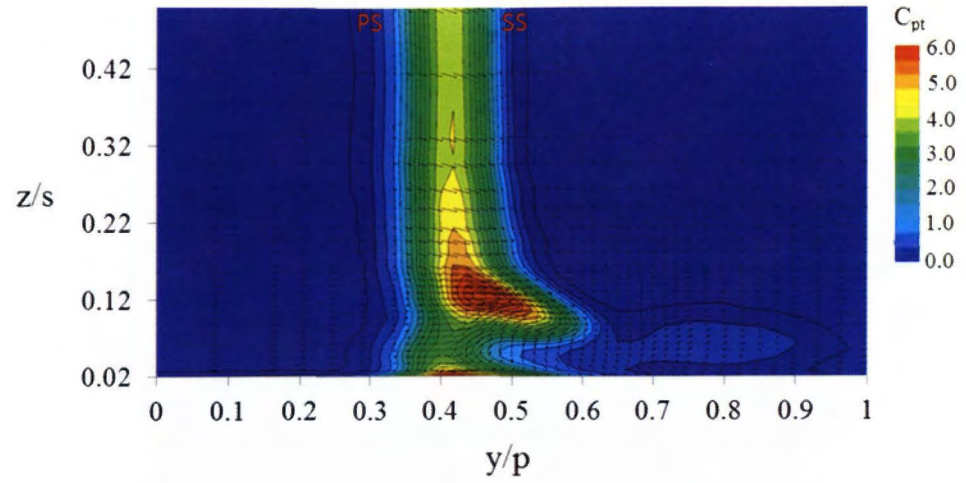

(a)C_{pt}

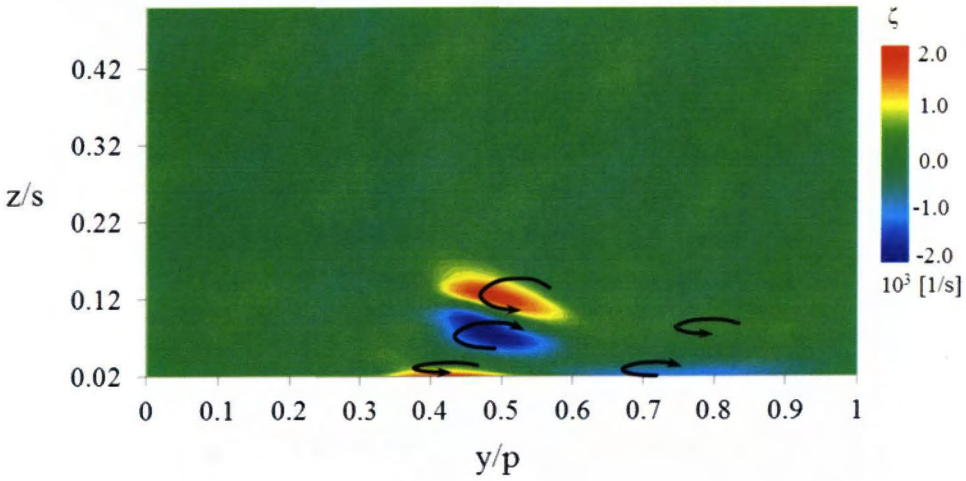

(b) ζ

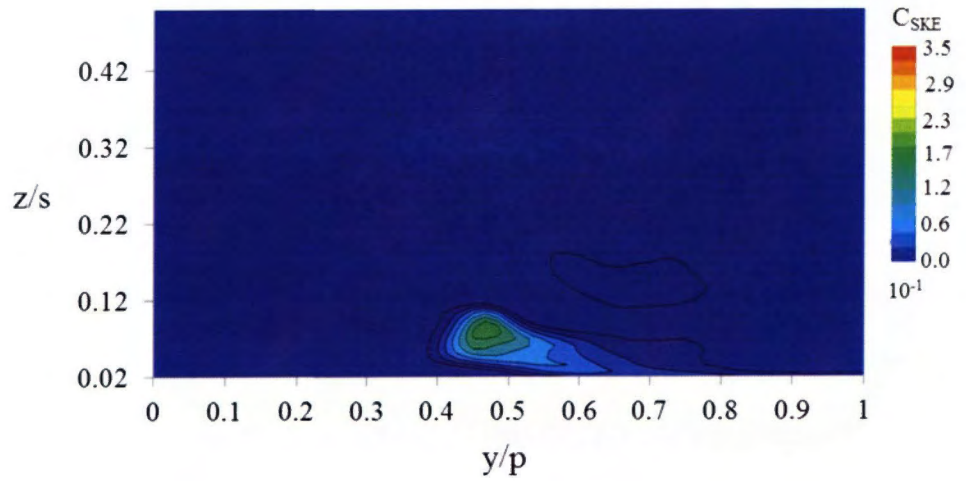

(c)C_{SKE}

Figure 45 Flow behaviour at Plane 1.25C_{ax}-MFR=1.25%

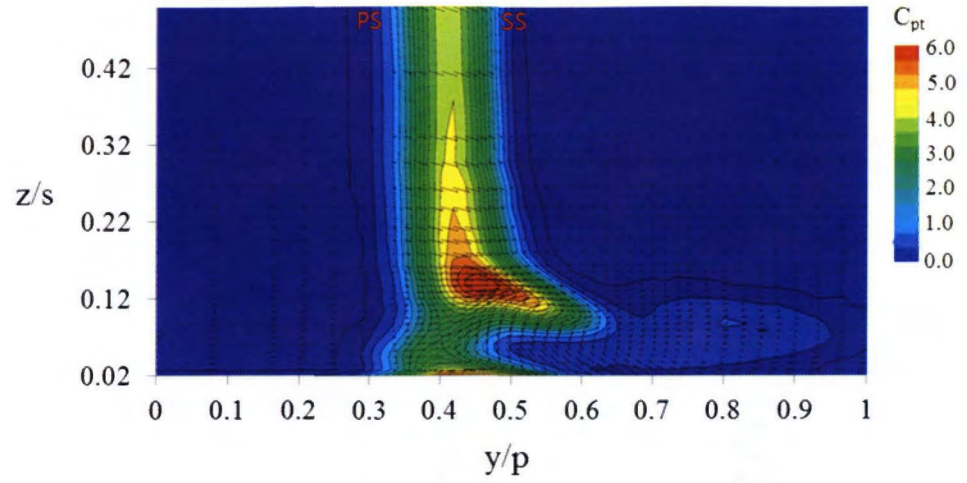

(a)C_{pt}

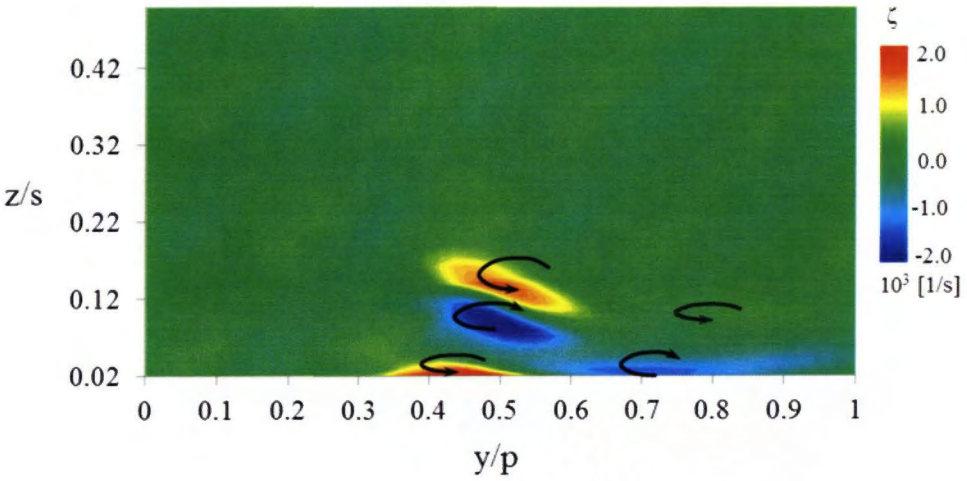

(b) ζ

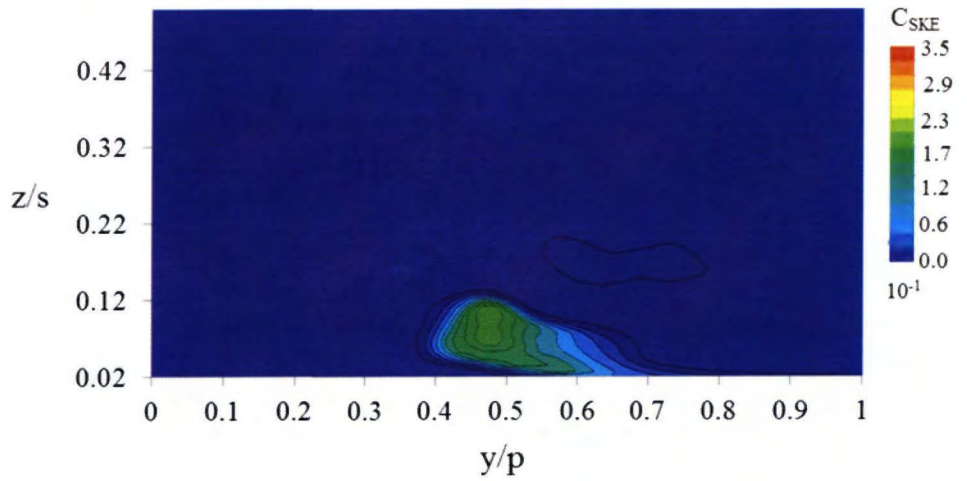

(c)C_{SKE}

Figure 46 Flow behaviour at Plane 1.25C_{ax} -MFR=1.75%

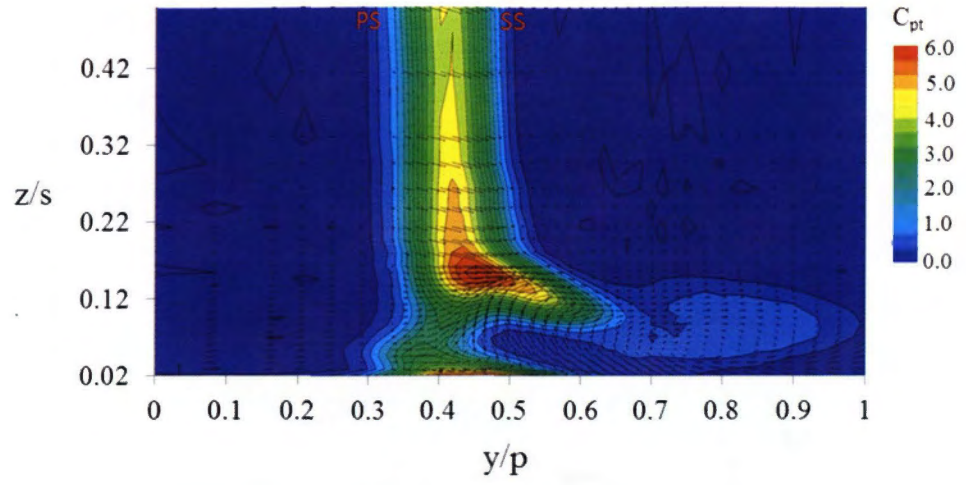

(a)C_{pt}

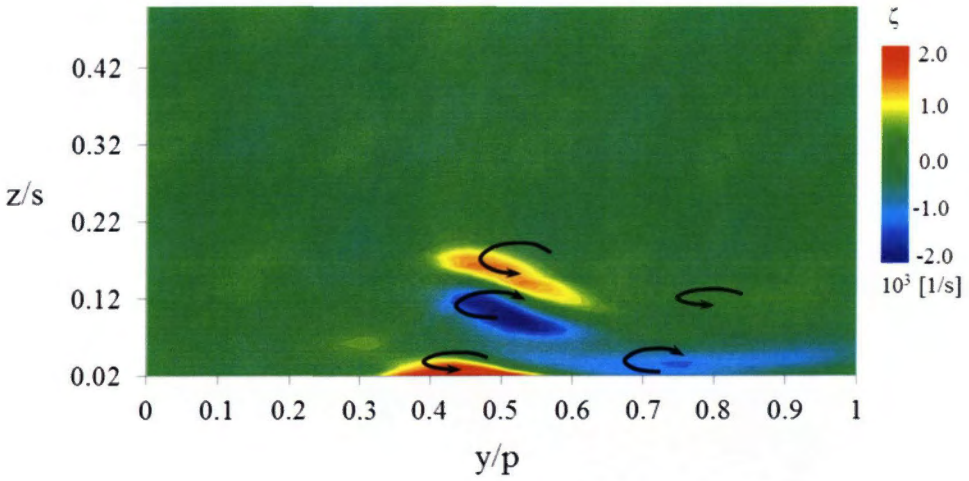

(b) ζ

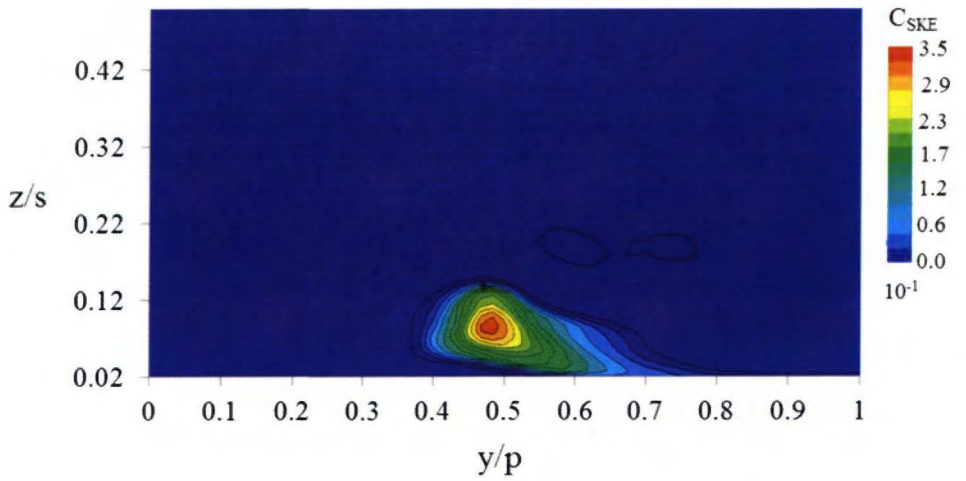

(c) C_{SKE}

Figure 47 Flow behaviour at Plane $1.25C_{ax}$ -MFR=2.25%

Normalized spanwise direction of $C_{pt}/C_{pt(mid)}$ and flow deviation at the same plane are plotted in Figure 48, by determining the average on pitchwise direction of each data. The graph illustrates the comparison between the leakage injections with the baseline case presented by the red line in (a) C_{pt} and (b) yaw angle, α. As be shown in Figure 48 (a), the $C_{pt}/C_{pt(mid)}$ =1 is actually belongs to the loss associated by the wake profile and for $C_{pt}/C_{pt(mid)}$ >1 can be considered as the loss associated by the secondary flows. For the baseline case, the loss influenced by the secondary flows can be observed from z/s=0.02 to z/s=0.3 with the maximum $C_{pt}/C_{pt(mid)}$ =1.33 located at z/s=0.08. The loss contributed by the secondary flows in spanwise direction spread slowly from z/s=0.3 to z/s=0.4 (indicates by $C_{pt}/C_{pt(mid)}$ >1)when the leakage flow are applied. The picth-averaged C_{pt} also presents the increases trend when the MFR increases. The maximum $C_{pt}/C_{pt(mid)}$ is approximately 1.39, 1.41, 1.5 and 1.58 for MFR = 0.75%, 1.25%,1.75% and 2.25% respectively. At the same time, as the MFR increases, the position of the pick slightly shifted toward midspan. This observation is in good agreement with the C_{pt} discussion made on Figure 43~Figure 47. The introduction of the leakage flow at upstream of the blade LE is considered to increase the strength of the PS-HSV which finally influenced to the higher flow blockage in the blade passages. As a result, a high flow deviation by the higher MFR was obtained as indicated in Figure 48 (b) thus resulting higher losses.

The aerodynamics performance of upstream leakage flows can be summarized by taking the mass-averaged C_{pt} for each case as shown in Figure 49. The approximate curve has been plotted thus the trend of aerodynamics performance can be observed. The contribution of the MFR towards the C_{pt} can directly specify from the graph. Measurement indicates the C_{pt} is linearly increases as the MFR increases. Based on the trend line obtained, applying the highest MFR=2.25%, resulting the $\overline{C_{pt}}$ =1.456 which means the loss was increased approximately 14.2%. In other words, in order to increase 1% of MFR, the loss is estimated to be increased about 6.3%. Another approach also can be used to describe the trend of loss with substituting the parameters into the linear function by taking the MFR parameter into account. As a result, Eq. 28 can be used to represent the loss trend for upstream leakage injection.

$$\overline{C_{pt}} = \gamma \mathrm{MFR} + \overline{C_{pt0}} \tag{33}$$

Where,

γ, loss increase rate (=0.080)

$\overline{C_{pt0}}$, baseline mass-averaged loss (=1.275)

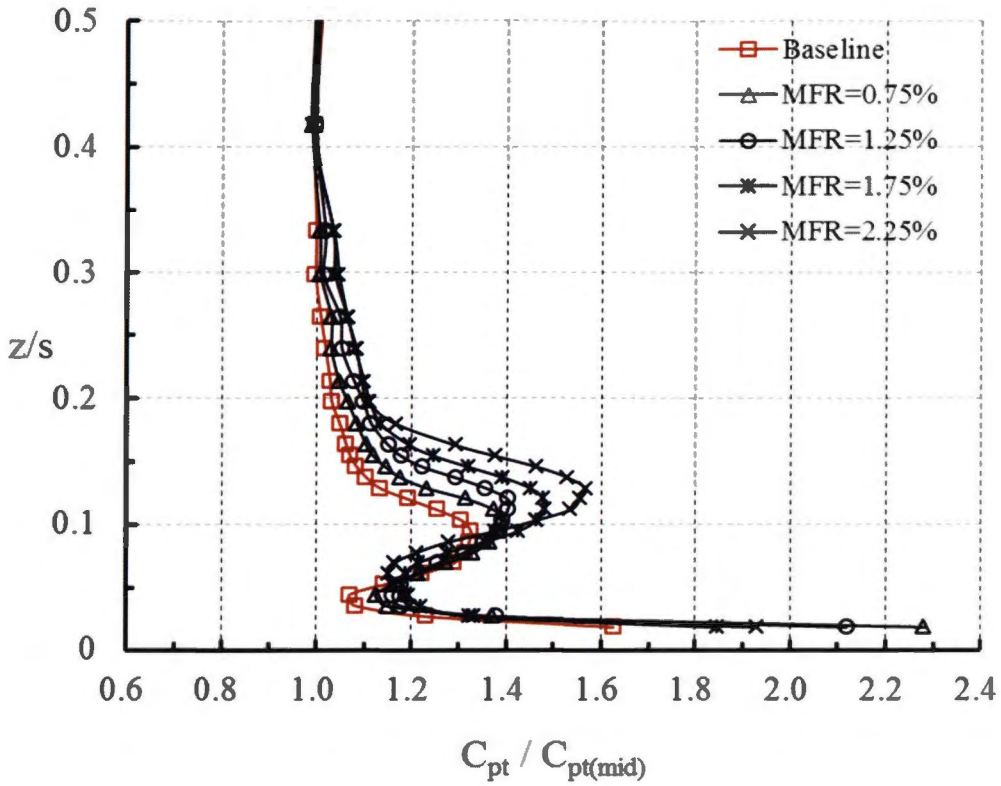

(a) Spanwise C_{pt}

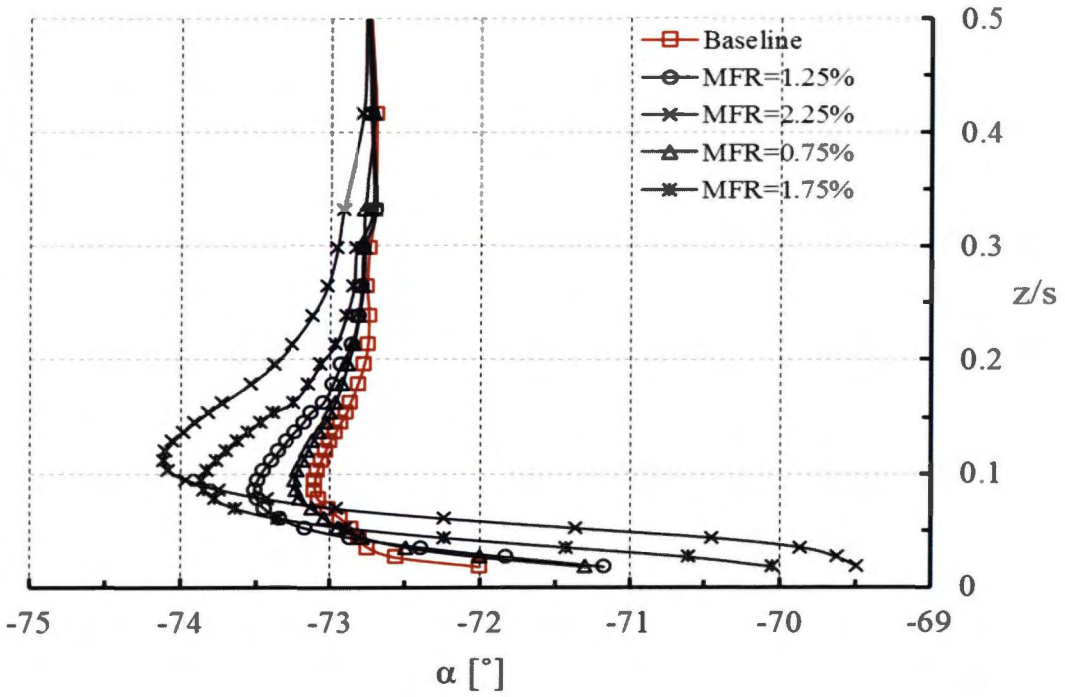

(b) Spanwise α

Figure 48 Pitch averaged C_{pt} (a) and yaw angle, α (b)

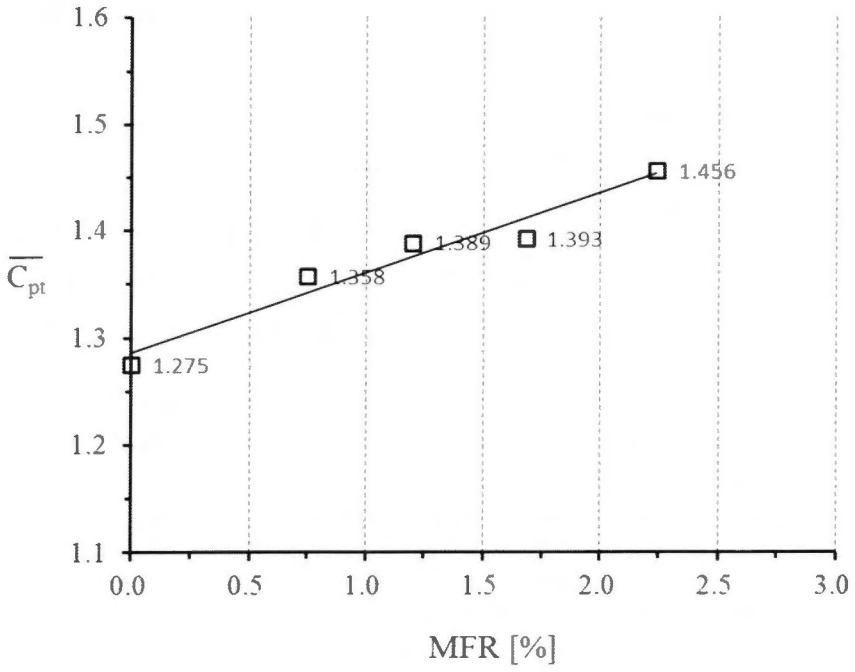

Figure 49 Trend line for mass-averaged total pressure loss at Plane $1.25C_{ax}$

3.3.3 Predicted flow behaviour at Plane $1.25C_{ax}$

The performance of numerical simulation in predicting the interaction between the leakage flow and the secondary flow on the endwall has been investigated by three cases. Firstly, the baseline case was predicted. Then it has been compared with another two injection cases; MFR=1.25% and 2.25% represent intermediate and extremely higher leakage injection. Figure 50 presents the C_{pt} contour (a), ζ (b) and C_{SKE} (c) for baseline case. The same figures are plotted for MFR=1.25% and 2.25% in Figure 51 and Figure 52. Without any leakage flow injection, Figure 50 (a) presents the loss contour for baseline case which was associated by the wake profile along the spanwise direction in the region y/p=0.3~0.5. The passage vortex was considered to be responsible to the loss core indicates with a higher loss region at y/p=0.43, z/s=0.10. As be shown in Figure 43 (a), this loss core was also be captured by the experimental. However, in comparison with the EFD, numerical simulation clearly predicted the existence of the loss core close to the endwall located at region y/p=0.35~0.5. The limitation of the measurement device to access this region caused the presence of loss core near this region was not clearly captured. In comparison to the baseline case, the loss core associated with the passage vortex can be observed to occur further away

from the wall corresponding to the MFR values. At MFR = 1.25%, see Figure 51 (a), additional loss region can be observed to occur on the blade SS. Noted that, this new loss core was also presented by the experimental as shown in Figure 45 (a). As the MFR increases, the additional loss region also increases as shown by MFR= 2.25%, see Figure 52 (a). This additional loss region was also caused by the flow vorticity which is clearly captured on the blade SS. Additionally, in comparison with the measurement, CFD also clearly captured the presence of the vortical structure illustrates by the secondary velocity vector is centralized at y/p=0.75, z/s=0.11 to present the increased strength of the passage vortex in the cascade. Higher leakage flow ejection case causes deformation on the shape of the loss core characterized by the passage vortex. The CFD results show similar trends as the EFD. Similar to the EFD, the position of the loss core predicted by CFD seems to move away from the endwall as the MFR increases. Although the similar trend can be observed, the CFD results show a discrepancy in terms of the shape and location of the loss core. The discrepancy could be contributed by the different inlet flow profile used in the CFD which influence to the development of the passage vortex. see Figure 42. With regard to the loss region characterized by the corner vortex which has been observed earlier, see Figure 51, wider loss region can be observed at higher MFR indicating the increase of the corner vortex strength. The same trend of C_{SKE} is also presented by the CFD where the increases of the secondary flow energy can be observed after the leakage injection; see Figure 51 (c). Its continuously increase when the leakage flow changed to MFR=2.25%, see Figure 52 (c). However, CFD has predicted the higher secondary flow energy compared to EFD close to endwall side which been observed after the leakage injection. This higher flow energy might be sourced by the newly generated flow vorticity near this region. Figure 53 summarizes the predicted aerodynamics performance by determine the mass-averaged C_{pt} which is compared to EFD. A similar pattern can be observed between the EFD and CFD. Having the similar trends, the losses predicted by the CFD increased approximately 14.3% for MFR= 2.25%. Thus, it could be estimated that about 6.4% of loss increases when injecting a leakage flow by MFR=1%. The prediction is very close to the EFD with 6.3% of loss per MFR. In general, the graph shows that CFD is over predicted the losses in the range of 3%~5% in comparison to EFD. Based on Eq. 33, the loss predicted by CFD can be estimated by Eq. 34.

$$\overline{C_{pt}} = 0.085\text{MFR} + 1.331 \tag{34}$$

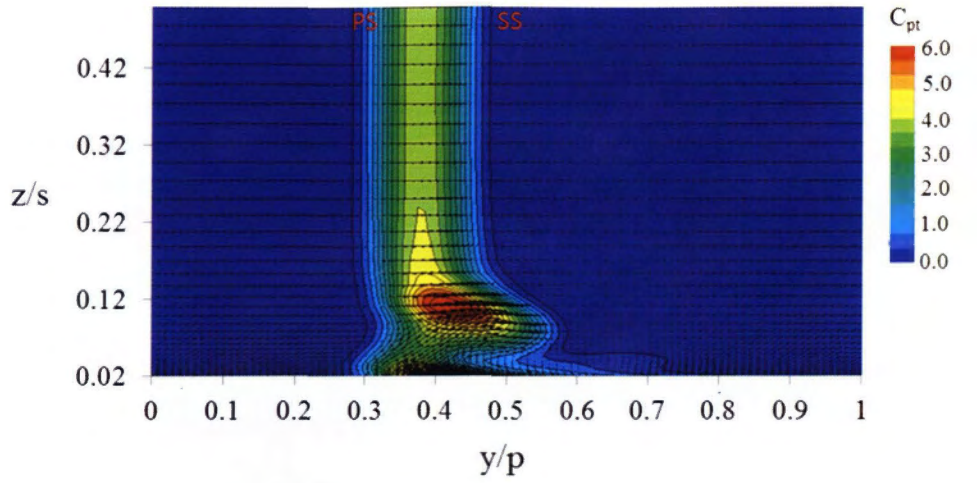

(a) C_{pt}

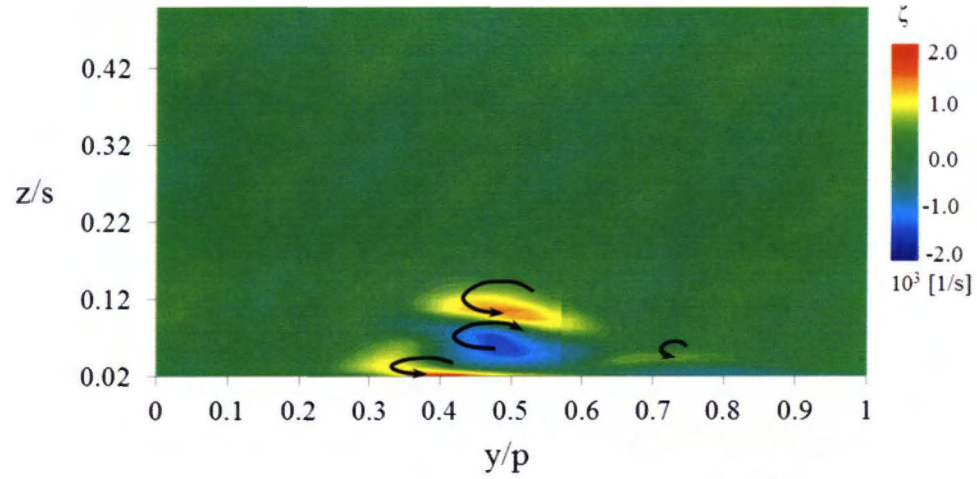

(b) ζ

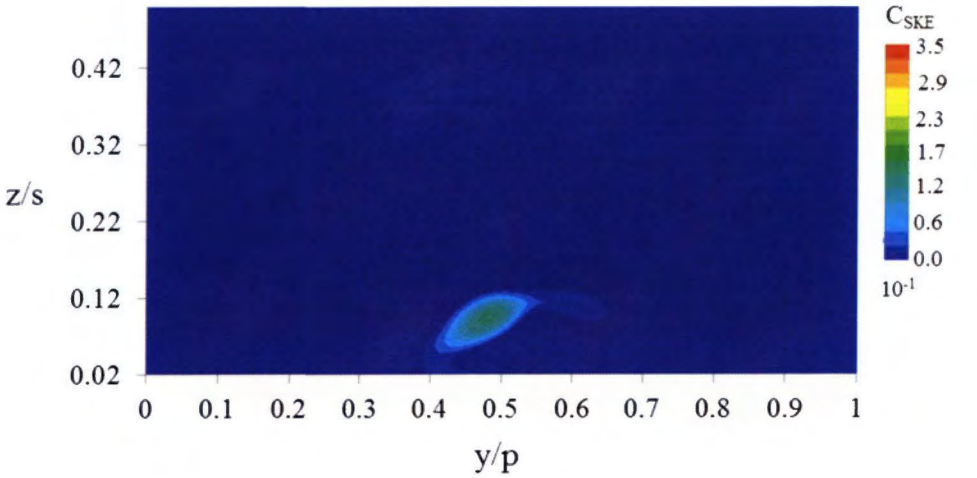

(c) C_{SKE}

Figure 50 Predicted flow behaviour- baseline case

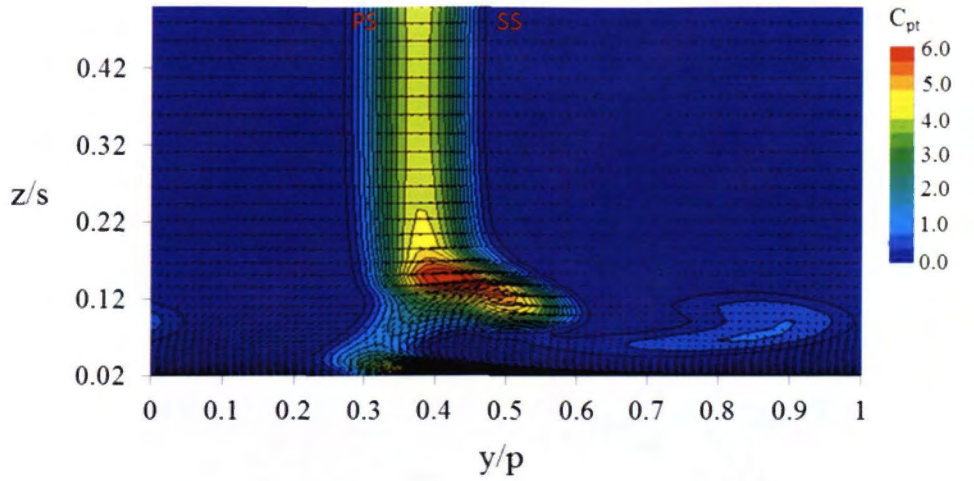

(a) C_{pt}

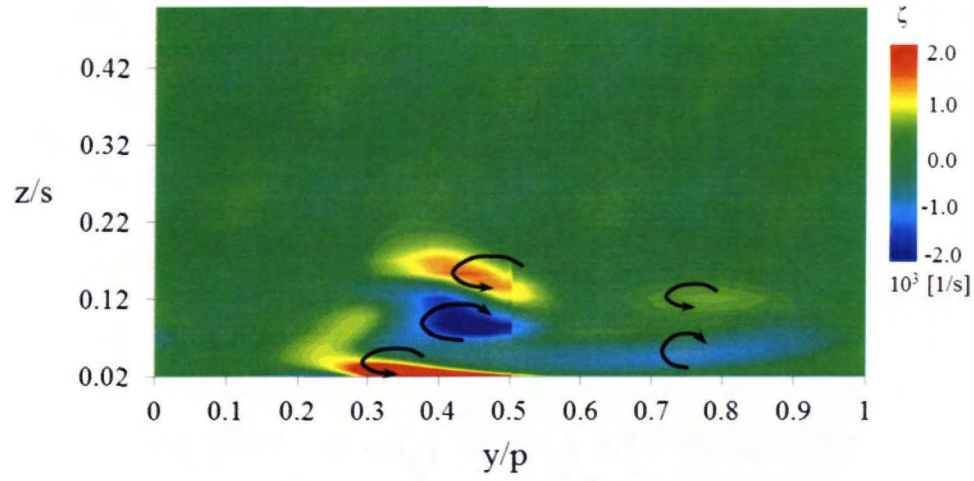

(b) ζ

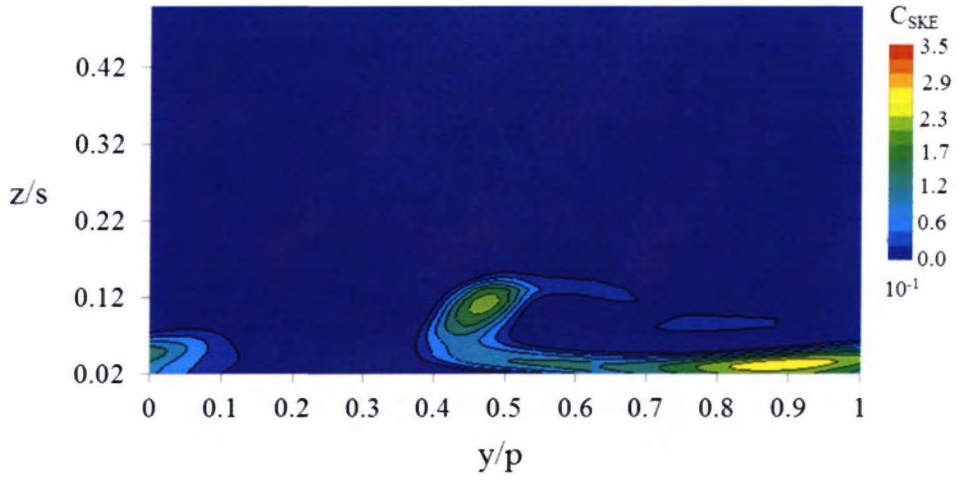

(c) C_{SKE}

Figure 51 Predicted flow behaviour-MFR = 1.25%

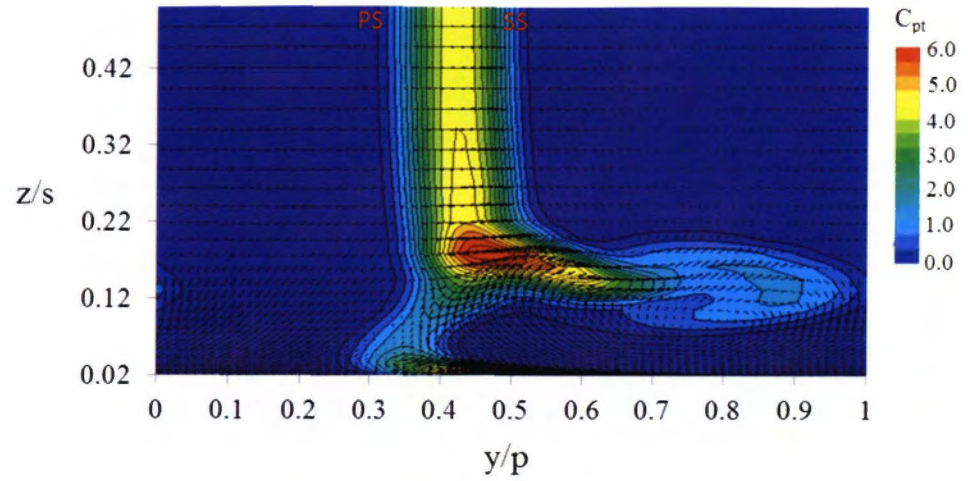

(a)C_{pt}

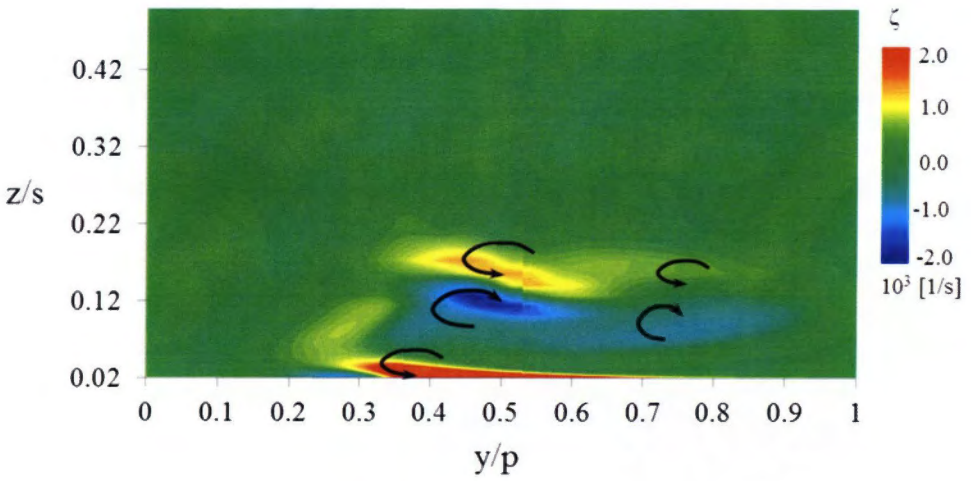

(b) ζ

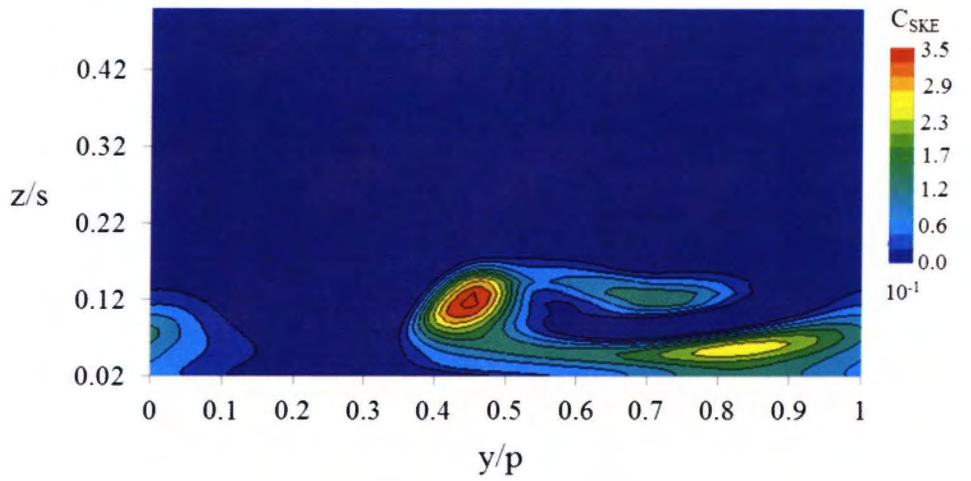

(c) C_{SKE}

Figure 52 Predicted flow behaviour-MFR=2.25%

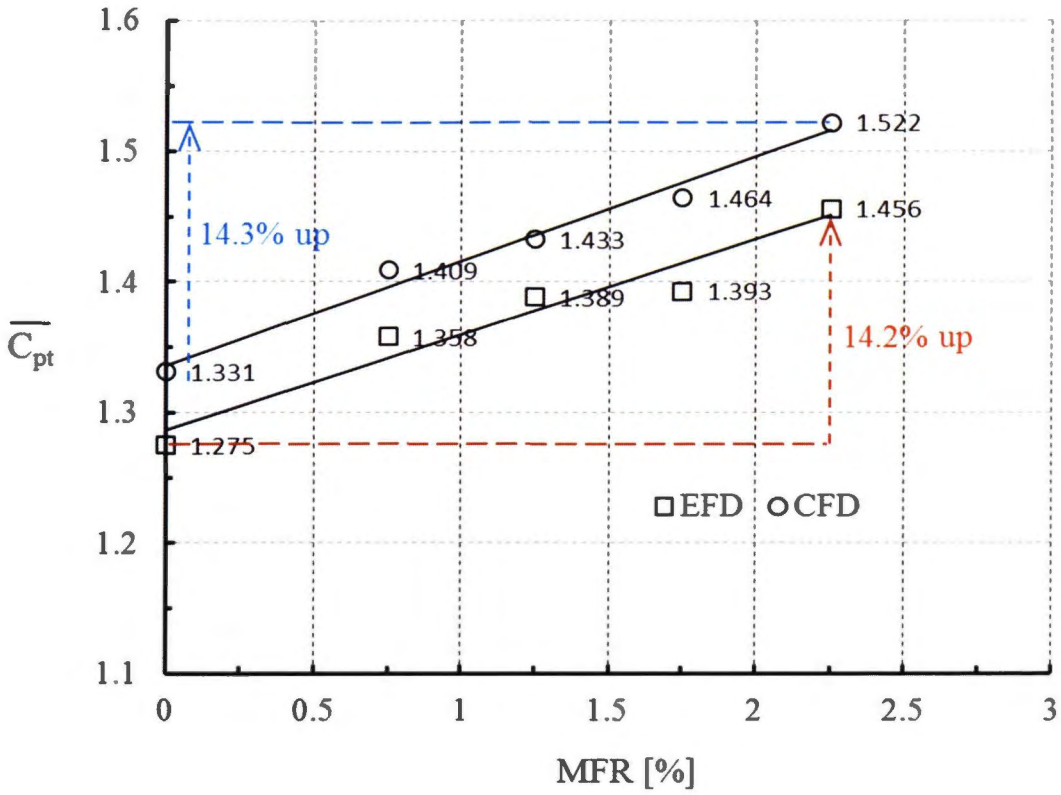

Figure 53 Loss trend in comparison between CFD and EFD

3.3.4 Predicted secondary flow structures

According to the discussion in the previous sections, even though the discrepancy in terms of position and shape of contours in comparison between CFD and EFD, they almost presented the similarity on the contour trend. For instant, the presence of the additional loss region which was due to the increased strength of the passage vortex has been captured in both studies. Thus, the advantage of the numerical simulation can be taken to predict the structures of the secondary flows before and after the leakage flow injection. Present section intended to provide details flow structures on the endwall region predicted by the CFD. The details will provide further understanding on the interaction between the leakage and the mainflow. Figure 54~Figure 56 show the vortex core generated at the swirling strength equal to 760 [s-1] for baseline case, MFR=1.25% and MFR=2.25%, respectively. The color of the vortex core is representing the vorticity, ζ valued within the range of 2000 [s-1] and –2000 [s-1]. In order to observe the formation of the vortical structures near the blade LE, a streamline is presented on stagnation plane on each figure where the line color represents the flow

velocity. Furthermore, the ζ contour at Plane B which is located at approximately 60% from blade PS is also presented in each figure. These two planes enable the observation of the horse-shoe vortex (HSV) development in the cascade. Note that $x/C_{ax} = 0$ is parallel to the position of the blade LE.

In the baseline case as shown in Figure 54, CFD has predicted the formation of pressure side leg horse-shoe vortex (PS-HSV) and suction side leg horse-shoe vortex (SS-HSV) near the blade leading edge. PS-HSV travels from the blade PS to neighboring blade SS consequently meet the SS-HSV coming from adjacent blade LE. The presence of the leading edge corner vortex has also been predicted at both sides of blade leading edge with a smaller core compared to HSV. Based on the streamline, the HSV is centralized at $x/C_{ax} = -0.15$, $z/s=0.02$ and the higher ζ core captured on Plane B located at approximately $x/C_{ax} = 0.35$ illustrates the PS-HSV moving towards downstream of the blade passage. A modification of the existing secondary flow structures occurred when the leakage flow is injected, see Figure 55. The introduction of the leakage injection upstream of the blade LE unfortunately induced to the flow blockage just downstream of the slot (slot location, $x/C_{ax} = -0.63$). As a result, the strength of the HSV near the blade LE was amplified as indicates by the increases diameter of the swirling flow in Figure 55. Figure also clearly explained the increase of HSV strength with the higher swirling energy of the core compared to the baseline case. This resulting in increase of PS-HSV energy which will allow it to travel across from blade PS and lifted- off onto adjacent blade SS. At MFR=2.25%, ζ contour on Plane B in Figure 56 shows that the direction of the PS-HSV slightly shifted towards upstream. The PS-HSV seems to be merged with the adjacent flow ζ caused by the separation flow downstream of the slot. At MFR=1.25%, a newly generated vortex core can clearly be observed along the pitchwise direction just downstream of the slot. As shown in Figure 57, due to the high pressure near the blade stagnation region, ejected leakage flow tends to move towards centre of the blade passage and accumulated with the opposite flow direction of the leakage flow that coming from adjacent blade. This phenomenon has influenced to the formation of new vortex core (accumulated flow vortex, AFV) which then developed along the blade SS surface. As been shown in previous section, the presence of this vortex core is predicted to responsible to the additional loss which was generated after the leakage flow injection. As the MFR increases, the AFV strength is further increases. At MFR=2.25%, see Figure 56, ejected leakage flow has much higher momentum to penetrates into the main

stream; particularly near the stagnation region compared to the lower MFR cases. Higher blockage consequently influenced to higher strength of the HSV. Noted that the higher energy of the PS HSV, the earlier the reattachment onto the adjacent blade SS occurs. The position of the PS-HSV shifted again toward upstream compared to the lower injection and baseline cases as shown in Plane B in each figure. This phenomenon consequently deflected the direction of the LE CV upwards. The explanation parallel to the position of first loss core which is shifted towards midspan at a higher MFR as shown in C_{pt} contours in EFD and CFD.

To obtain the full understanding on the vortex propagations, the vortex core generated near the blade trailing edge are also presented in Figure 58~Figure 60. Again, the ζ contour at Plane 1.25Cax is also shown in order to directly recognize the sources of the ζ from the vortex core. Further downstream of the blade leading edge, it can be observed that PS-HSV was deflected by the SS-HSV before attaching onto the adjacent blade SS surface, see Figure 58. This SS-HSV is actually coming from adjacent blade suction, losing its swirling energy when travels away from the blade leading edge. In contrast, the strength of the LE-CV increases near the blade throat and developed in the same direction with the PS-HSV to become a large passage vortex at blade downstream plane.

The first C_{pt} core which was presented in Figure 43 (a) and Fig. 50(a) are considered to be associated with this particular vortex core. Figure 58 also shows the origin of the counter vortex (CV) located just downstream of the blade throat. The CV rotating in anti-clockwise direction was also captured by the ζ contour shown in Figure 50 (b) ~ Figure 52 (b). Figure 59 and Figure 60 also clearly indicate the development of the AFV near the blade TE. Thus, the newly generated vortex core, AFV at upstream seems to be responsible to the additional losses. Since the ζ contours based on CFD is showing almost similar trend with the EFD, the predicted vortex core could explain the sources of the flow vorticity as shown in bottom side of Figure 58~Figure 60. Figure 61 shows the birdview of the flow streamline in comparison between baseline and injection cases.

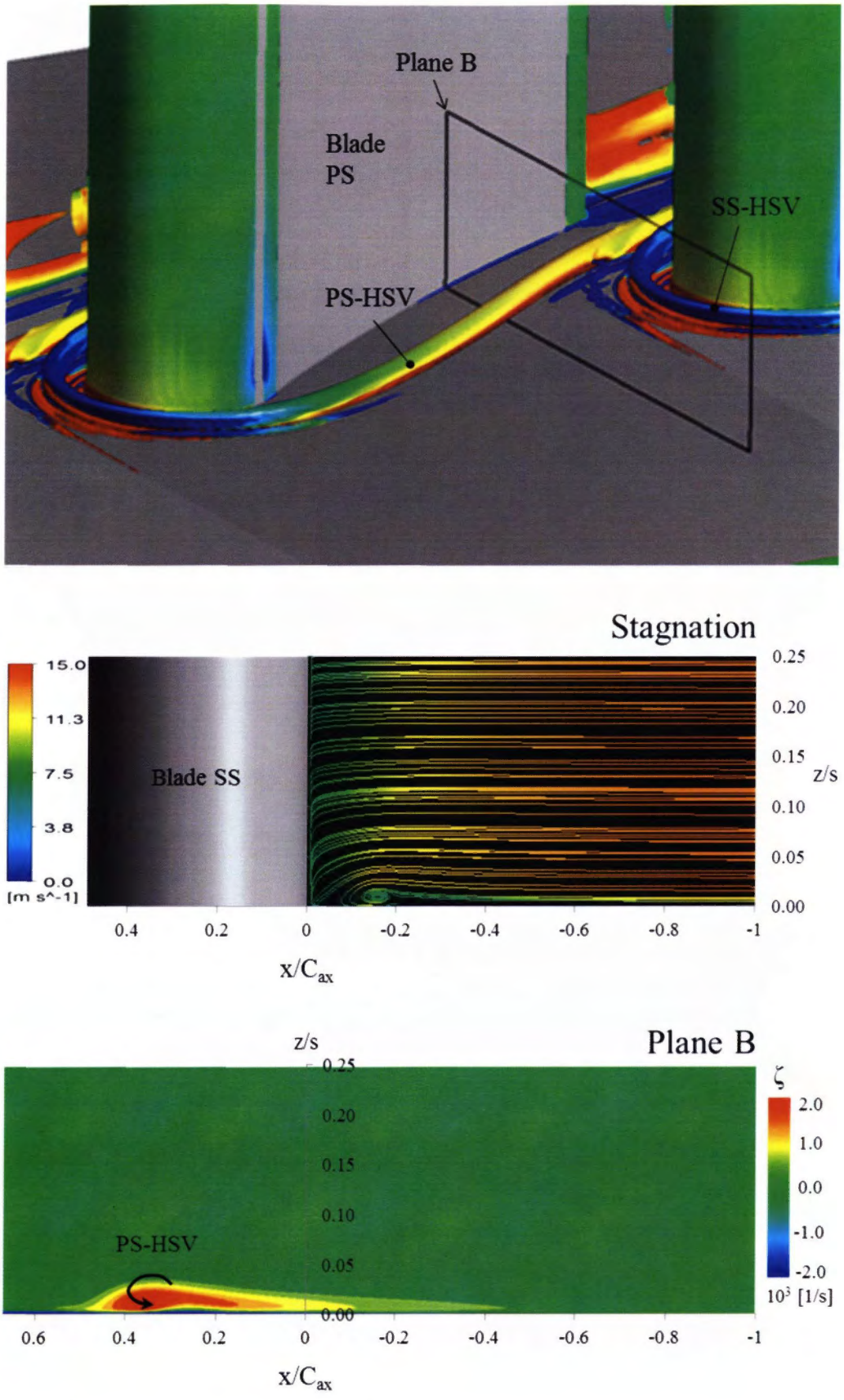

Figure 54 Predicted secondary flow structures at upstream for baseline case

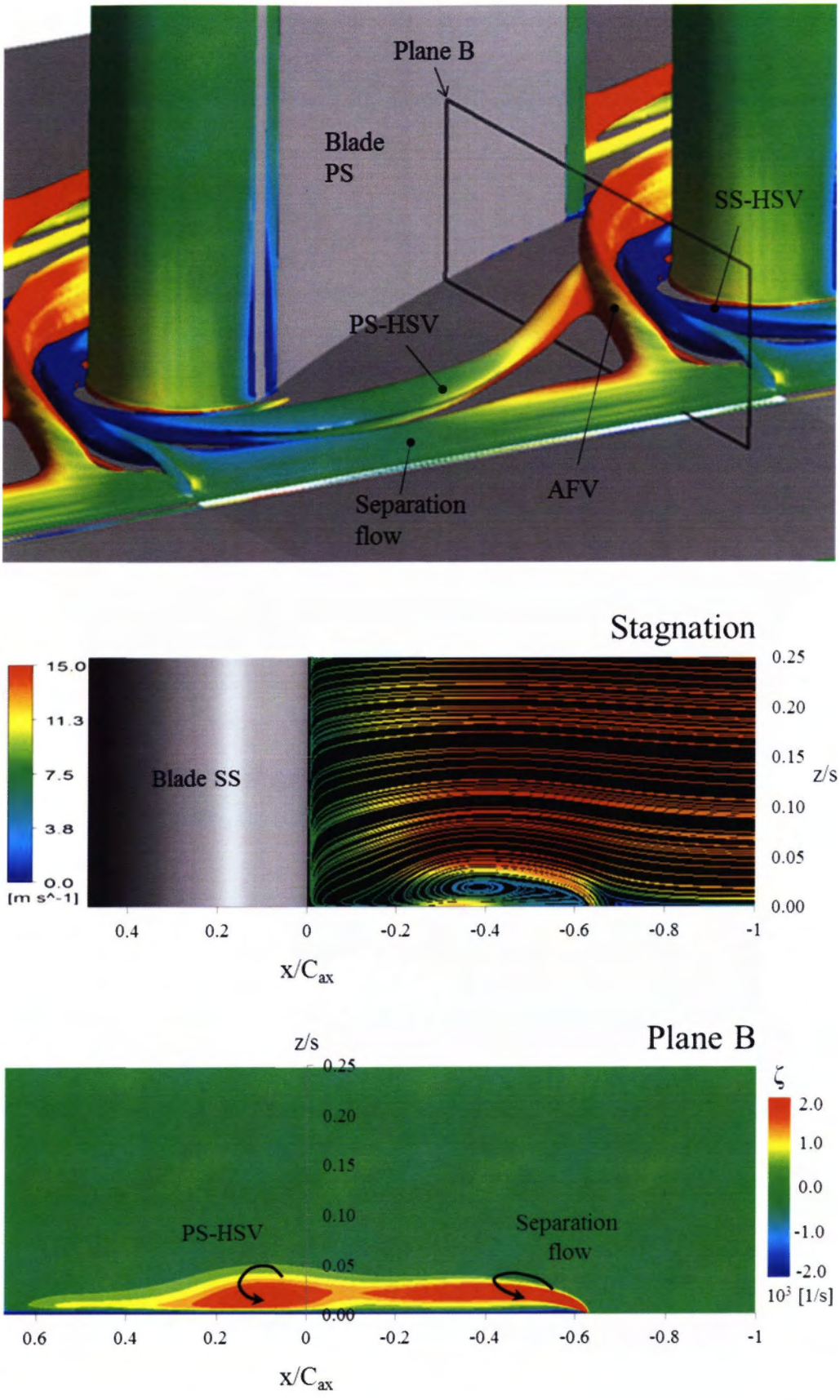

Figure 55 Predicted secondary flow structures at upstream for MFR=1.25%

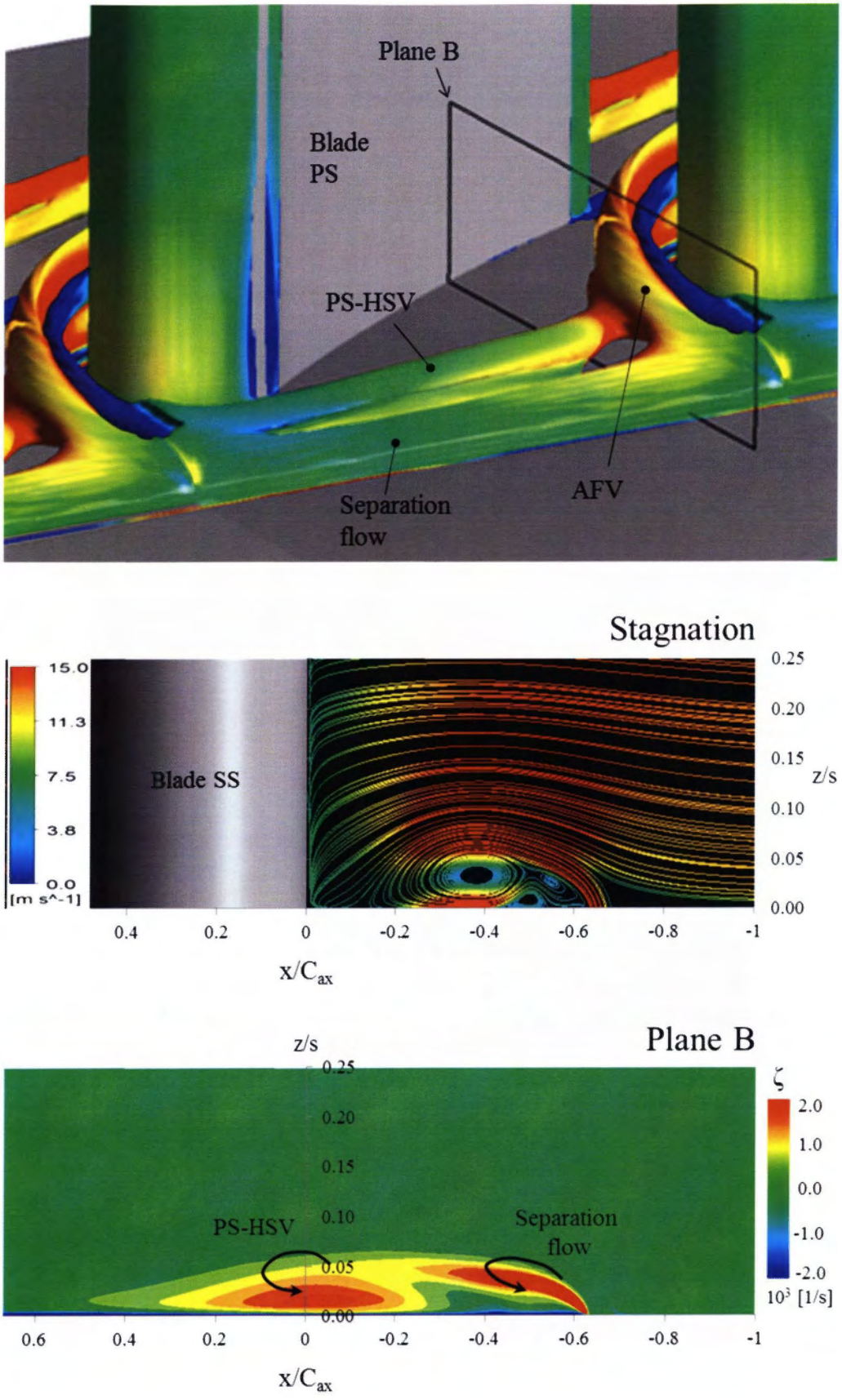

Figure 56 Predicted secondary flow structures at upstream for MFR=2.25%

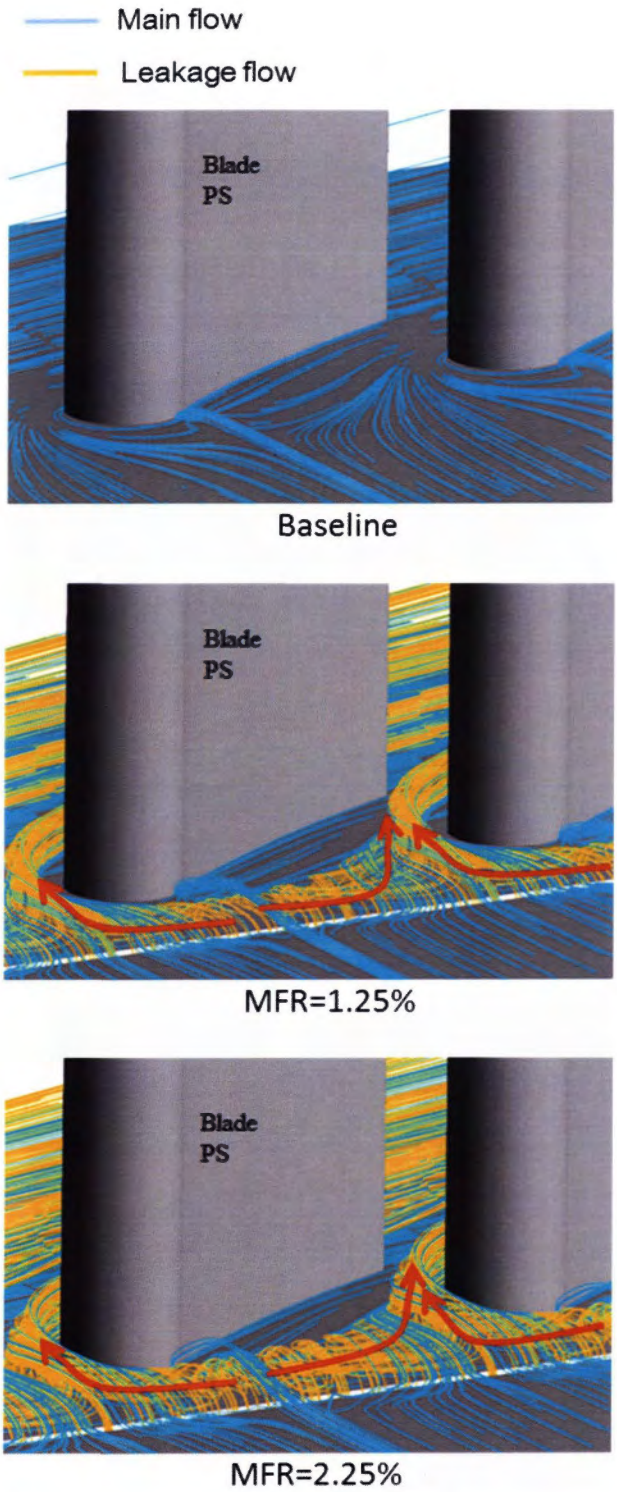

Figure 57 3D streamline on the endwall region for baseline (top), MFR=1.25% (middle) and MFR=2.25% (bottom)

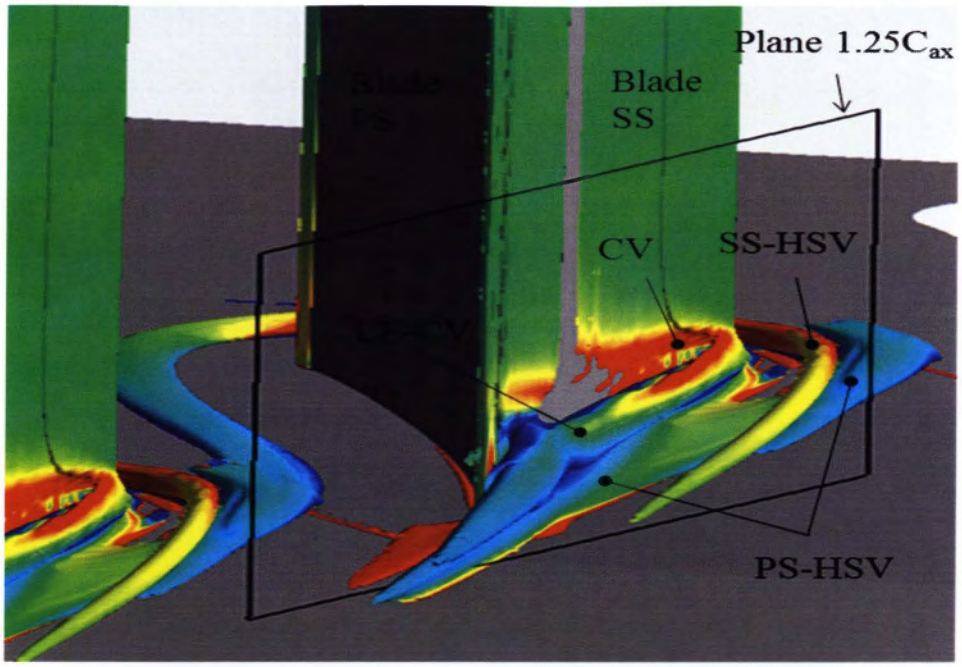

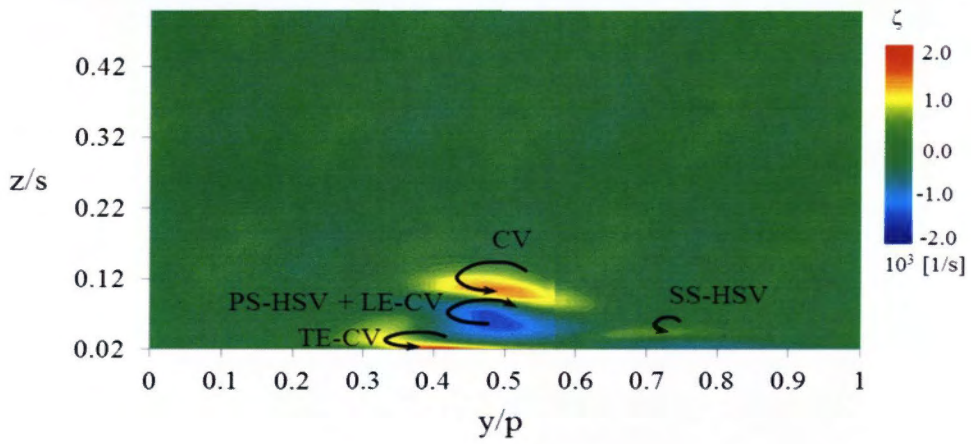

Plane 1.25C$_{ax}$ vorticity-CFD

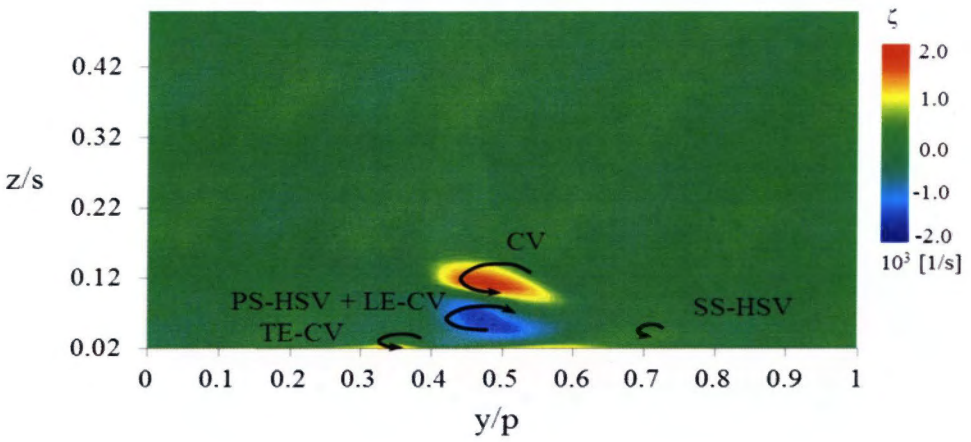

Plane 1.25C$_{ax}$ vorticity-EFD

Figure 58 Predicted flow structures at downstream for baseline case

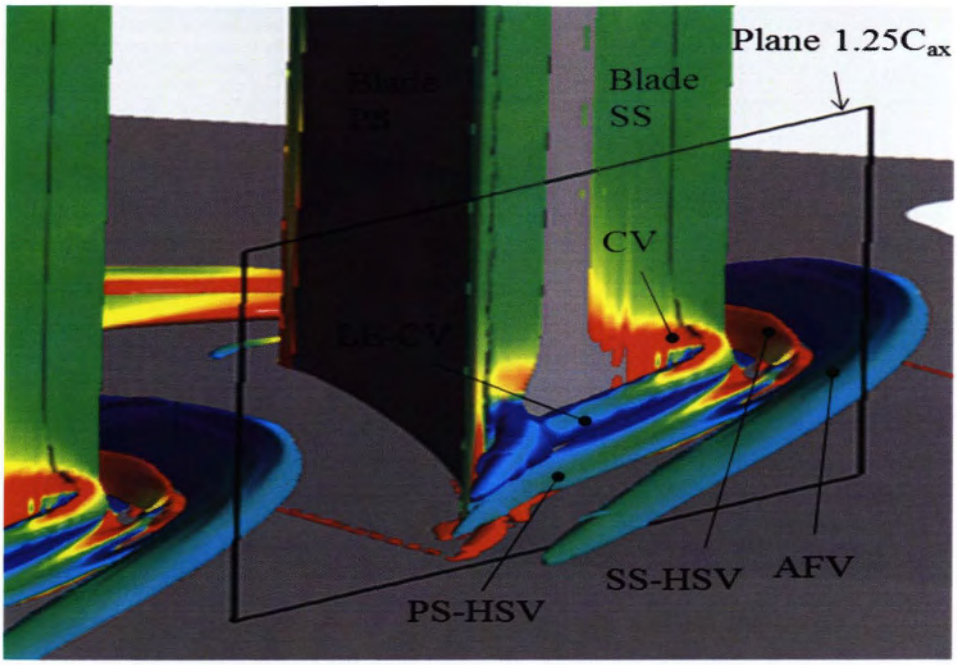

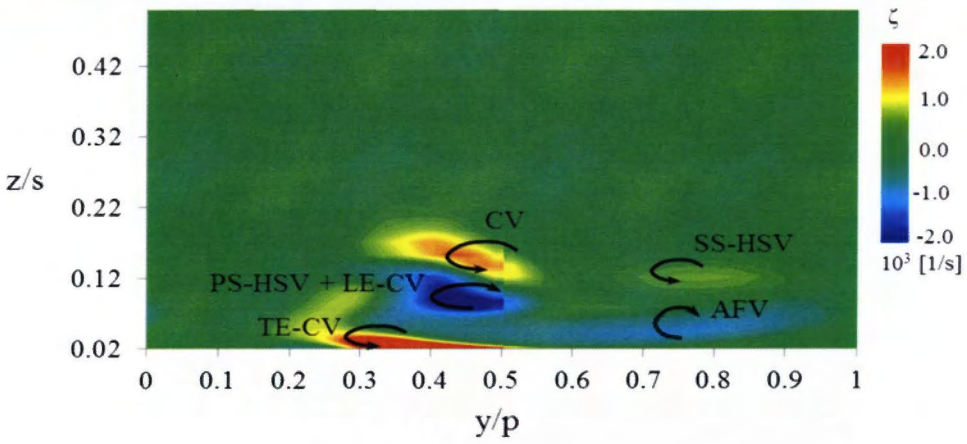

Plane 1.25C$_{ax}$ vorticity-CFD

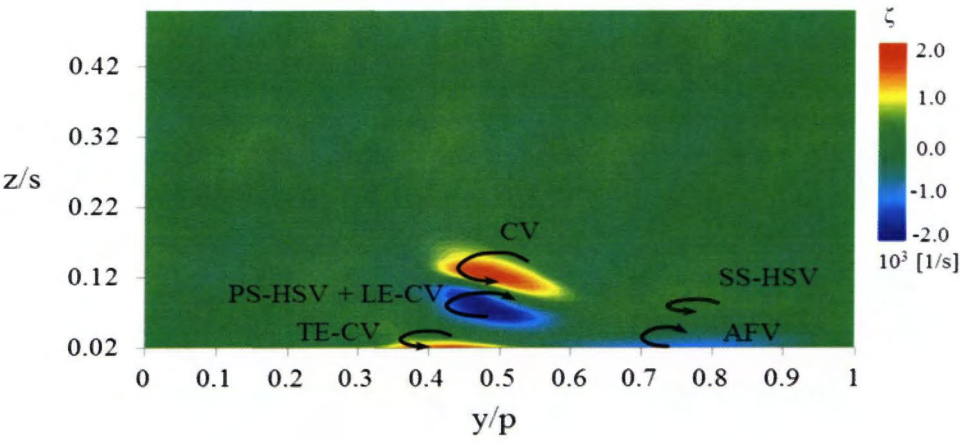

Plane 1.25C$_{ax}$ vorticity-EFD

Figure 59 Predicted flow structures at downstream for MFR=1.25%

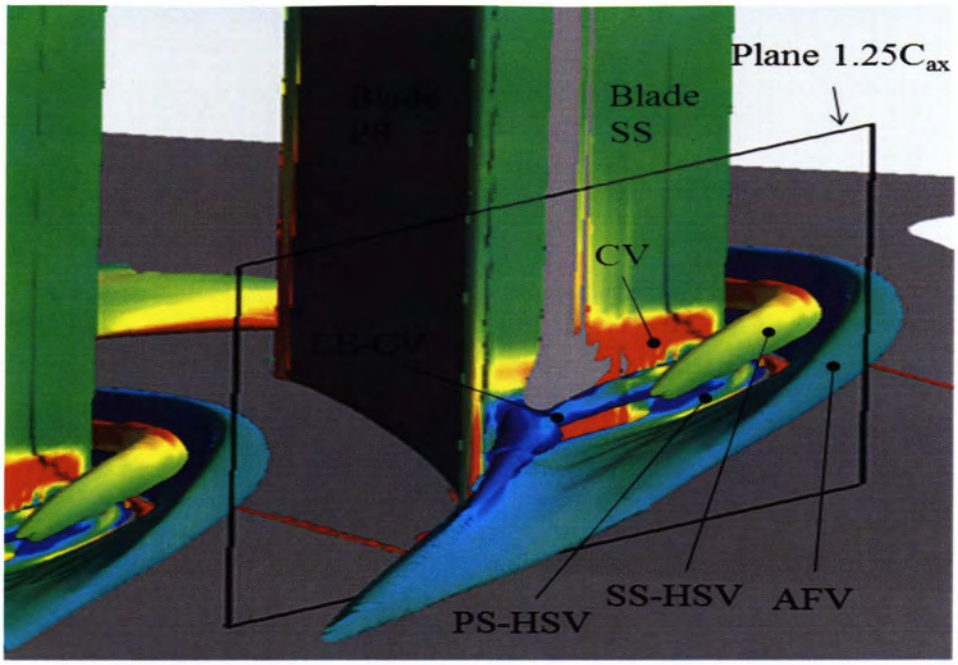

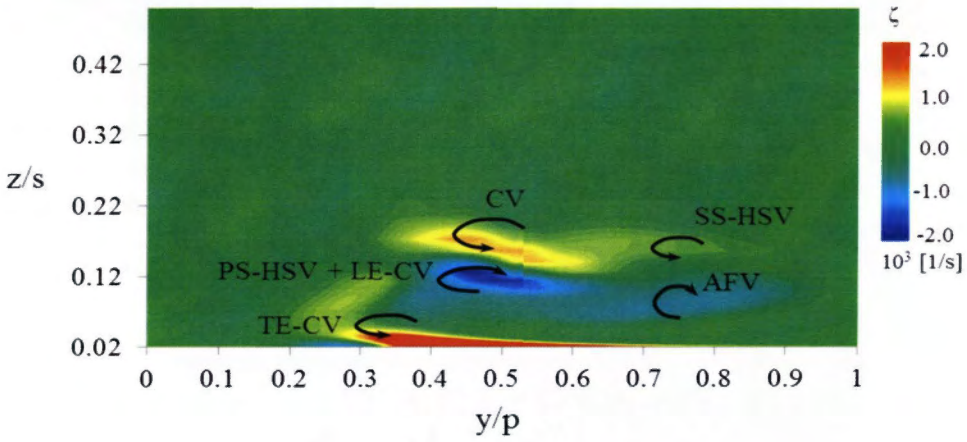

Plane 1.25C$_{ax}$ vorticity-CFD

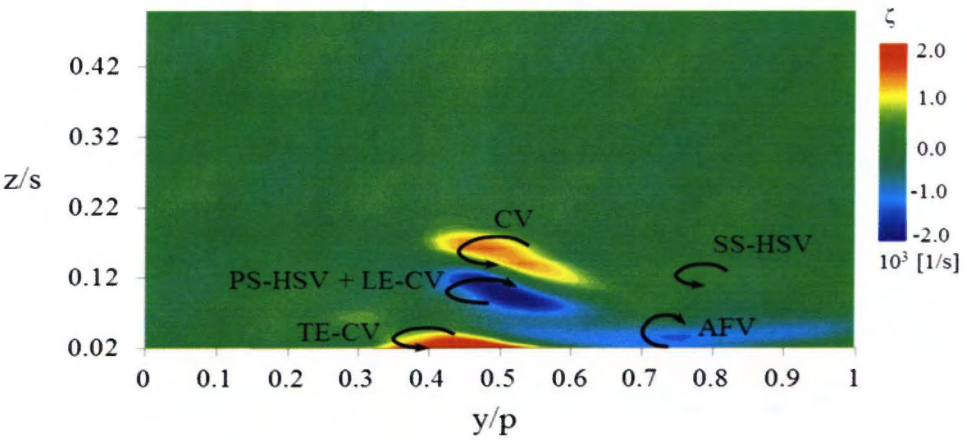

Plane 1.25C$_{ax}$ vorticity-EFD

Figure 60 Predicted flow structures at downstream for MFR=2.25%

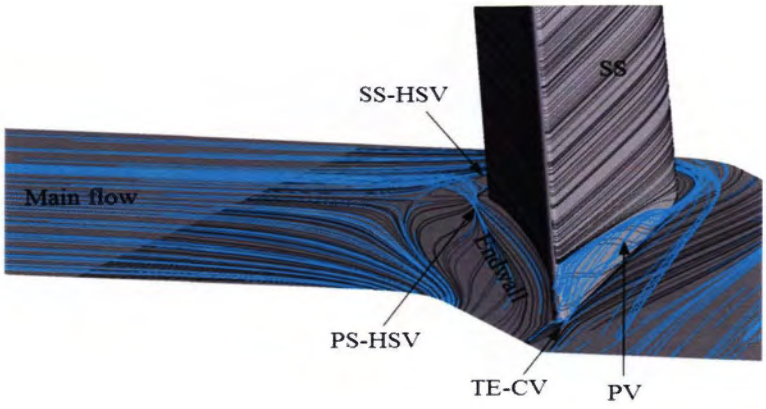

(a)Baseline case

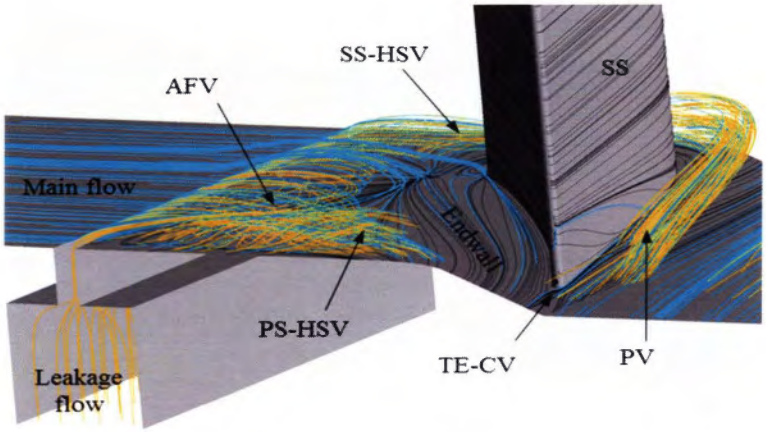

(b) MFR = 1.25%

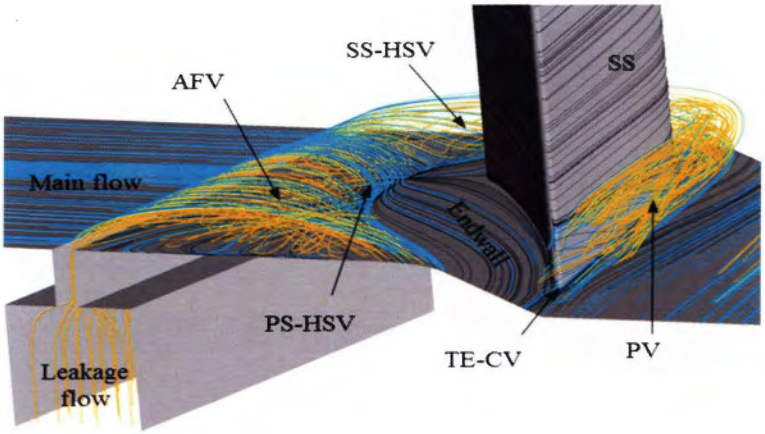

(c)MFR = 2.25%

Figure 61 Birdview of flow streamline for baseline, 1.25% and 2.25% injections

3.4 Effect of the secondary air behaviour on C_{pt} contours

3.4.1 CFD modelling

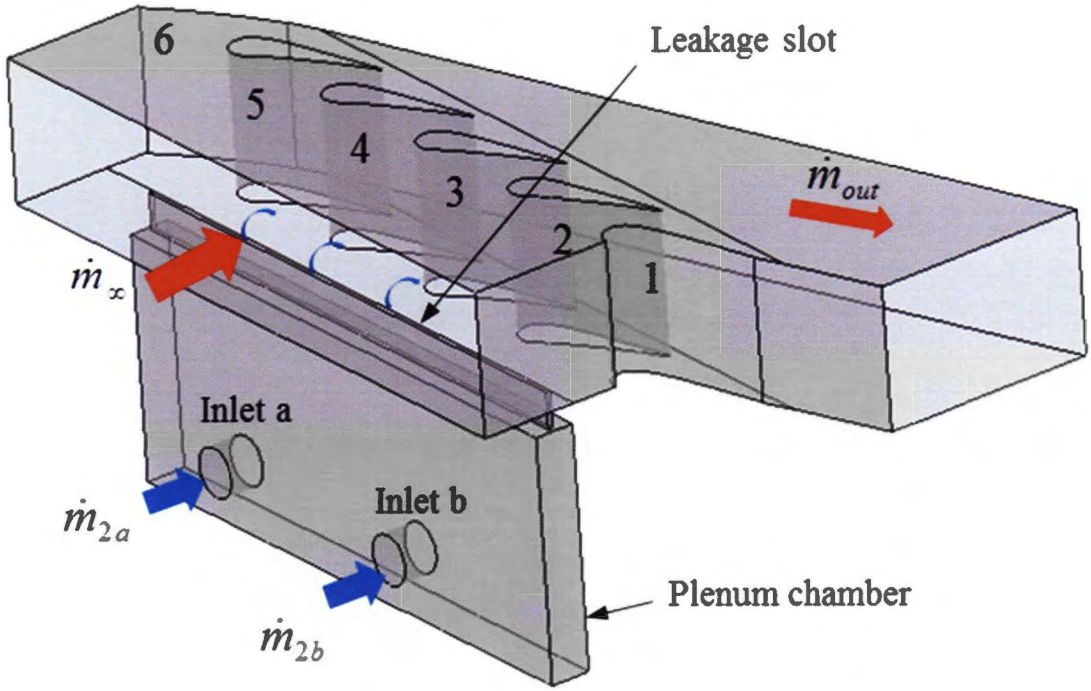

Figure 62 CFD modelling to predict the effect of secondary air profile on C_{pt}

The discrepancy in terms of shape and position of the loss contours between CFD and EFD shown in previous section especially for the leakage injection cases were considered due to the different secondary inlet profile. In CFD, the translational periodicity was applied on the interface between the pitch thus the uniform flow distribution were predicted along the slot exit. However, the secondary flow behaviour cannot be revealed in real situation due to the difficulty of measurement device to access in a very limited area inside the plenum chamber. Furthermore, it is very difficult to obtain a uniform flow distribution inside the plenum chamber. Thus, the mass flow rate, $\dot{m}_2$ has been applied on the secondary inlet boundary condition based on the experimental condition which was measured by laminar flow meter. From Figure 18, a secondary air coming from the laminar flow meter was split into two inlet pipes before entering the plenum chamber. In order to predict the flow with almost the same condition to the real situation, a new CFD model including the plenum chamber with two inlets (**a** and **b**) was also generated as shown in Figure 62. Plenum

chamber extended for 4 pitches parallel to the slot length. Gridgen was applied to generate the mesh with 12.4 million elements with fully structured multi blocks. By considering the time and cost required, approximately 1.5 million of mesh element were generated for each blade pitch. The same grid topology was applied on each blade pitch thus the bias causes by the grid itself can be avoided. This model enables the studies on the secondary air behaviour on the C_{pt} contours. The same turbulence model used in previous flow prediction, SST was adopted. From Figure 62, the total mass flow rate at cascade downstream can be represented as

$$\dot{m}_{out} = \dot{m}_{\infty} + \dot{m}_2 \tag{35}$$

Since the secondary air inlet was split into two pipes (inlet **a** and inlet **b**), here $\dot{m}_2$ can be represented as

$$\dot{m}_2 = \dot{m}_{2a} + \dot{m}_{2b} \tag{36}$$

Thus,

$$\dot{m}_{out} = \dot{m}_{\infty} + \dot{m}_{2a} + \dot{m}_{2b} \tag{37}$$

In order to investigate the effect of the flow inside the plenum chamber, fixed $\dot{m}_2$ at MFR=2.25% was predicted with several cases by different $\dot{m}_{2a}$ and $\dot{m}_{2b}$. Five cases were predicted in this study.

Case 1

$$\boxed{\dot{m}_{2a} = \dot{m}_{2b} = \frac{1}{2}\dot{m}_2}$$

Case 2

$$\boxed{\dot{m}_{2a} = \frac{2}{3}\dot{m}_2} \qquad \boxed{\dot{m}_{2b} = \frac{1}{3}\dot{m}_2}$$

Case 3

$$\dot{m}_{2a} = \frac{3}{4}\dot{m}_2 \qquad \dot{m}_{2b} = \frac{1}{4}\dot{m}_2$$

Case 4

$$\dot{m}_{2a} = \frac{1}{3}\dot{m}_\infty \qquad \dot{m}_{2b} = \frac{2}{3}\dot{m}_\infty$$

Case 5

$$\dot{m}_{2a} = \frac{1}{4}\dot{m}_\infty \qquad \dot{m}_{2b} = \frac{3}{4}\dot{m}_\infty$$

The same mass flow rate was applied to $\dot{m}_{2a}$ and $\dot{m}_{2b}$ in Case 1, $\dot{m}_{2a} > \dot{m}_{2b}$ in Case 2 and Case 3 while $\dot{m}_{2a} < \dot{m}_{2b}$ in Case 4 and Case 5. These all cases were applied into two secondary inlets and the different flow behaviour inside plenum chamber were expected. Since the measurement grid of the total pressure was located at downstream of the Blade 3, see Figure 22, thus the same position of the C_{pt} contour will be observed to see the changes of the flow behaviour by each cases.

3.4.2 Results and discussion

Predicted flow streamline inside the plenum chamber by different mass flow rate from inlet **a** ($\dot{m}_{2a}$) and inlet **b** ($\dot{m}_{2b}$) at fixed $\dot{m}_2$ is presented in Figure 63. There are three different colours of streamline; blue represents the main flow, yellow represents a leakage flow coming from inlet **a** while red represents a leakage flow coming from inlet **b**. All cases illustrate that the leakage flow from both inlets were deflected by the plenum chamber wall which just located close to the air inlet. Thus they tend to move towards side and bottom wall and finally penetrated into the mainstream. This phenomenon influenced to the high turbulence flow inside the chamber. It clearly shows that the flow inside the plenum chamber is ununiformed before entering the mainstream through the slot. Furthermore, the flow structures inside the chamber is significantly depends on the amount of flow from inlet **a** and

inlet **b**. Case 1 in Figure 63 (a) presents that the penetration of the flow toward each other from both inlet almost the same since the same mass flow was applied. For the Case 2 and Case 3 where $\dot{m}_{2a} > \dot{m}_{2b}$, see Figure 63 (b) and (c), the flow inside the chamber is highly influenced by the yellow streamline ($\dot{m}_{2a}$) and consequently changed the flow structure. On the other hand, Case 3 and Case 4 for $\dot{m}_{2a} < \dot{m}_{2b}$, see Figure 63 (d) and (e), the flow is highly influenced by red streamline ($\dot{m}_{2b}$) instead of yellow. Figure 64 (a)~(d) presents the endwall streamline which illustrates the direction of the leakage flow coming from the plenum chamber based on Case 1~Case 5, respectively. The concentration of flow observation will be made on the flow structures between Blade 3 and Blade 4 where its parallel to the position of the traverse grid at blade downstream. As being discussed in previous section, the leakage flow coming from the slot tends to move towards center of the blade passage due to the high pressure close the blade stagnation region. Then it accumulated with the opposite flow direction coming from adjacent blade stagnation region to generate a newly vortex core, AFV (as shown in Figure 56). The shape and position of the C_{pt} contours presented in previous section for the leakage injection cases are considered to highly influenced by the formation of AFV.

As shown by Case 1 in Figure 64 (a), AFV is actually generated by the accumulation of flow coming from inlet **a** and inlet **b** (illustrates by the arrow **a** and **b**). However, red streamline coming from inlet b mostly influences the AFV. In Case 2 when $\dot{m}_{2a}$ was increased, see Figure 64 (b), red streamline seems to be reduced and its almost the same with the yellow streamline coming from inlet a to generate AFV. However, when the $\dot{m}_{2a}$ continuously increases as Case 3 in Figure 64 (c), AFV mostly influenced by the yellow streamline. In contrast, AFV was mostly generated by the red streamline when $\dot{m}_{2b}$ being increases and yellow streamline was eliminated at this region, see Figure 64 (d) and (e). The changes of flow phenomenon presented by Case 1~Case 5 is considered at least to change the characteristic of the AFV consequently effected to the shape and position of the C_{pt} contours at blade downstream. C_{pt} contours downstream of Blade 3 for Case 1~Case 5 are presented in Figure 65 (a)~(e). The range of contours are the same with the C_{pt} contours shown in Figure 47 (a) and Figure 52 (a) thus direct comparison can be made towards EFD and the periodicity applied CFD modelling. Periodicity applied CFD model was presented in Figure 35 and Figure 36 in Chapter 2. The first loss core in Figure 65 slightly changed among the cases. Even though this core was actually associated by the PS-HSV and also LE-CV, the change of

the AFV characteristics is predicted to give some effect on the development of PS-HSV since it was deflected by the AFV near the blade SS (as shown in Figure 56). As a result, slightly different shape of first core was presented by each cases. Furthermore, the different flow structure inside the chamber gives a significant change on the third loss core. The different leakage fluid momentum from both sides (**a** and **b**) is considered might be changed the direction and strength of the AFV which thus resulting different C_{pt} contour at downstream. In comparison with the EFD in Figure 47 (a), Case 3 illustrates almost the similar shape of third core among the cases. Additionally, the shape is also significantly different in comparison with periodicity model (earlier model) in Figure 52 (a). However, it is difficult to investigate the actual condition by the measurement in order to have a similar condition in CFD simulation due to the accessibility of the measurement device in such region.

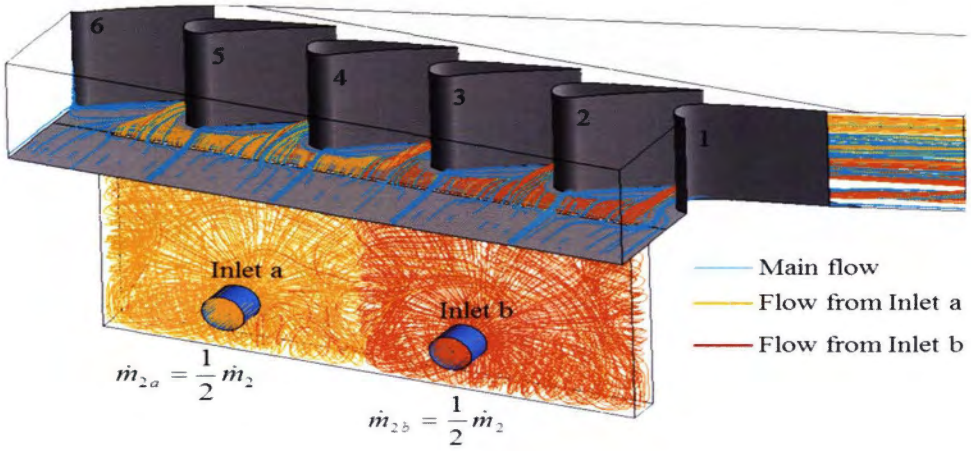

(a) Case 1

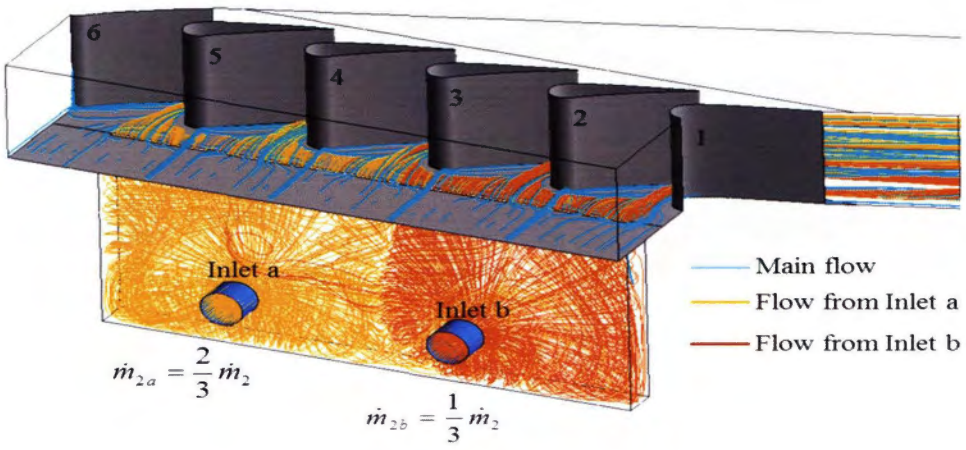

(b) Case 2

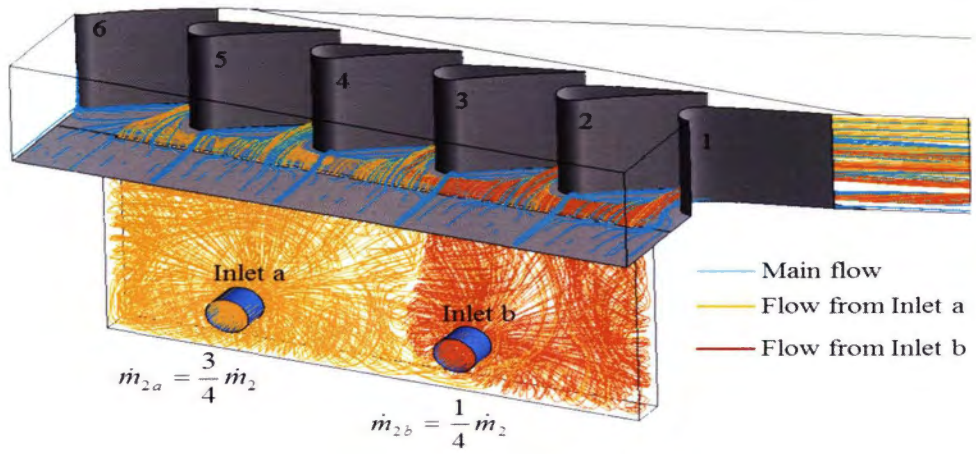

(c) Case 3

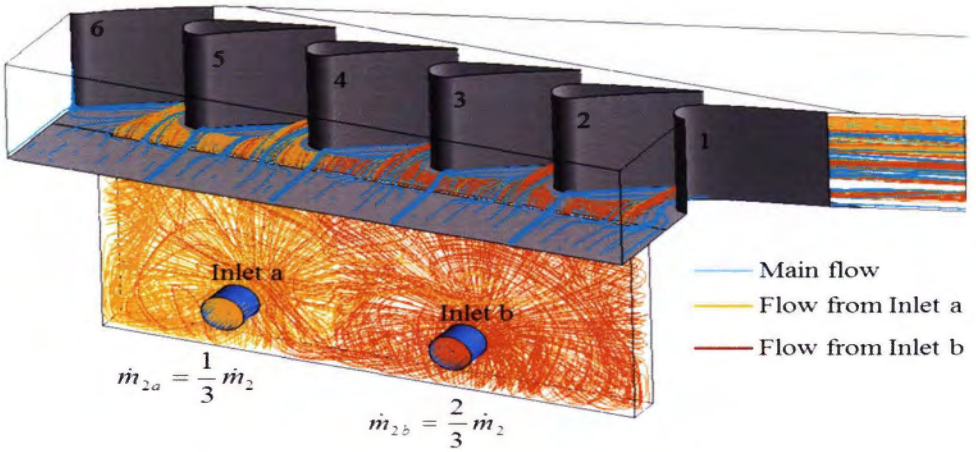

(d) Case 4

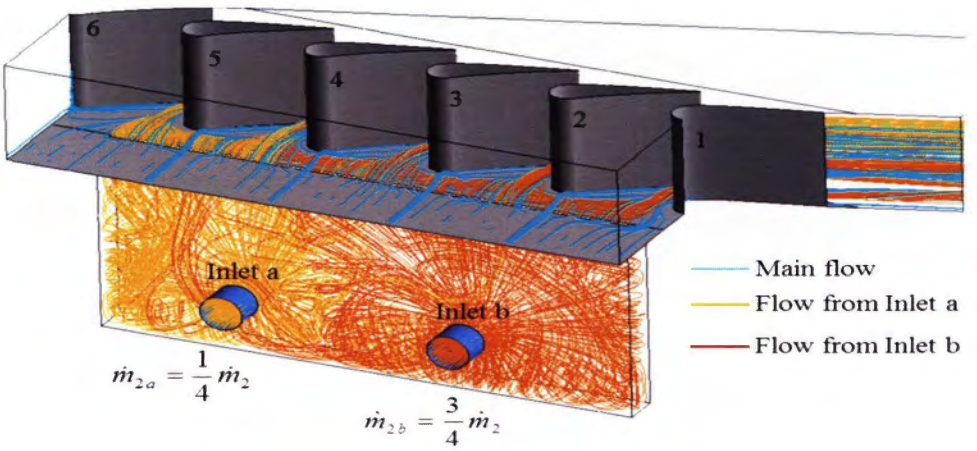

(e) Case 5

Figure 63 Plenum chamber flow streamline for each case

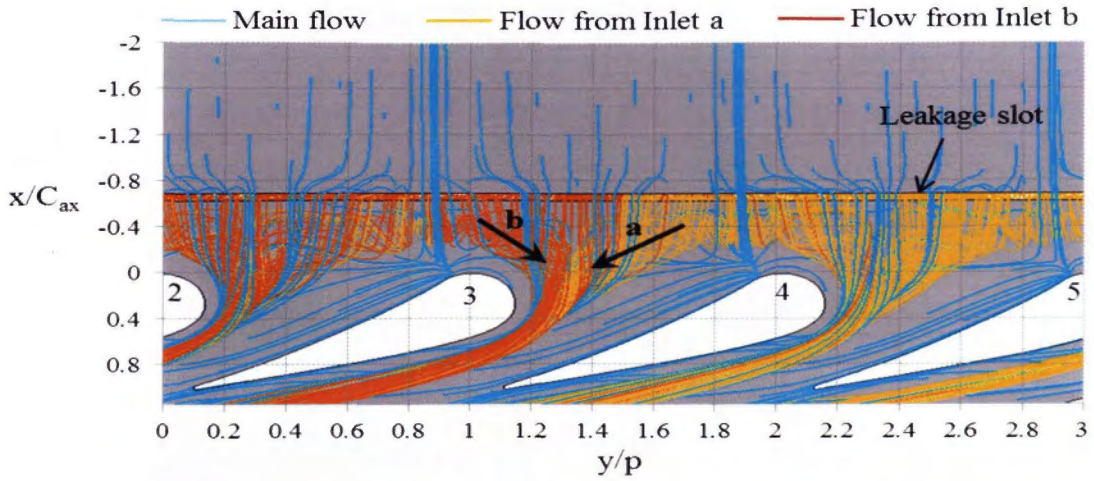

(a) Case 1

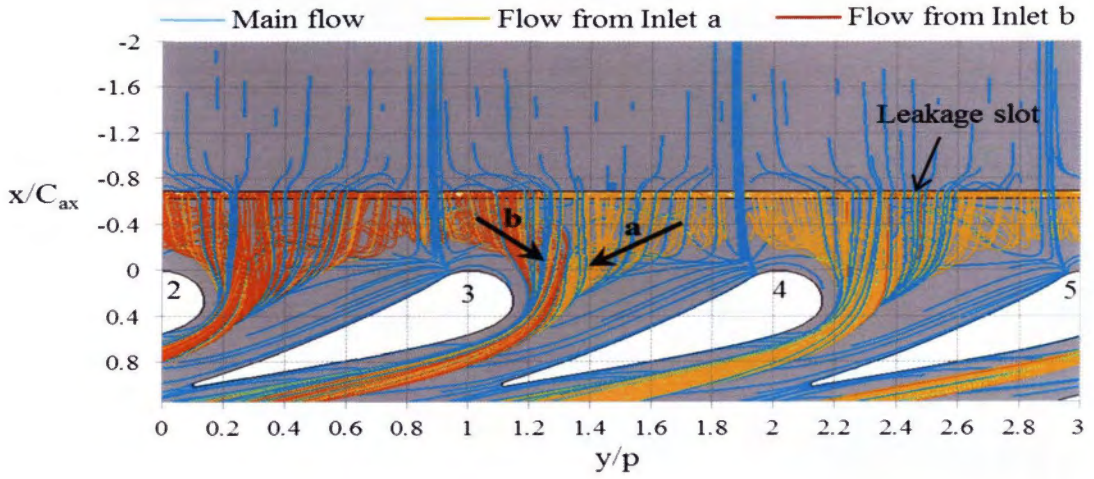

(b) Case 2

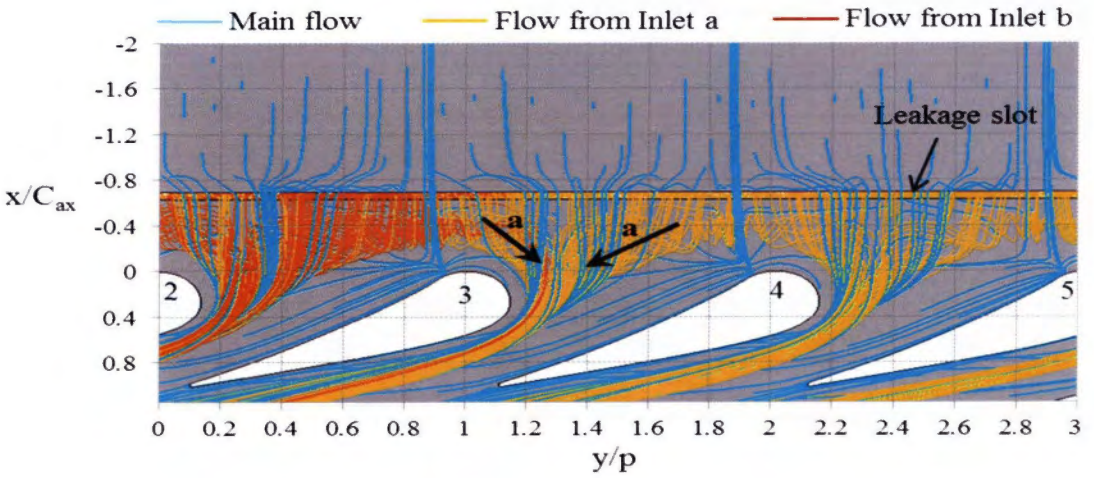

(c) Case 3

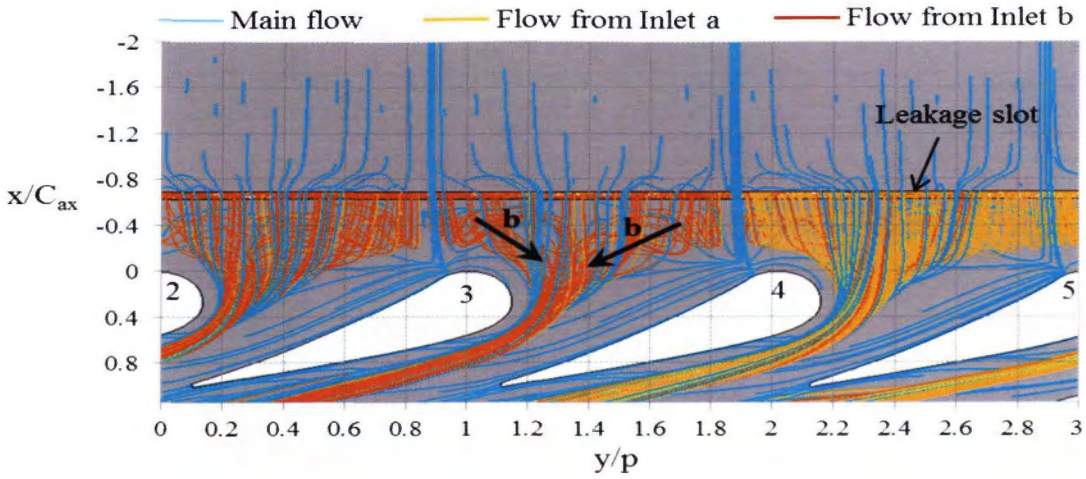

(d) Case 4

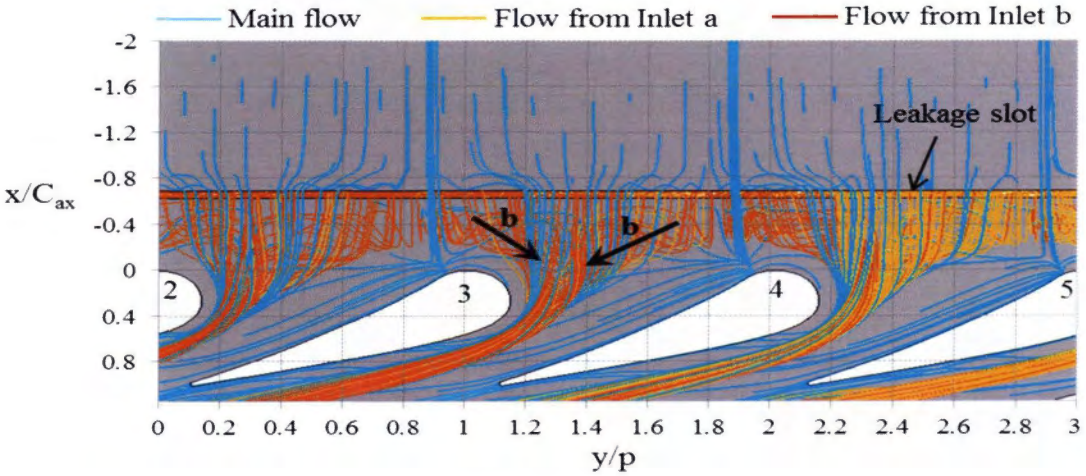

(e) Case 5

Figure 64 Endwall streamline for each case

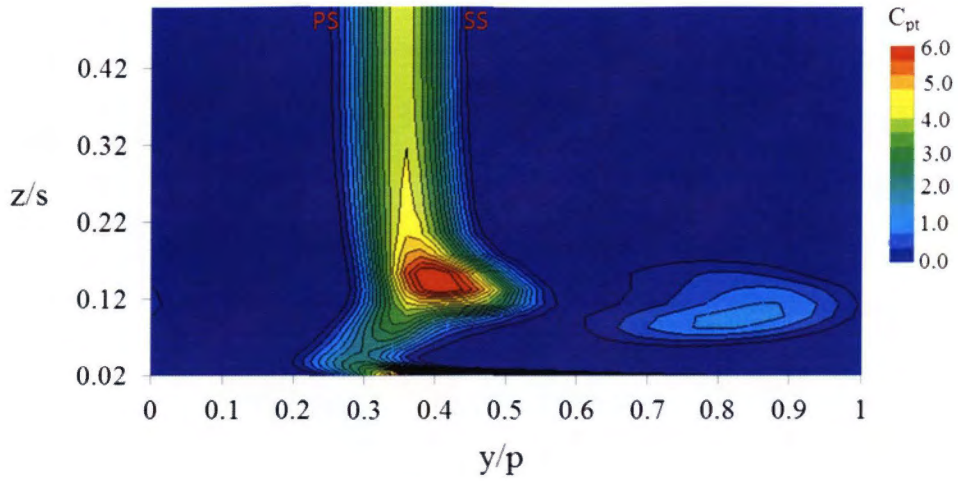

(a) Case 1

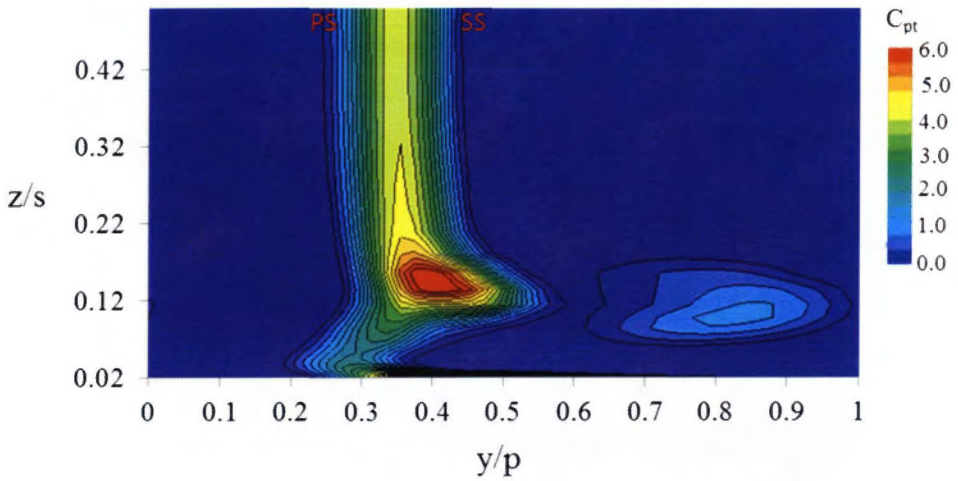

(b) Case 2

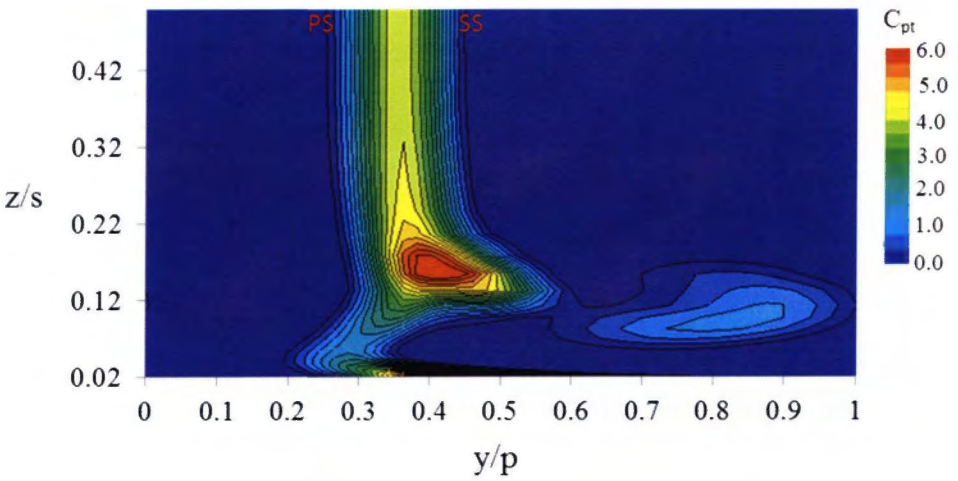

(c) Case 3

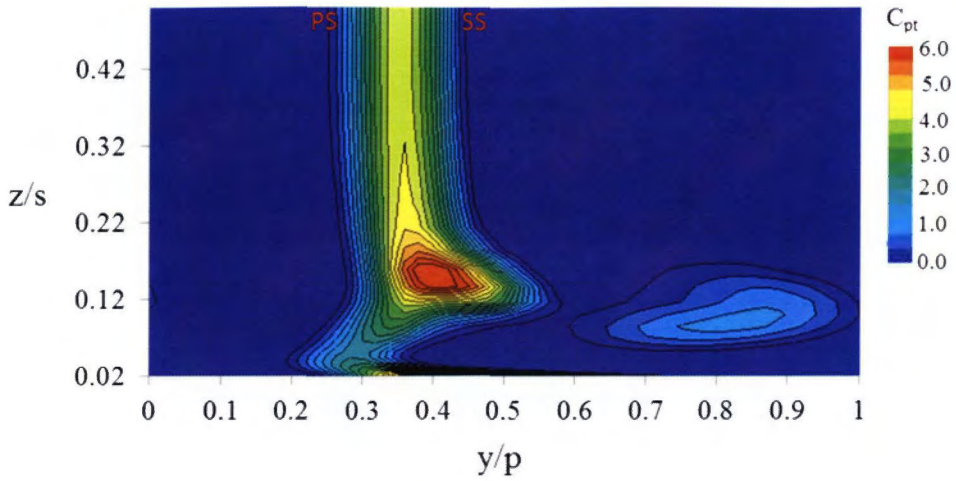

(d) Case 4

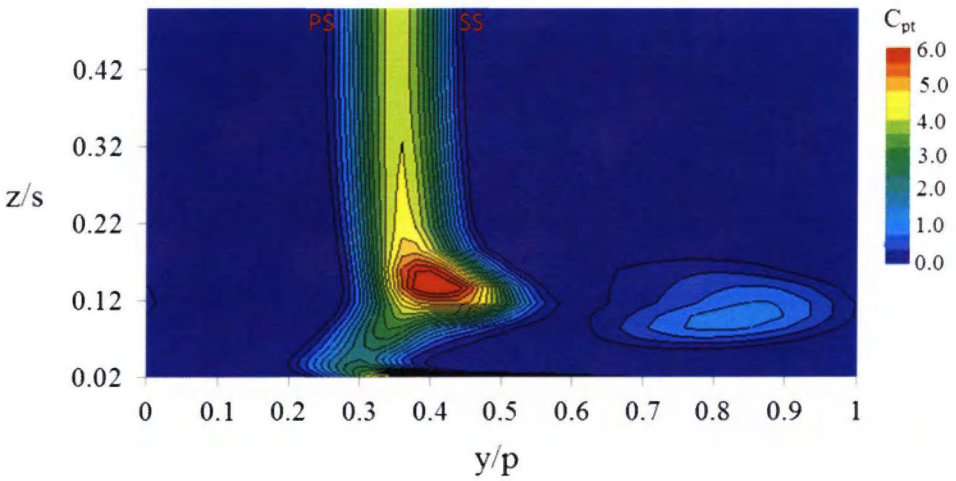

(e) Case 5

Figure 65 C_{pt} contour at Plane $1.25C_{ax}$ for each case

3.5 Thermal performances

3.5.1 Experimental based performances

The potential of the leakage flow injection to protect the endwall surfaces has been revealed by conducting liquid crystal for surface temperature measurement. Based on the temperature data, non-dimensional temperature which is represented by film cooling effectiveness, η is used to describe the cooling performance of leakage flow. The blue contour illustrates the lower η while the red one illustrates the higher η. Figure 66 (a) ~Figure 69 (a) indicate the η contours for MFR=0.75%, 1.25%, 1.75% and 2.25%, respectively. In order to have details information about the thermal performance, the heat transfer coefficient, *h* and the RGB propagation illustrated by the liquid crystal are also included in each figure. Figures illustrate the contour from the position of the leakage slot (x/C_{ax}= -0.63) till downstream of the blade TE for two pitches (y/p = 0~2). View of the two blades also included and that is the actual camera angle during measurement. Noted that the axis showing by the gridlines is only referring to the endwall surfaces and invalid for the blade tip region. This is because the camera was slightly inclined in order to capture the most important region in the measurement. At lower injection of 0.75%, see Figure 66 (a), the unprotected region in pitchwise direction is observed from y/p=0.2~0.8 and y/p=1.4~1.9. This is because the leakage flow was unable to be injected near the stagnation region due to the higher pressure. This influenced them to be injected into the mainstream at the lowest pressure region located between the two blades at approximately y/p=0.8~1.3. Since the leakage flow only be penetrated near this region, high level of η contours was obtained. However, when the leakage flow increased to 1.25%, see Figure 67, the protection region became wider not only in pitchwise direction but also in axial direction. Unlikely the case for 0.75%, the leakage flow provides a protection layer along the cascade pitch even though at a lower level η. Upstream of the blade LE, leakage flow provided the protection layer from x/C_{ax}=-0.63 to x/C_{ax}=-0.43 which approximately 35% of the endwall surfaces towards blade LE. This might be considered that the leakage flow had enough momentum to be penetrated into the higher pressure mainstream especially close to the stagnation region. At y/p=0.8~1.2, the contour also seems to expand from x/C_{ax}=-0.03 to x/C_{ax}=0.57 and the contour shape at this region are highly influenced by the secondary flow behavior. They likely influenced by the flow which is moving towards blade SS. Further increases the MFR to 1.75%, see Figure 68, the wider η

contour is presented. Approximately 50% of the endwall surfaces on upstream region are protected. However, at region y/p=0.8~1.2, no significant change on the protection layer can be observed in axial direction except in pitchwise direction. As expected, MFR=2.25%, see Figure 69, presented the greatest cooling performance compared to other cases where approximately 90% of protection layer is provided on the endwall surfaces close to the blade LE. The penetration of the leakage flow further downstream of the blade approximately x/C_{ax}=0.7 also can be observed at y/p=0.6~1.2. However, overall η contours illustrate the low η region just downstream of the leakage slot especially at higher MFR. As discussed in previous section, the normal injection of the leakage flow towards mainstream direction influenced to blockage which introduced to the separation flow. As a result, the leakage flow could not stay closer to the endwall resulting lower η at this region. Figure 70 presents the laterally averaged η starting from the slot position, x/C_{ax}=-0.63 and ended at blade TE, x/C_{ax}=1.0. Most of the cases show that the η pick are located at approximately x/C_{ax}=-0.4. This is might be the position where the leakage flow reattached to the endwall surface after the flow separation phenomenon which is occurred just downstream of the slot. The reattachment point of the leakage flow on the endwall surface downstream of the slot is closer to the slot position due to the weaker flow separation by the MFR=0.75%. This was explains by the position of the pick of each cases in Figure 70. The reduce trend of cooling performance is presented towards blade downstream. The leakage flow mixed out with secondary flow which finally prevented most of the leakage flow to stay closer to the endwall surface. This is considered as the main reason of the reduce trend as indicated in the Figure 70. Due to the higher penetration of the leakage flow into the mainstream at higher MFR, the protection region is higher compared to lower cases in axial direction. The cooling performance indicates in Figure 70 is parallel with the η contours presented in Figure 66 (a) ~Figure 69 (a) where the higher performance of η showed by higher MFR. The cooling performance is summarized by determined the mass-averaged of η as shown in Figure 71. The performance can be increased by increasing the amount of the leakage flow. MFR=2.25% illustrates the highest performance among the cases. $\bar{\eta}$ seems to be linearly increased as the MFR increases which approximately 6.7% for every 1% of MFR. Thus, the relationship between $\bar{\eta}$ and MFR can be represented by Eq. 38.

$$\bar{\eta} = 0.067\text{MFR} \tag{38}$$

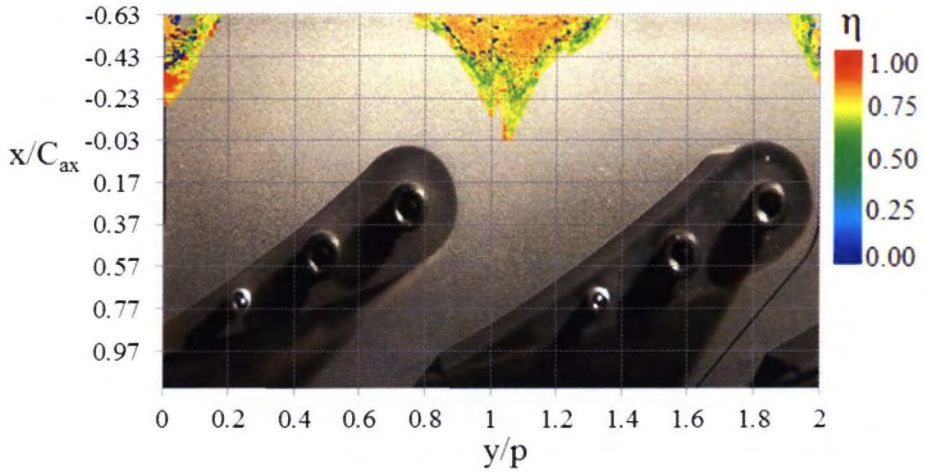

(a) Film cooling effectiveness

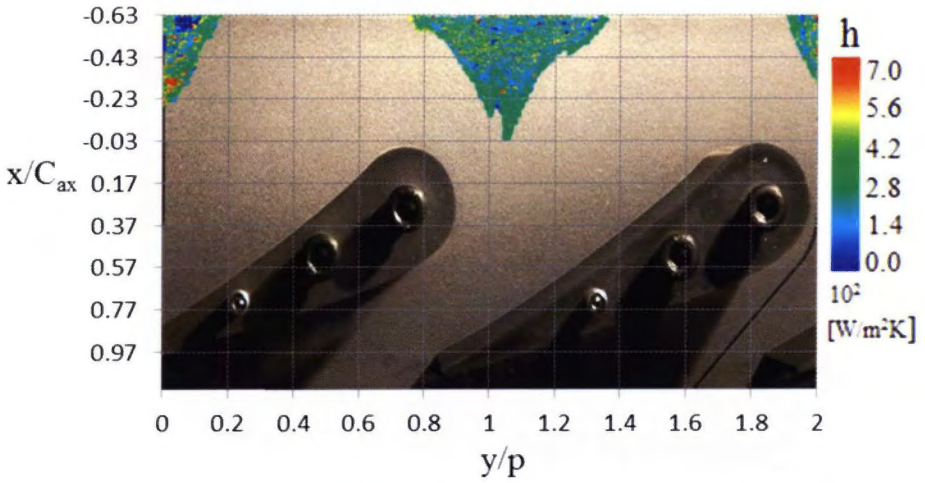

(b) Heat transfer coefficient

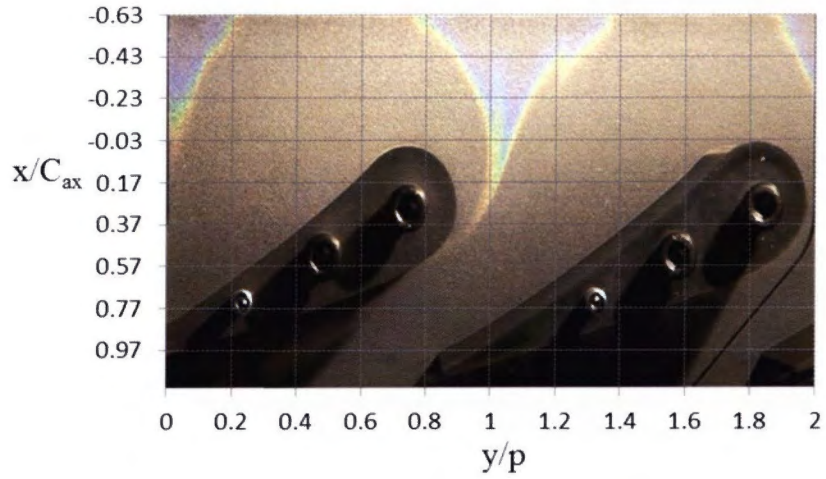

(c) Liquid crystal RGB propagation

Figure 66 Thermal performance for MFR = 0.75%

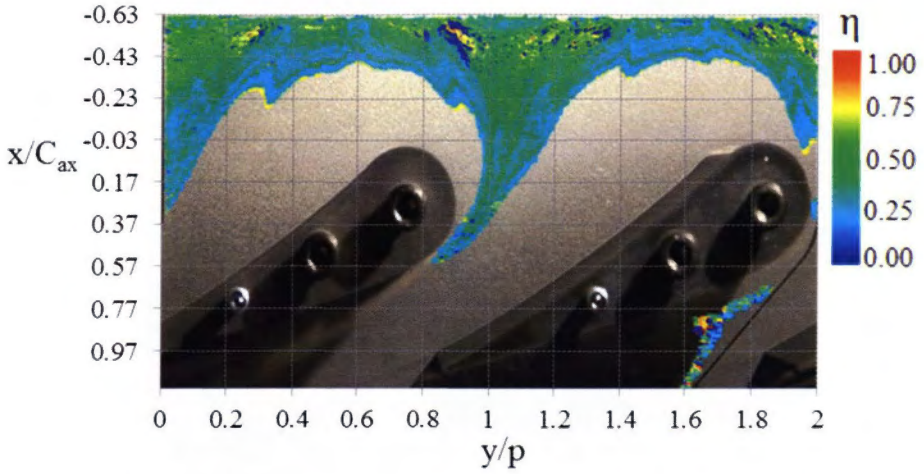

(a) Film cooling effectiveness

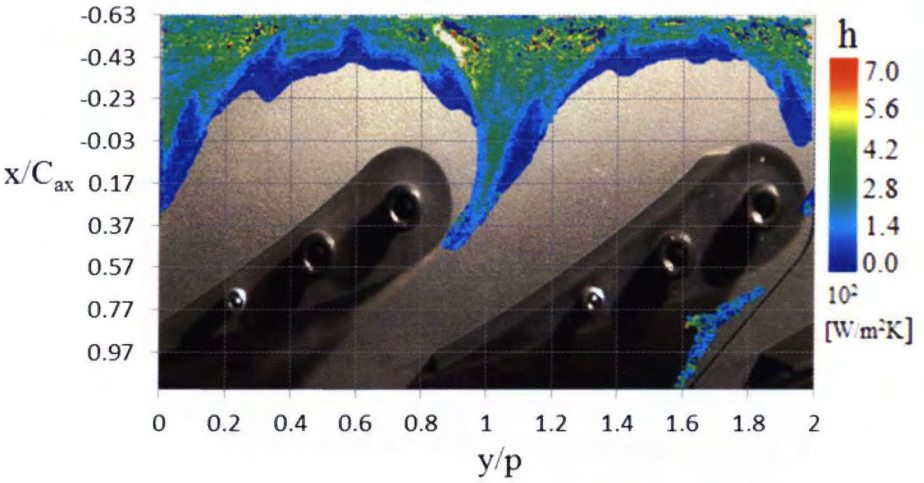

(b) Heat transfer coefficient

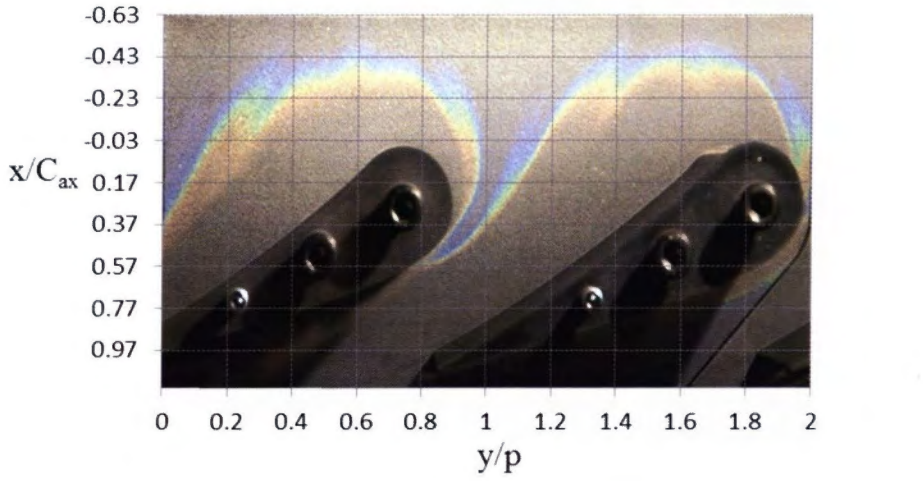

(c) Liquid crystal RGB propagation

Figure 67 Thermal performance for MFR = 1.25%

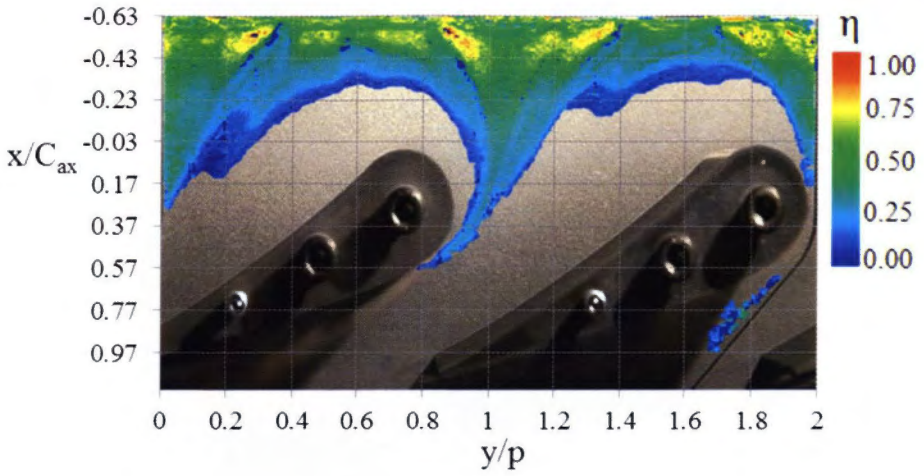

(a) Film cooling effectiveness

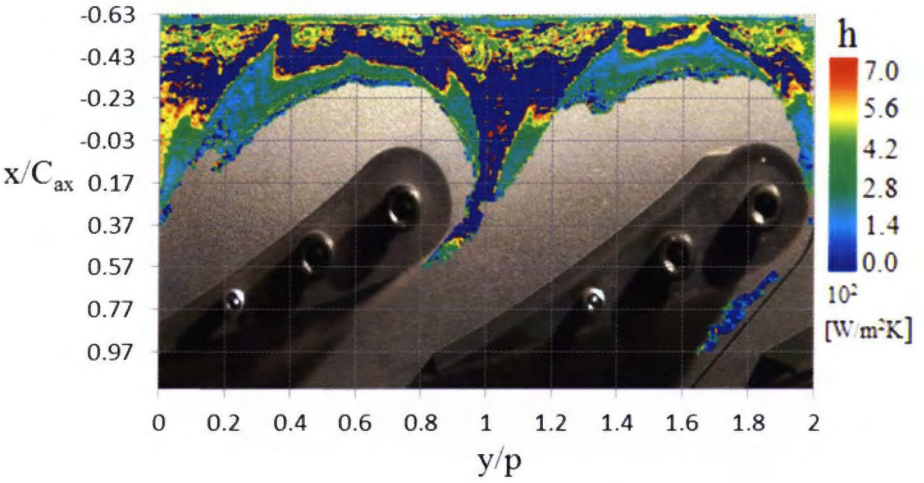

(b) Heat transfer coefficient

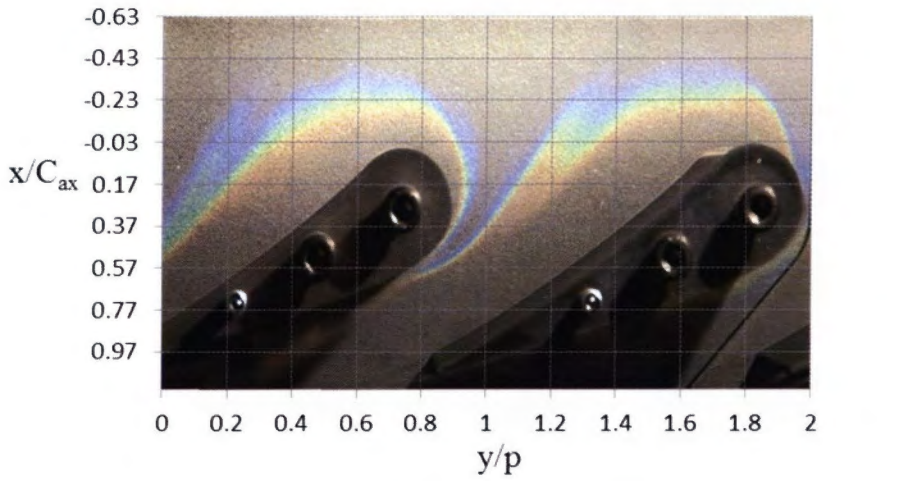

(c) Liquid crystal RGB propagation

Figure 68 Thermal performance for MFR = 1.75%

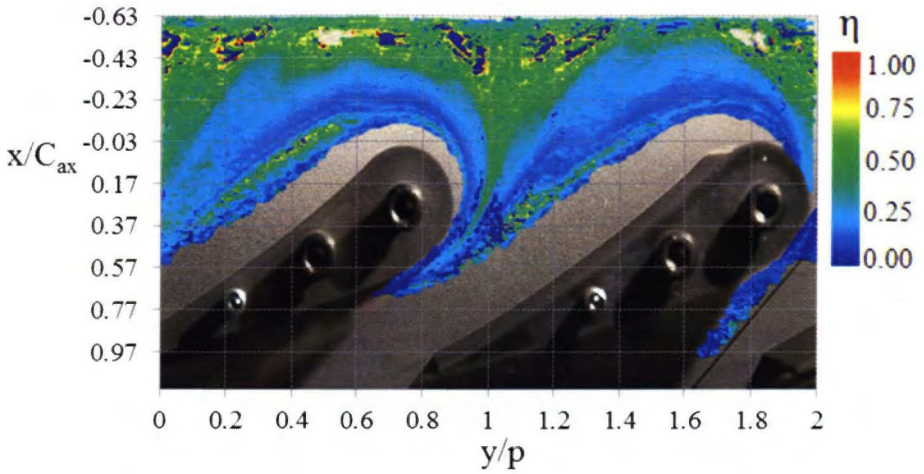

(a) Film cooling effectiveness

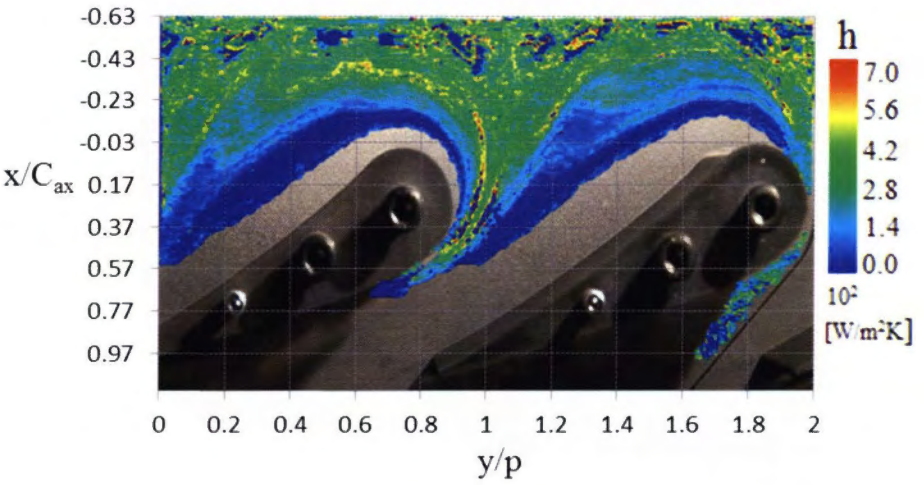

(b) Heat transfer coefficient

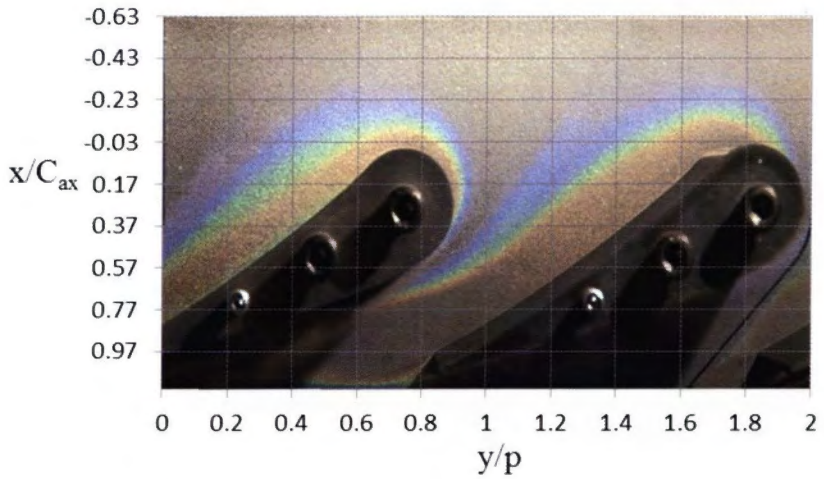

(c) Liquid crystal RGB propagation

Figure 69 Thermal performances for MFR = 2.25%

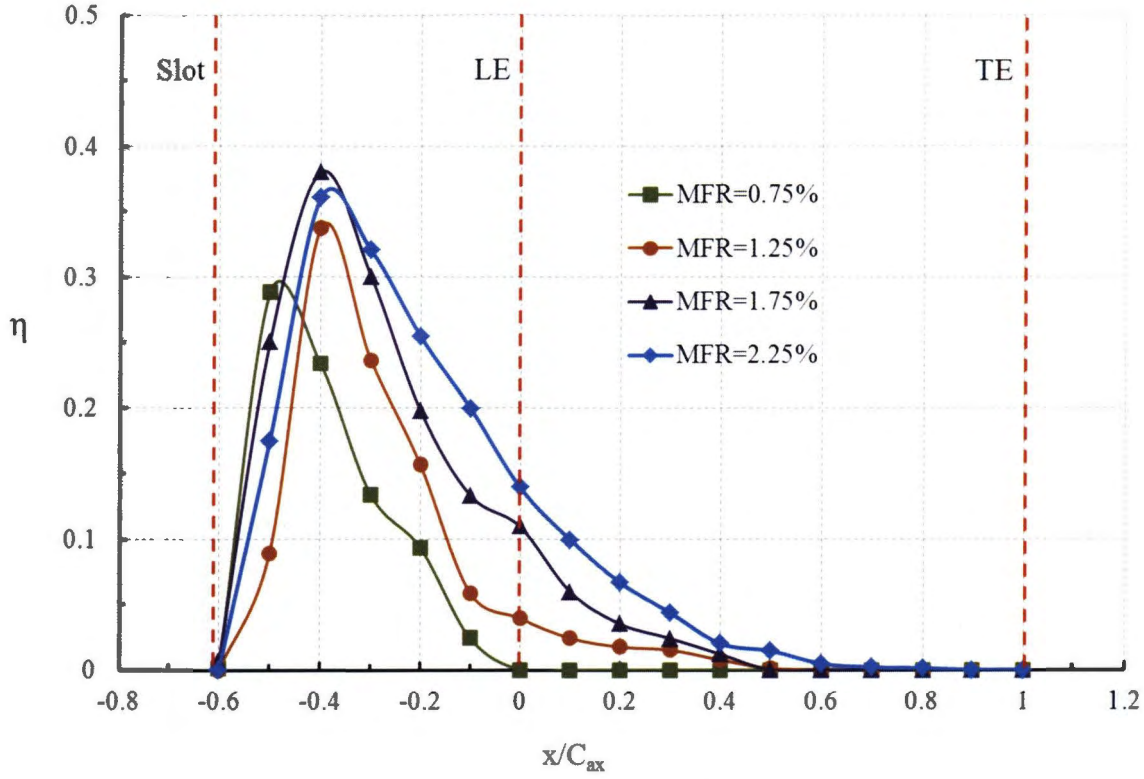

Figure 70 Laterally averaged film cooling effectiveness-EFD

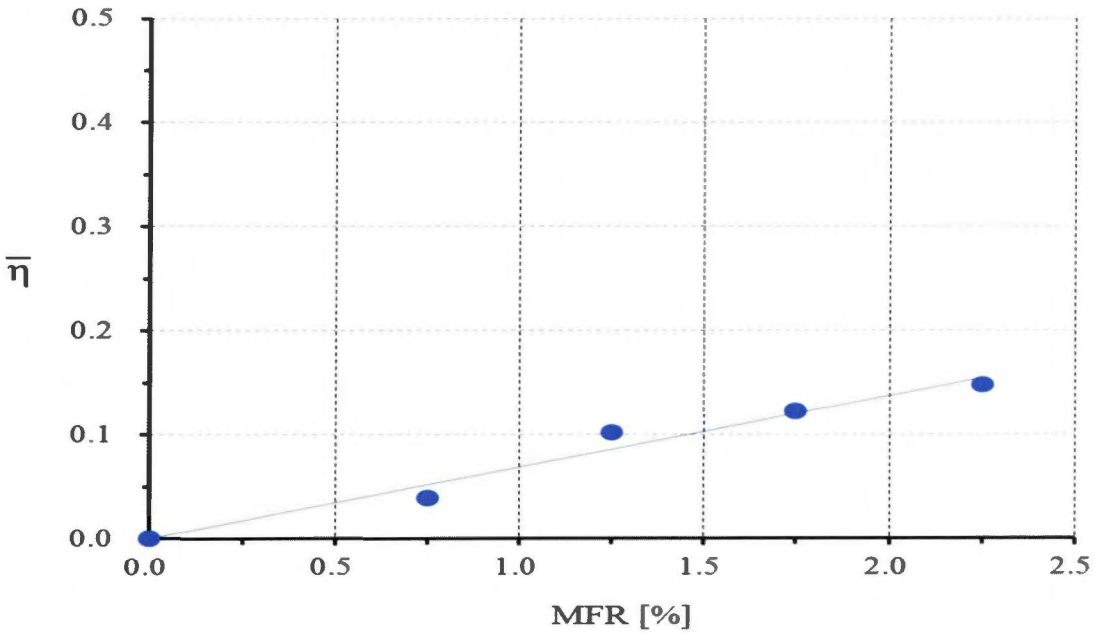

Figure 71 Mass-averaged film cooling effectiveness-EFD

3.5.2 Predicted thermal performances

The performance of the numerical simulation to predict the thermal behaviour under the influenced of the leakage flow has been investigated. As the same turbulence model applied in the aerodynamic prediction, SST was also being applied in this investigation. Figure 72~Figure 75 illustrate the predicted film cooling effectiveness (a) and the heat transfer coefficient (b) for MFR=0.75%, 1.25%, 1.75% and 2.25%, respectively. The region illustrates in the figure is the same which were presented in Figure 66~Figure 69 in order to enable the direct comparison between experimental and the prediction. At MFR=0.75% indicates in Figure 72 (a), the higher η is obtained at the region between y/p=0.8~1.4. Even though it is about 20% wider compared to the measured η, see Figure 66 (a), the prediction presents a similar behaviour of performance indicated by the measurement. CFD also predicted that the leakage flow tends to be penetrated near this region due to the higher pressure close to the stagnation region. As a result, the lower η is presented near the stagnation region with approximately 0.15~0.25 (light blue region). Noted that this protection layer was not be captured by the measurement at the same injection case. The difficulties to obtain almost the same leakage flow profile inside the plenum chamber and the heat loss during the measurement are considered as main reasons. Furthermore, the smaller range of the liquid crystal used to capture the endwall temperature changes also one of the reason. As the MFR increases, the η contour became wider in both axial and pitchwise direction. If the lower η indicates with light blue region is neglected, the similar contour is predicted at MFR=1.25% where it increased to x/C_{ax}=-0.43 and this can be observed along the slot in pitchwise direction. When the MFR increases, the increase trend of η can continuously observed in Figure 74 (a) and Figure 75 (a). However, unlikely the contour obtained by the measurement, no significant changes of the η contour (tail shape contour) showing at region x/C_{ax}=-0.03 towards downstream except the light blue layer. But this tail shape contour exist at the region between x/C_{ax}=0.57~0.67 in both measurement and prediction expect the MFR=0.75%. The heat transfer coefficient parallels to the η contour where they also increases as the MFR increases. The dark blue region illustrates the h with almost close to 0 were captures along y/p=1.0. Noted that this is the region where the leakage flow was accumulated and the formation of the AFV also occurred at this region. The dark blue region also can be seen along the pitchwise direction. This region shifted slightly downstream as the MFR increases. This might be due to the high strength of the separation flow at higher MFR.

At higher MFR of 1.75% and 2.25%, see Figure 74 (b) and Figure 75 (b), the apparent of the dark blue region became more significant at x/C_{ax}=-0.43 and MFR=2.25% illustrates the widest. This is the second separation flow exists between the separation flow vortex and the HSV near the blade LE. Separation flow prevented the leakage flow to stay closer to the endwall surfaces thus low h was obtained. The thermal performance between CFD and EFD is compared based on the mass-averaged η as shown in Figure 76. The red approximate line indicates the linear increase trend is also obtained by the prediction. The relationship between the η and the MFR is describes in Eq. 39.

$$\bar{\eta} = 0.127\text{MFR} \tag{39}$$

Based on Eq. 38 and Eq. 39, the predicted increase rate of η is higher about half of the measurement where the η increase approximately 12.7% for every 1% of MFR. As being explained, due to the different leakage profile, heat loss and the smaller range temperature measurement were the main reasons. In CFD, the adiabatic wall condition was applied to the plenum and endwall surfaces thus the heat loss could be considered as 0.

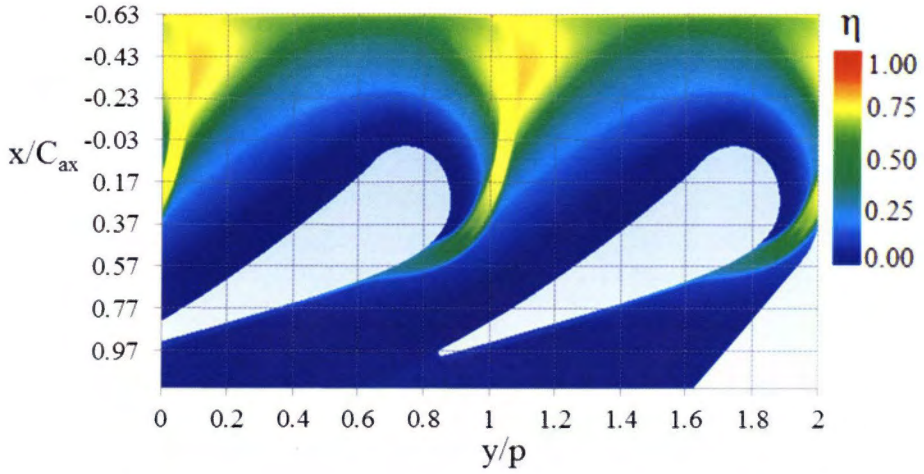

(a) Film cooling effectiveness

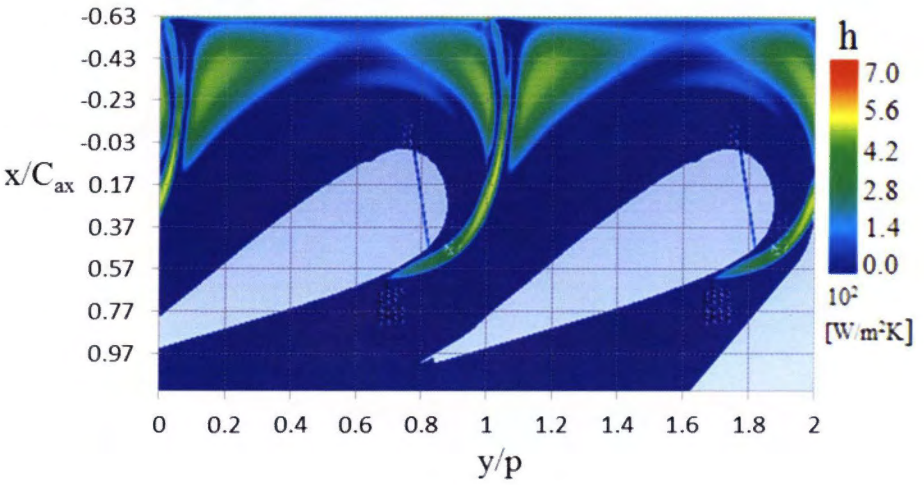

(b) Heat transfer coefficient

Figure 72 Predicted thermal performance for MFR = 0.75%

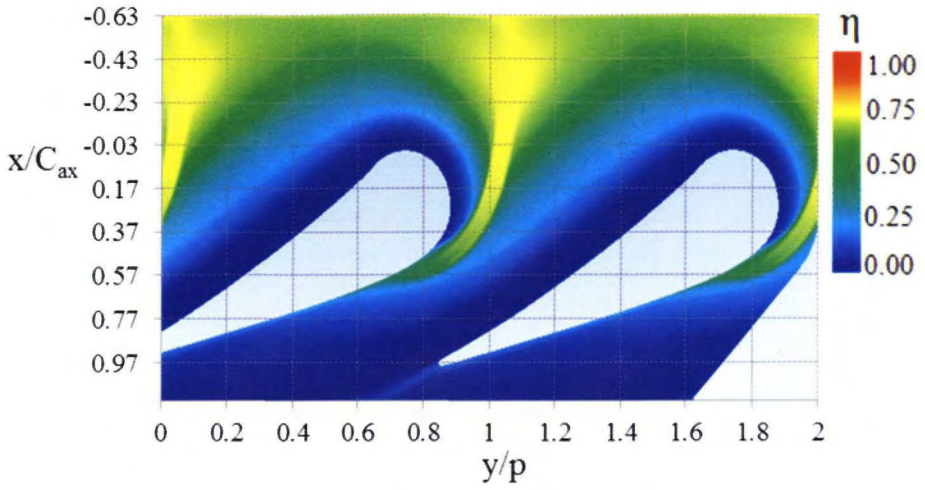

(a) Film cooling effectiveness

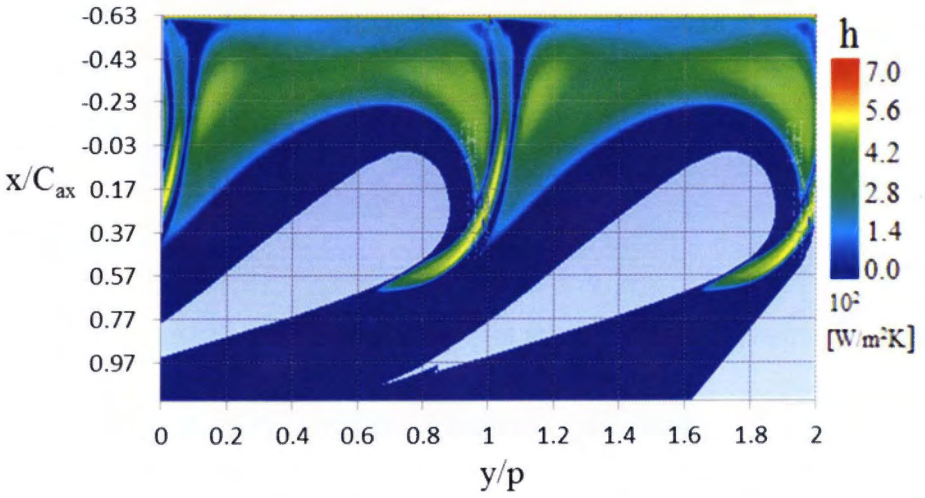

(b) Heat transfer coefficient

Figure 73 Predicted thermal performance for MFR = 1.25%

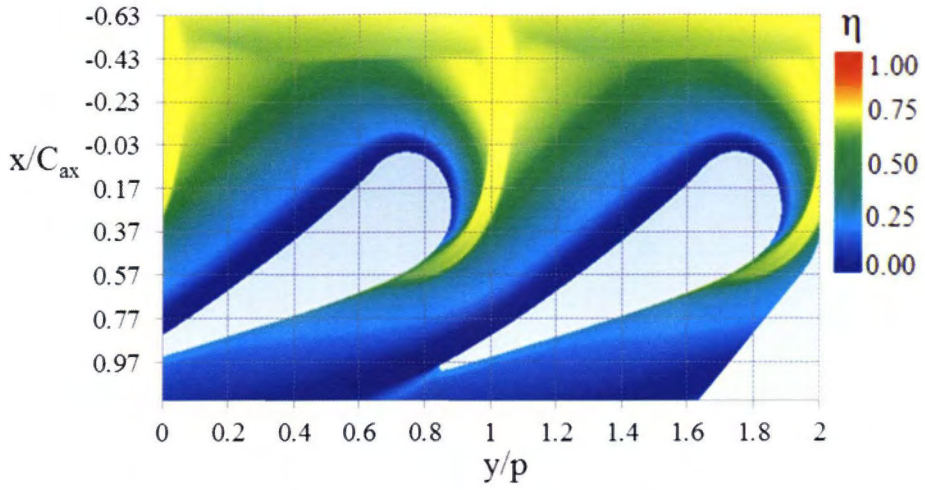

(a) Film cooling effectiveness

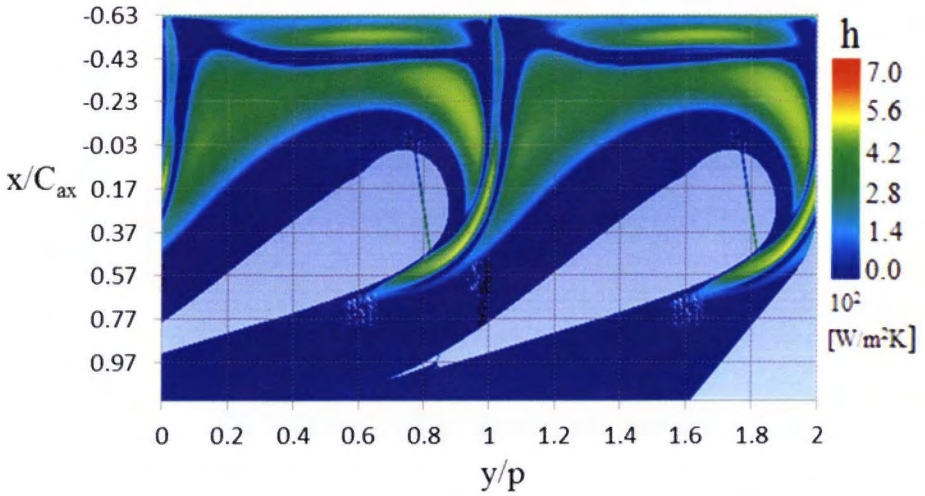

(b) Heat transfer coefficient

Figure 74 Predicted thermal performance for MFR=1.75%

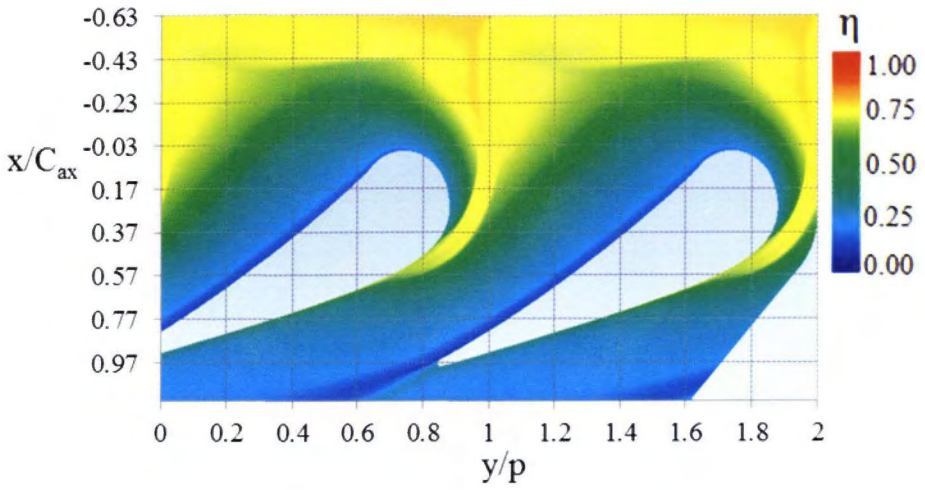

(a) Film cooling effectiveness

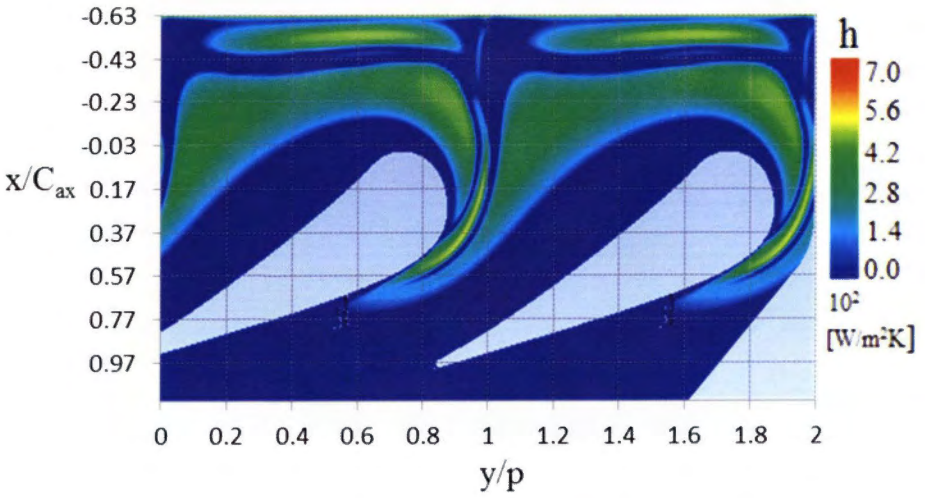

(b) Heat transfer coefficient

Figure 75 Predicted thermal performance for MFR=2.25%

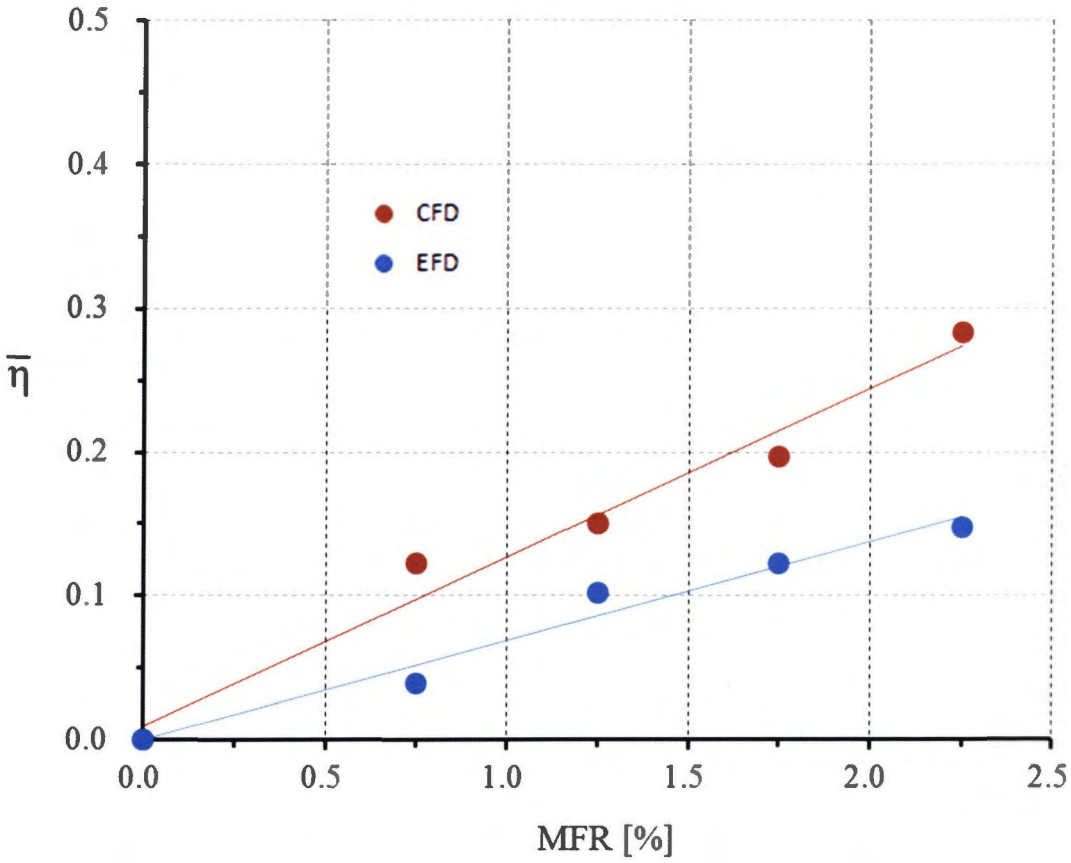

Figure 76 Mass-averaged film cooling effectiveness

3.6 Flow behaviour effects on thermal performances

Figure 77 shows the effect of the secondary flow structures on endwall η distribution in (a) and blade SS surface (b) at MFR=1.25% with the endwall streamline superimposed. Cooling layer provided by the leakage flow seems to be highly influenced by the secondary flows structures. The presence of the PS-HSV and SS-HSV near the blade leading edge leaves the area unprotected. These vortex prevented the leakage flow to go through this area which finally mixed out with the main stream moving towards adjacent blade SS. The contour shows that higher η was observed at the region where the leakage flow was accumulated. Furthermore, the cross flow and the development of the passage vortex (PV) from blade PS to neighbouring blade SS provide a wider cooling coverage on the endwall region near the blade SS instead of blade PS. The merging of PS-HSV and LE-CV to generate a larger PV along the blade SS surface enable the coolant to provide a lower η trail as shown on the right figure. The details of η on the blade SS surface explain in Figure 78 (a) and Figure 78 (b) for MFR=1.25 and MFR=2.25%, respectively. ζ contour at Plane B which were presented in Figure 55 and Figure 56 also shown on the right figure. As shown in Figure 78, the η strikes on the blade SS illustrates the reattachment position of PS-HSV which was coming from adjacent blade PS. The higher MFR cases with high fluid momentum enable to cross the mainstream with higher flow deviation thus could reached the neighbouring blade SS earlier. Furthermore, the wider η in spanwise direction ($Z_H > Z_L$) explains that higher MFR injection lifted off blade surface in higher position due to the higher C_{SKE}.

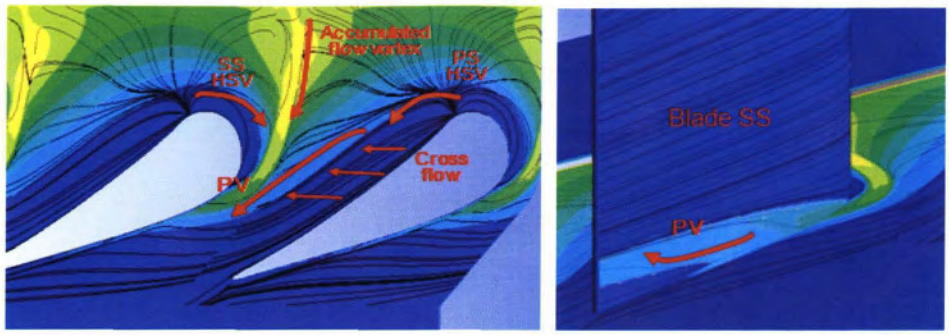

(a) Endwall side (b) Blade SS side

Figure 77 η contours influenced by secondary flow behaviour

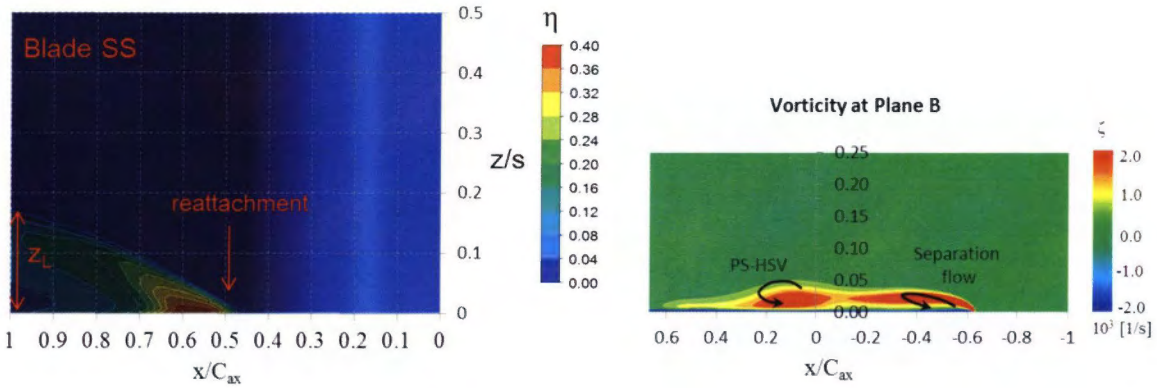

(a) η on blade SS (left) and ζ on Plane B (right) at MFR=1.25%

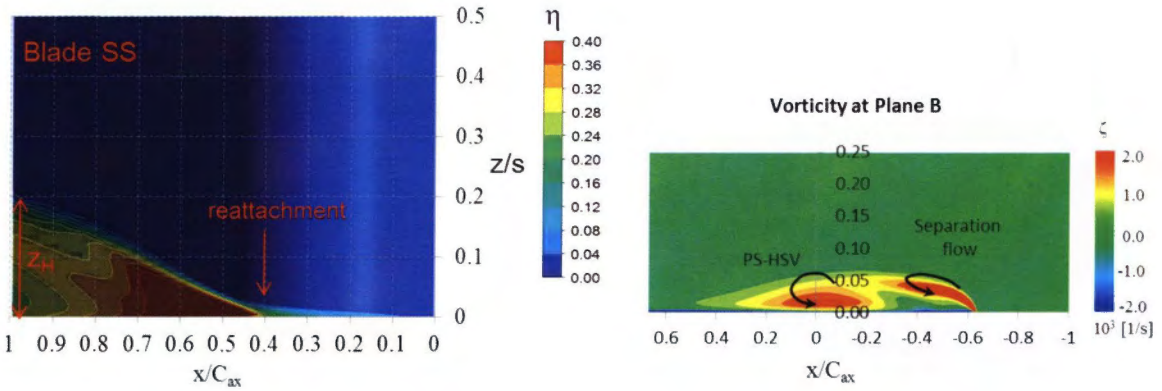

(b) η on blade SS (left) and ζ on Plane B (right) at MFR=2.25%

Figure 78 Effect of flow structures on blade SS film cooling effectiveness

3.7 Overall performances

Based on the discussion in previous sections, it is clearly explain that the leakage flow has a high potential to provide the protection layer on the endwall surfaces. However, the changed of the existing flow structures caused by leakage injection resulting the increases of the C_{pt}. This cannot be neglected since a significant change of C_{pt} contours were captured in both EFD and CFD. The relationship between the C_{pt} and η is presented in Figure 79. The approximated lines are also drawn and compared between EFD and CFD. Both EFD and CFD illustrate that the C_{pt} and η are proportional to the MFR where the higher the MFR, the wider the protection layer and the loss continuously increases. The relationship between C_{pt} and η can be represented in Eq. 40 and Eq. 41 for EFD and CFD, respectively.

$$\text{EFD: } C_{pt} = 1.21\,\overline{\eta} + 1.271 \tag{40}$$

$$\text{CFD: } C_{pt} = 0.68\,\overline{\eta} + 1.331 \tag{41}$$

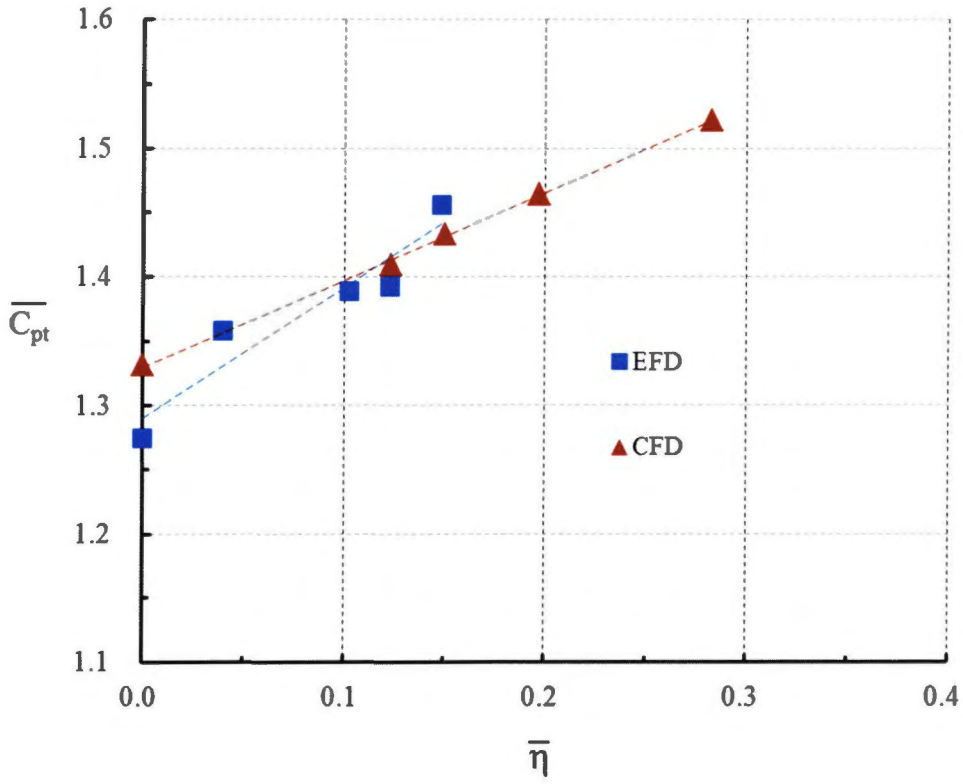

Figure 79 Aero-thermal performance of leakage flow

Chapter 4

Slot Modifications Effect by Prediction

This chapter provides details on the extended studies in order to improve current aero-thermal performance as discussed in Chapter 3. The modification of slots is expected to improve their performance. The numerical investigation on the slot configuration focuses on the slot orientation and its position from the blade LE. The leakage flow with various injection angles, β are compared to the baseline configuration with 90° injection. For the slot position studies, the slot with various position, *l* from the blade LE were compared to the baseline slot position which is located at $-0.63C_{ax}$ upstream from blade LE. This chapter provides the prediction results to show their effect on current aero-thermal performance. This investigation aims the improvement of the aero-thermal performance which could be considered in actual gas turbine application.

4.1 CFD modeling

Based on the good agreement that have been achieved between the EFD and CFD for baseline configuration as presented in Chapter 3, the present section intended to predict the performance of leakage flow injection with a different slot configuration. The modification of the slot in term of slot orientation and position were considered could provide some modification on the existing performance. In order to obtain a direct comparison with the predicted baseline configuration, the same mesh and grid topology was applied to the mainstream and the blade domain. The only change that was made is the slot configuration. The injection angle, β=90° and position, $l = x/C_{ax} = -0.63$ which was presented in the previous chapter is considered as the baseline slot configuration. As shown in Figure 80, the slot were oriented to three different injection angles, β=60°, 45°and 30°. However, in order to see their

effect only by the injection angle, all cases were fixed at slot position, l =-0.63 where it is the same position with the baseline slot configuration. Since the slot was inclined, the slot width, d_b = 4 [mm] is actually become shallower with d_β = 4.Sin(β) [mm]. The endwall thickness was fixed at $0.24C_{ax}$ for all cases. The effect by the slot position was predicted by another three slot positions. Since l =-0.63 is considered as baseline slot position, the slot was firstly shifted to l =-0.90 where it was move away from the blade LE. Due to the limitation of the slot distance in the real gas turbine, the slot was also move closer to the blade LE with two cases of l =-0.36 and -0.10. The thermal and aerodynamics performance by the slot modification will discuss in the next section.

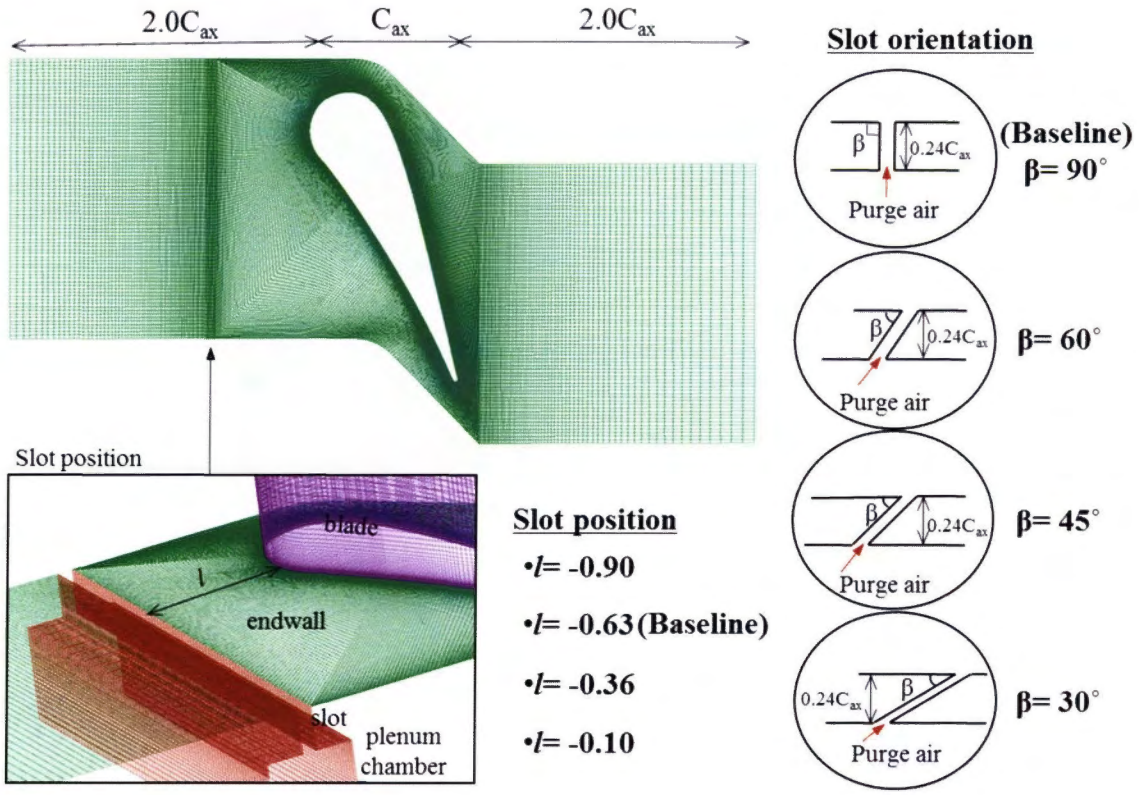

Figure 80 CFD modeling for slot orientation and position

4.2 Leakage flow performance influenced by slot orientation at l=-0.63

4.2.1 Aerodynamics performances

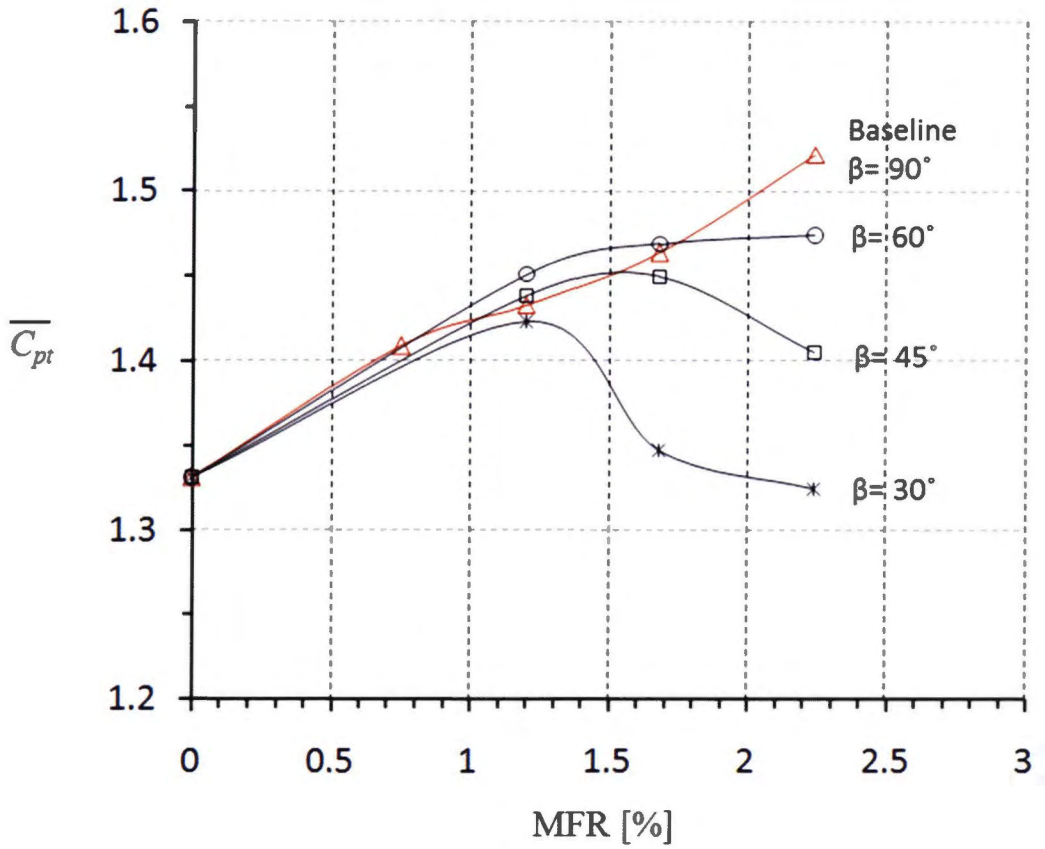

Figure 81 Mass averaged C_{pt} by the effect of β at l=-0.63

Five cases of MFR, 0.75%, 1.25%, 1.45%, 1.75% and 2.25% have been predicted for each configuration. Mass averaged C_{pt} was determined and plotted in Figure 81 to present the slot performance in comparison to baseline configuration indicated by the red line. Regardless the β, injecting a leakage flow up to MFR=1.25% is predicted to increase the loss. However, not the case for the higher MFR of 1.75% and 2.25% where the loss started to reduce slowly for β= 60°cases. Continuously shallower the β to 45° and 30°, the loss indicates the decrease trend as the MFR being increased. The $\bar{C}_{pt}$ not only lower than the baseline case but also in comparison with the lower MFR showing by the same slot configuration particularly at

MFR=2.25%. According to the trend shown in Figure 81, the shallower the injection angle, the $\bar{C}_{pt}$ will starts to reduce at lower level of MFR. Figure 82 and Figure 83 present the C_{pt} contours for MFR=1.25% and 2.25%, respectively in comparison with different β. At MFR=1.25%, the shape of first loss core significantly changed at β =60° (Figure 82 (a)) and C_{pt} seems became wider at the bottom side of the core. In the contrary, the third core slightly reduced and the region exists closer to the endwall side. Further reduce the β to 45° and 30° as shown in Figure 82 (b) and (c), both loss cores reduced especially at β =30°, the third core is very weak. At MFR=2.25%, a very interesting results is shown in Figure 83 because it's contradicting with C_{pt} contour shown by the baseline case (Figure 52 (a)) when the MFR being increases. Especially for β =30°, see Figure 83 (c), the loss drastically reduced where the second and third loss cores mostly eliminated by leakage flow injection. These explain that the strength of the TE-CV and AFV became weaken and the influences of these vortexes to loss almost cannot be seen. The reduce strength of the PS-HSV also being explained by the deformation of the first loss core in the same figure. This phenomenon is parallel to the loss distribution shown in Figure 82.

The details flow structures by each β in the blade passage are shown in Figure 84~Figure 86 for MFR=2.25% since a very interesting result has been shown by the case. All β cases captured the presence the PS-HSV but the secondary flow seems to be modified by this slot configurations. The modification of the secondary flow structures is predicted to improve the blade passage by the less strength of the vortex core shown in each figure. In comparison with the baseline slot configuration at similar MFR, see Figure 56, the changes of β to a shallower angles seem to reduce the strength of the HSV indicated by the flow streamline at stagnation plane. At MFR=2.25%, the leakage flow has enough momentum and can easily be penetrated into the mainstream includes the blade stagnation region. By normal injection, the penetration of the leakage flow influenced to the flow blockage and high flow separation occurred at downstream of the slot. However, the less flow blockage at this region was predicted by shallower injection consequently reduce the strength of HSV. The smaller diameter of vortical structure might explain the reduce strength of HSV. By β =30° as shown in Figure 86, the occurrences of the flow separation almost cannot be seen and the HSV with a small diameter shifted closer to the blade LE wall. The development of PS-HSV has been observed by the ζ plotted on Plane B. In comparison with baseline slot configuration (Plane B ζ in Figure 56), PS-HSV seems to slightly shifted towards downstream by β =60°and

closer to blade PS by β =45° and β =30°, see Plane B in Figure 84~Figure 86. Noted that this phenomenon is contradicting with usual case where the PS-HSV is expected to cross the mainstream before lifted-off neighboring blade SS. Additionally, in comparison with the baseline case with no leakage flow injection, see Figure 54, the existing flow structures is actually being improved without PS-HSV crossing the mainstream thus less flow deviation occurs. This is due to the weaker PS-HSV with a low fluid momentum unable to cross the mainstream and it highly influenced by the higher momentum of leakage flow. This means that the formation of passage vortex near the blade SS occurs without the presence of PS-HSV and this might be the reason of the lower C_{pt} contour obtained by this case.

The most significant change on the secondary flows is the strength of the AFV reduced by β =45°and the formation of such vortex almost cannot be observed by β =30°. The endwall flow streamline illustrates in Figure 87 explains the formation of AFV by β =60° and the elimination of the AFV by shallower injection angle at β =30°. In usual case, the leakage flow tends to migrate toward blade center due to the high pressure region near the blade stagnation. However, as explained above, inclined slot toward this region could provide enough fluid momentum thus they can easily be penetrated and reached the blade PS wall before being deflected particularly by β =30°, see Figure 87 (c). Deflected leakage flow leaves a significant flow behavior indicated by the vortex core on the blade PS defined by DFV. The presence of DFV also can be observed in Plane B indicated by negative ζ rotating in clock wise direction. At β =30°, DFV seems to be appeared till the blade midspan.

The vortex core propagation near the blade TE by each β are presented in Figure 88~Figure 90. The ζ contour at Plane $1.25C_{ax}$ is also illustrates in the same figures. By β =60°, the influenced of the AFV which contributed to the third loss core (see Figure 83 (a)) is clearly shown by the negative ζ region in Figure 88 (a). However, the ζ is slightly lower in comparison with baseline slot configuration (see Figure 60) resulting lower losses. By β =45° and β =30° shown in Figure 89 and 90, the first loss core is predicted to be associated by the LE-CV alone without the combination with the PS-HSV. This illustrated by the lower ζ region parallel to the position of first loss core shown in Figure 83 (b) and (c). The reduced strength and elimination of the AFV by β =45° and β =30°, respectively is considered as the major change which contributed to the reduce loss where the appearance of the AFV in the ζ contour almost cannot be seen.

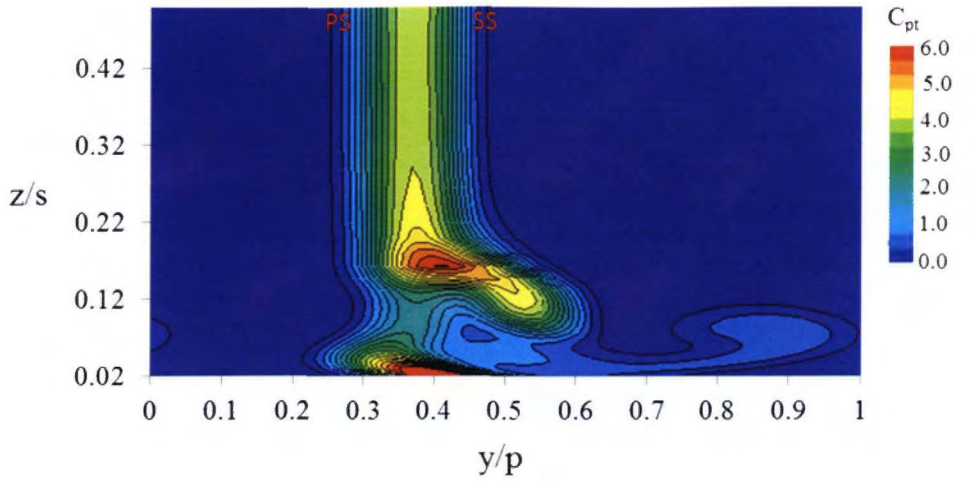

(a) β= 60°

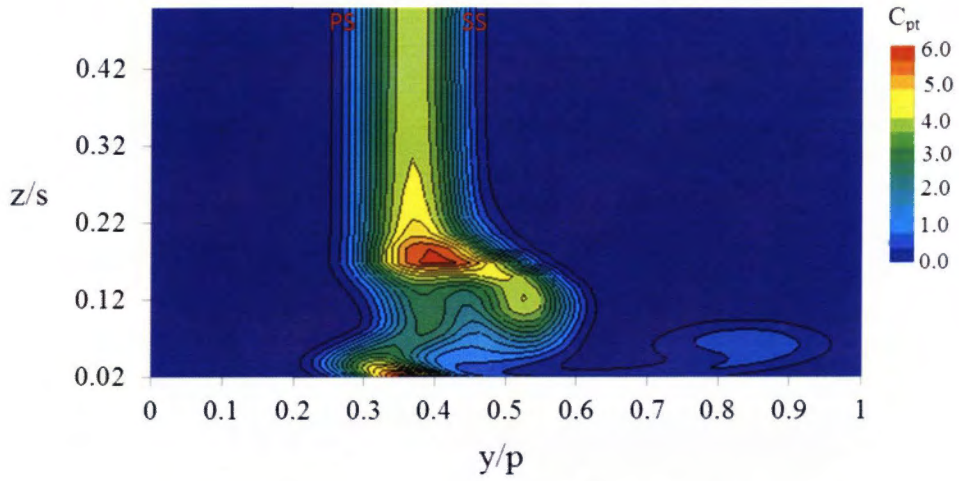

(b) β= 45°

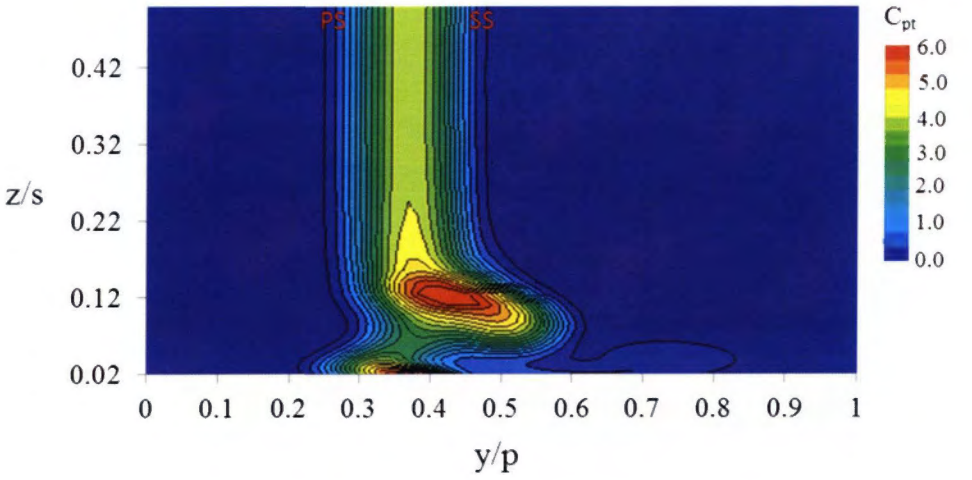

(c) β= 30°

Figure 82 Predicted C_{pt} contour at MFR-1.25% by three different β

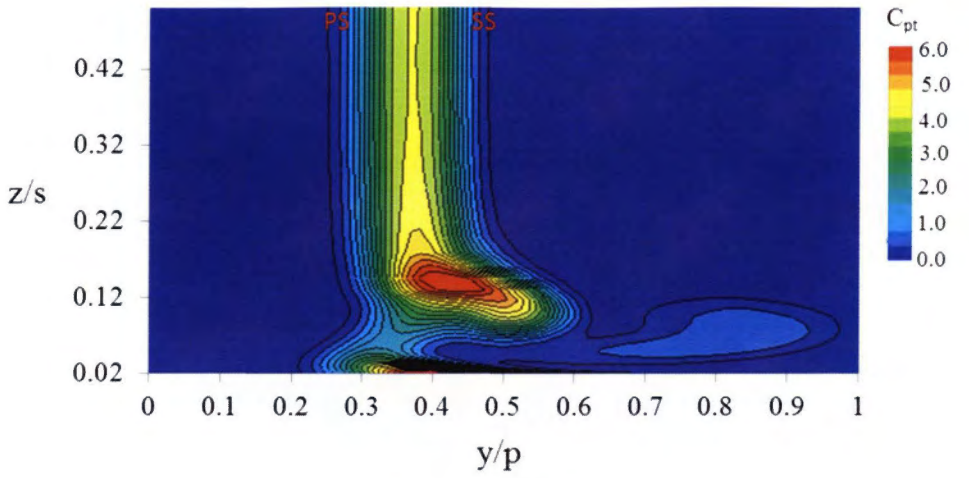

(a) β= 60°

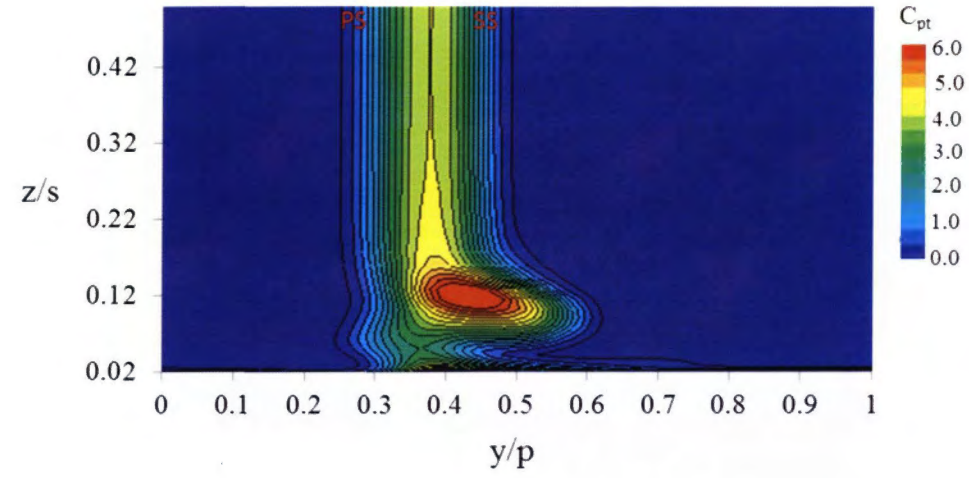

(b) β= 45°

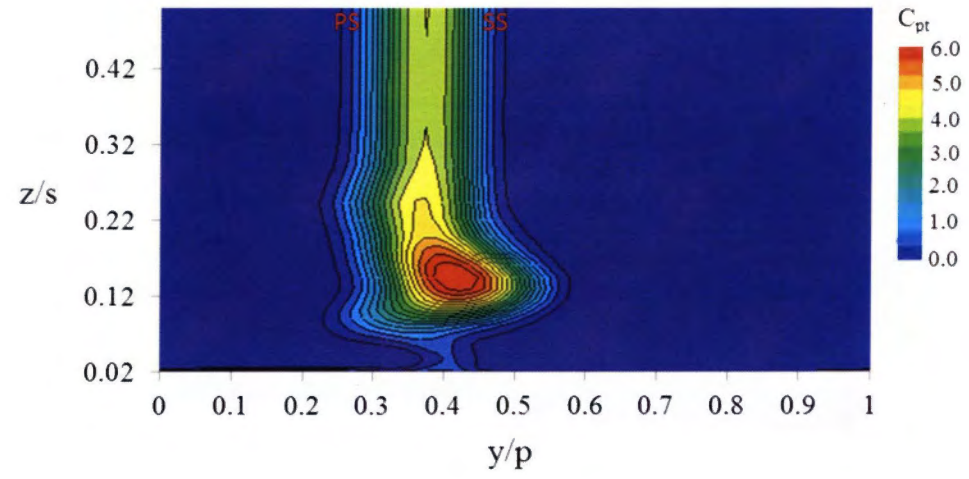

(c) β= 30°

Figure 83 Predicted C_{pt} contour at MFR-2.25% by three different β

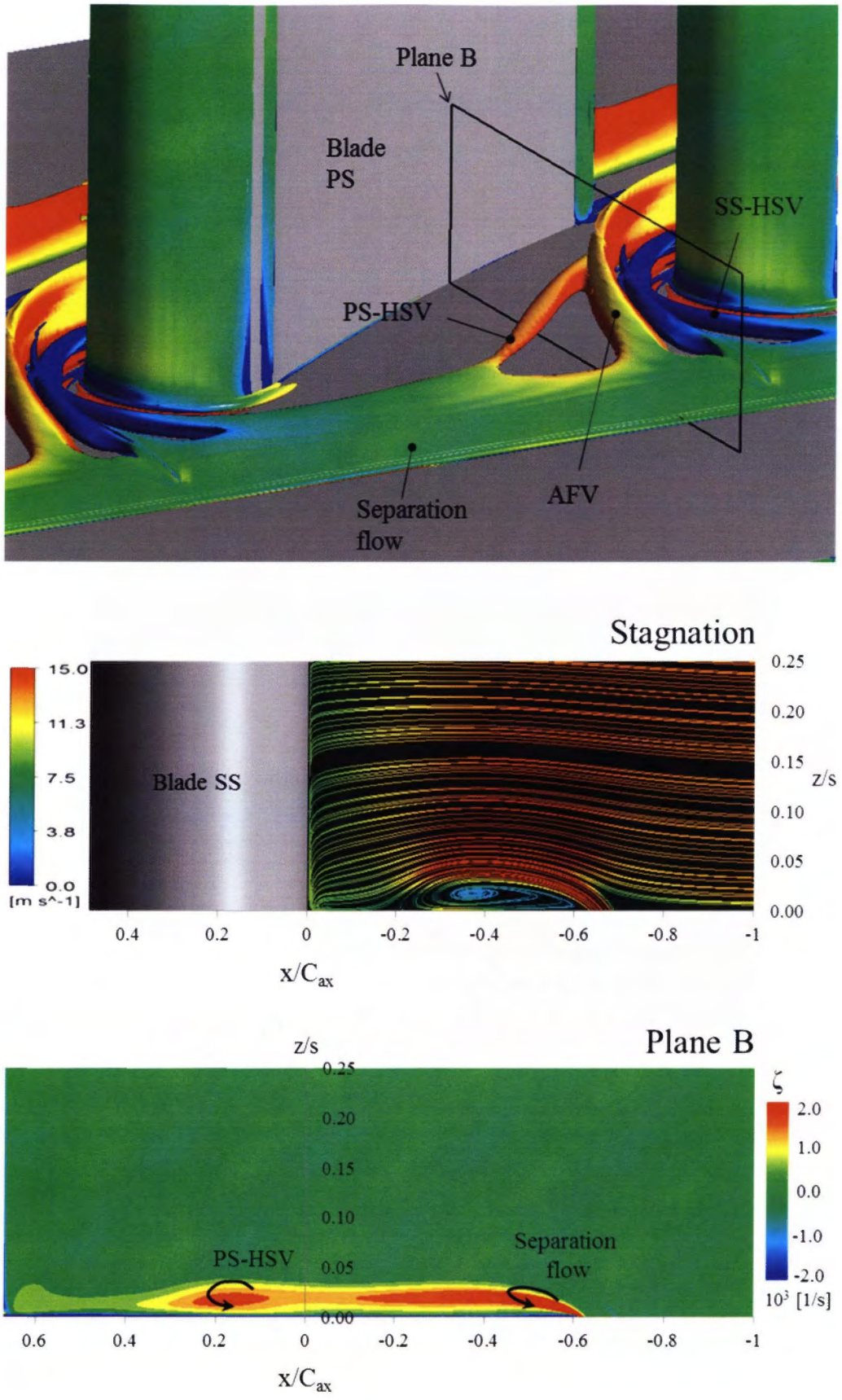

Figure 84 Predicted flow structures near blade LE at MFR=2.25% by β=60°

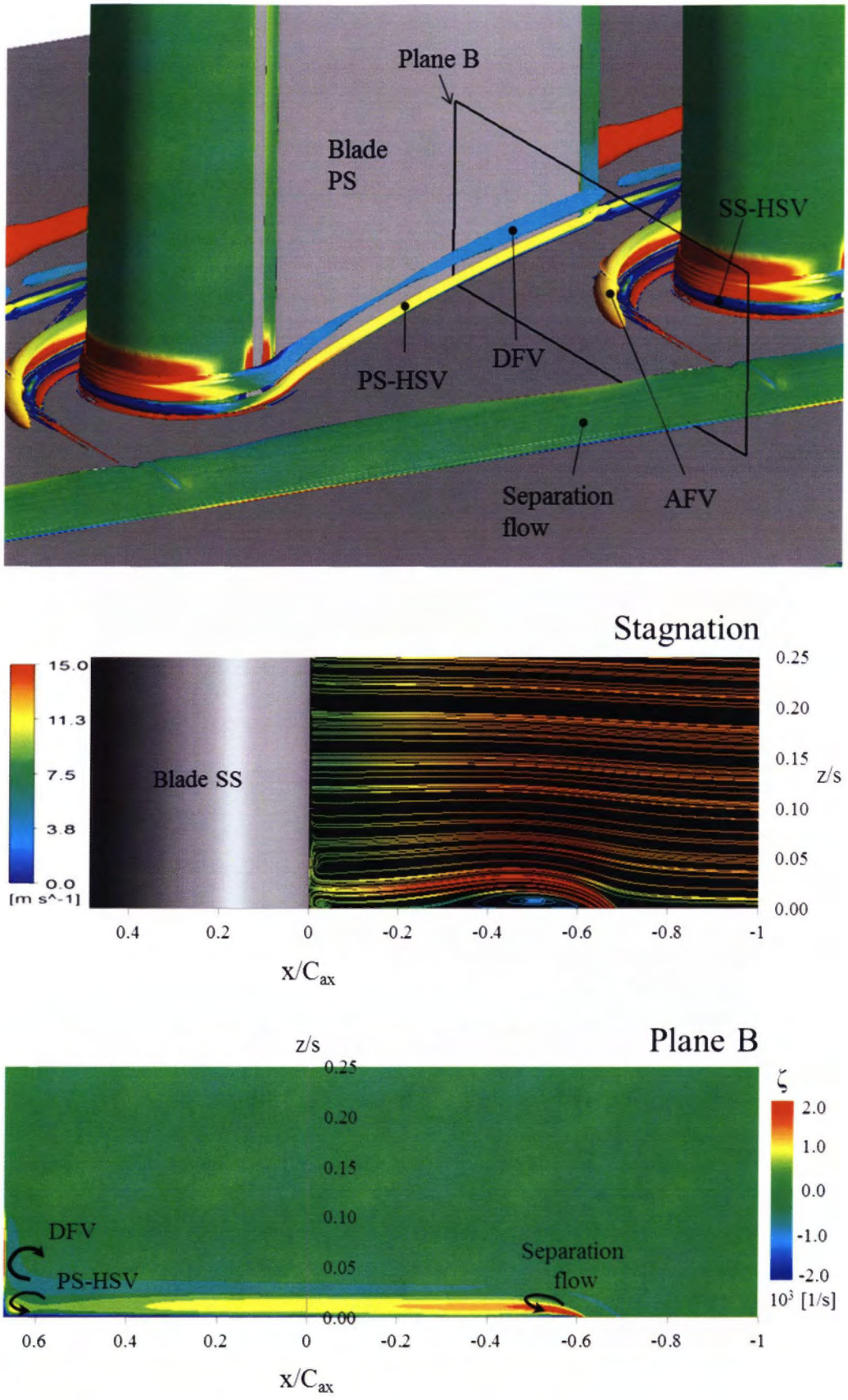

Figure 85 Predicted flow structures near blade LE at MFR=2.25% by β=45°

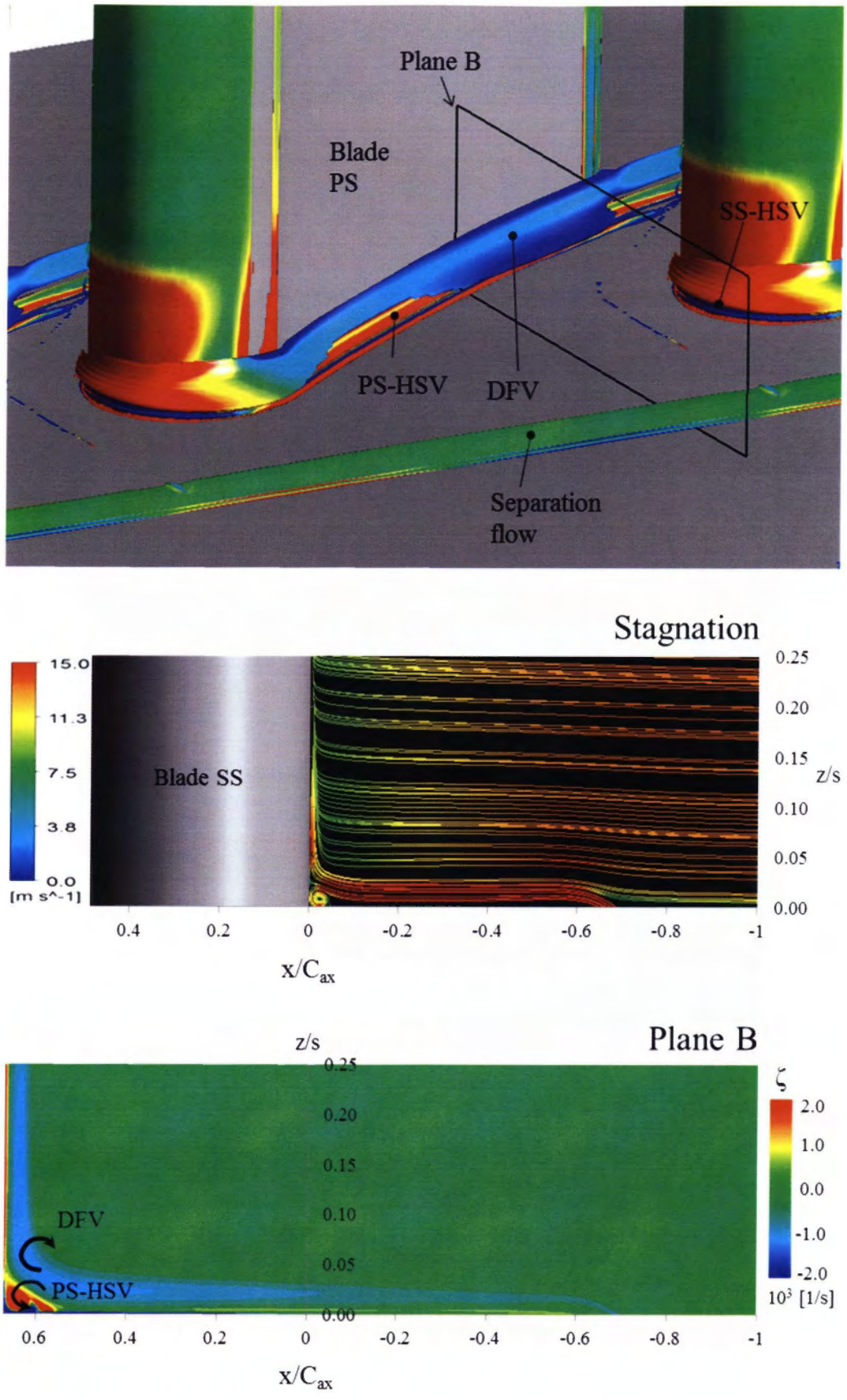

Figure 86 Predicted flow structures near blade LE at MFR=2.25% by β=30°

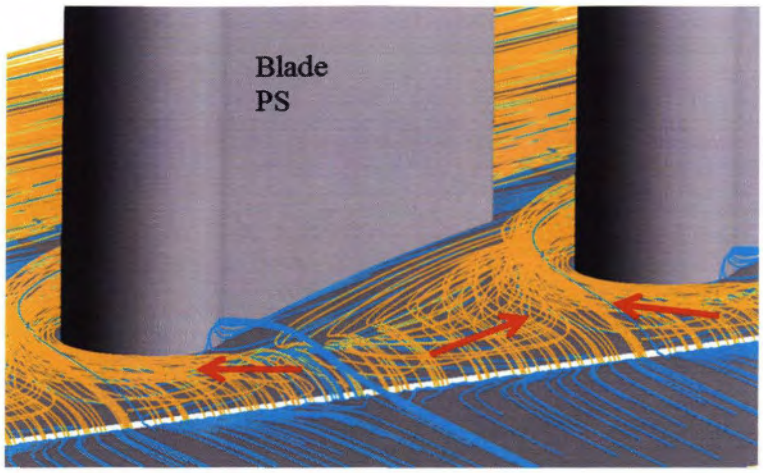

(a) Endwall streamline by β=60°

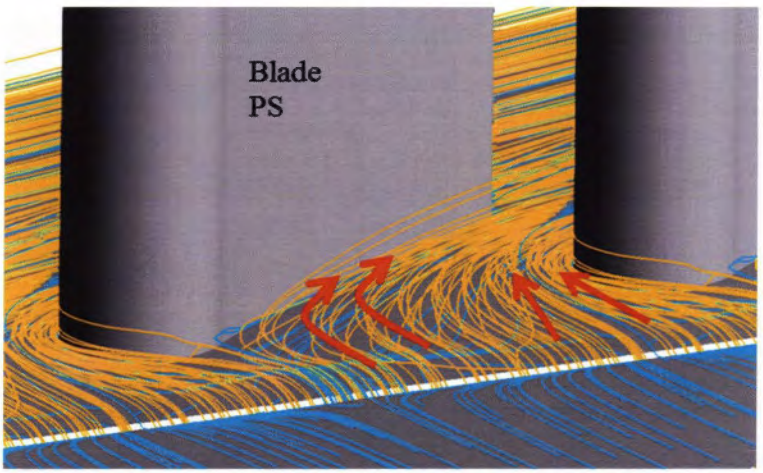

(b) Endwall streamline by β=45°

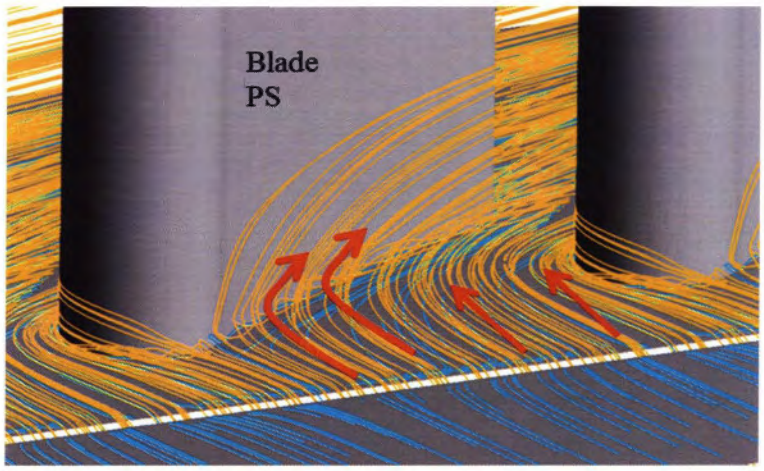

(c) Endwall streamline by β=30°

Figure 87 Predicted flow streamline on endwall region by slot orientation effect

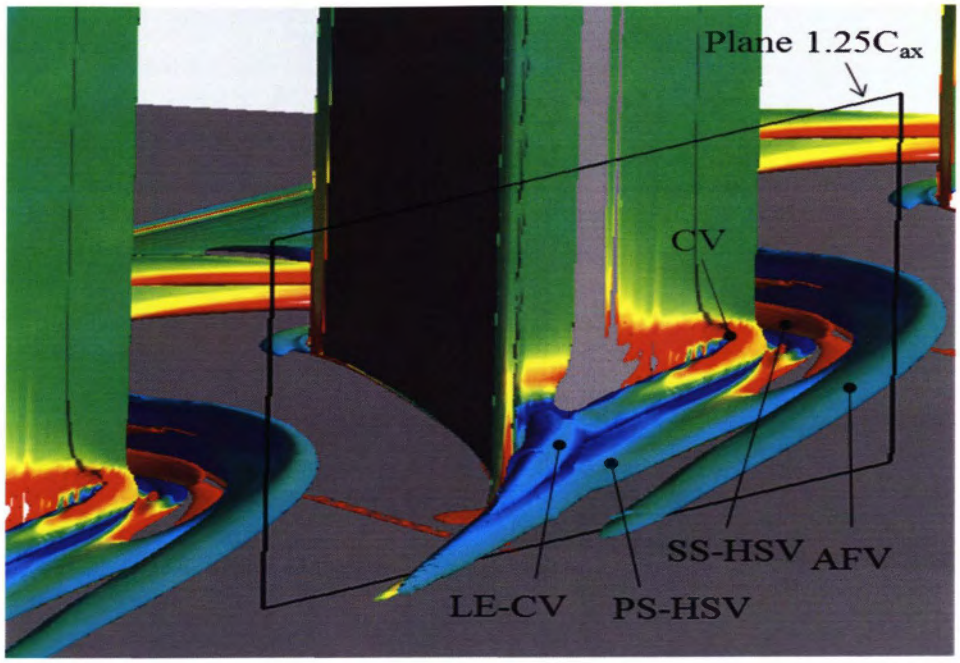

(a) Vortex core

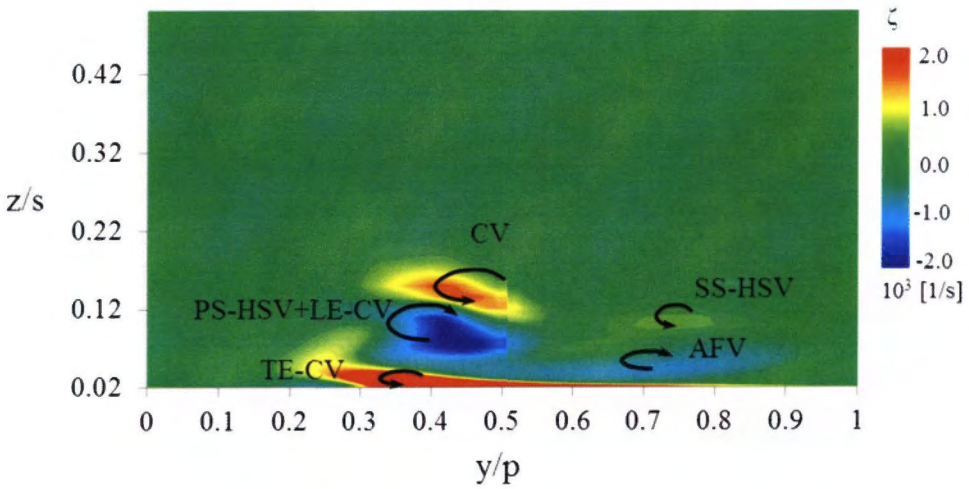

(b) Plane 1.25C$_{ax}$ vorticity

Figure 88 Predicted flow structures near blade TE at MFR=2.25% by β=60°

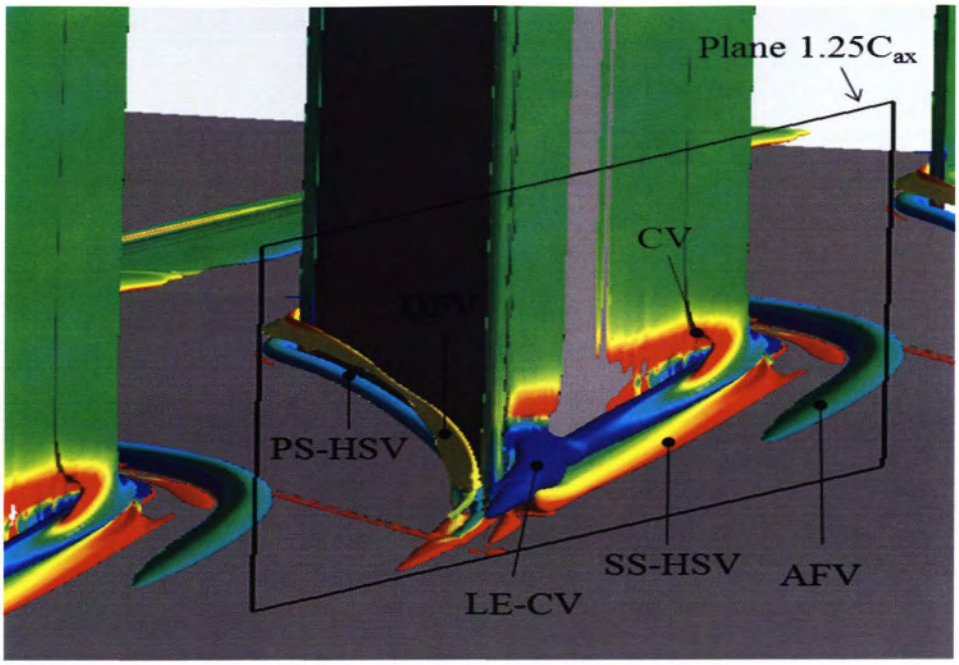

(a) Vortex core

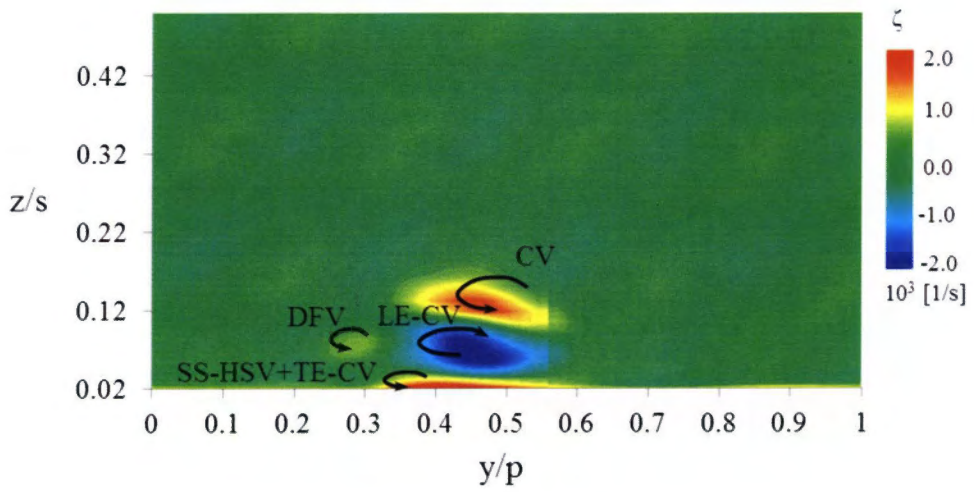

(b) Plane 1.25C$_{ax}$ vorticity

Figure 89 Predicted flow structures near blade TE at MFR=2.25% by β=45°

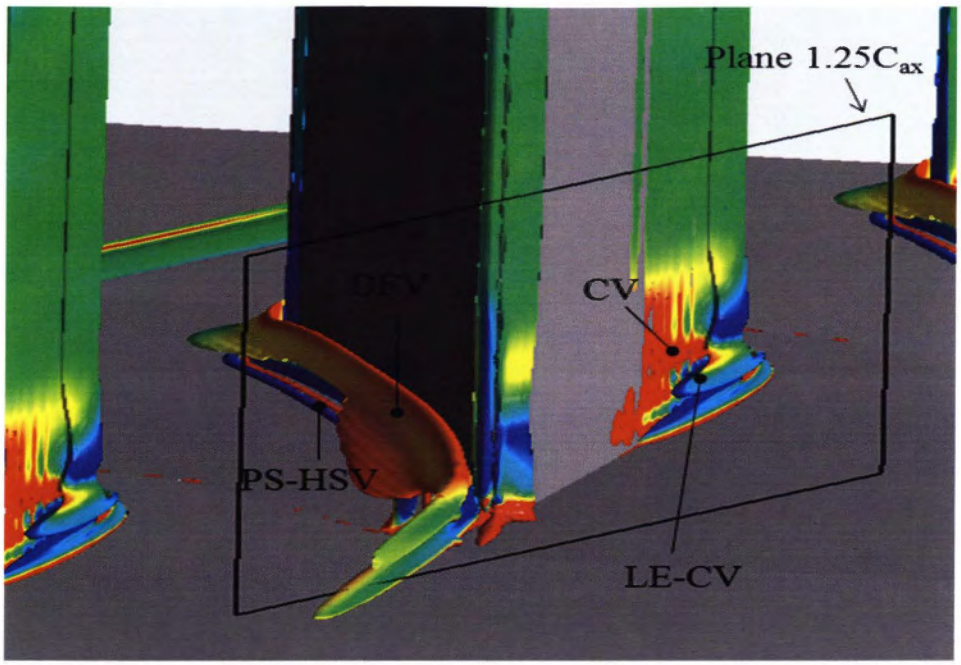

(a) Vortex core

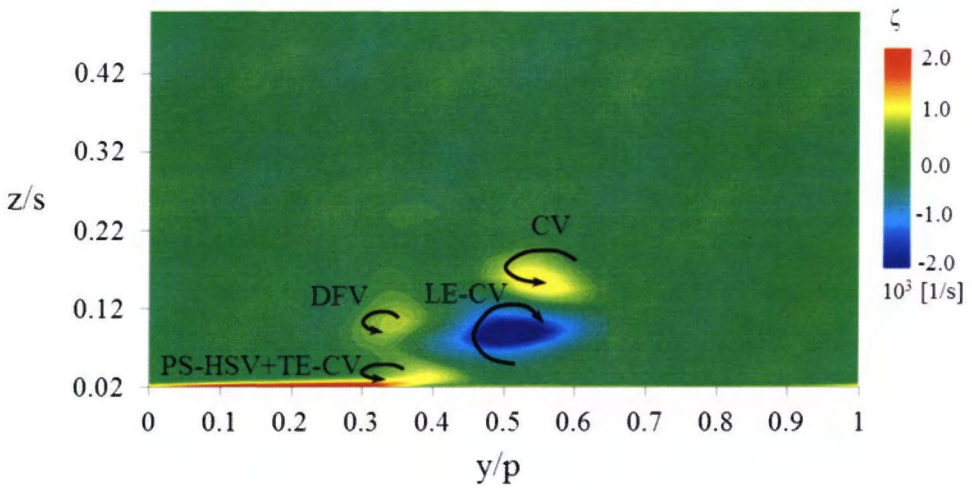

(b) Plane $1.25C_{ax}$ vorticity

Figure 90 Predicted flow structures near blade TE at MFR=2.25% by β=30°

4.2.2 Thermal performances

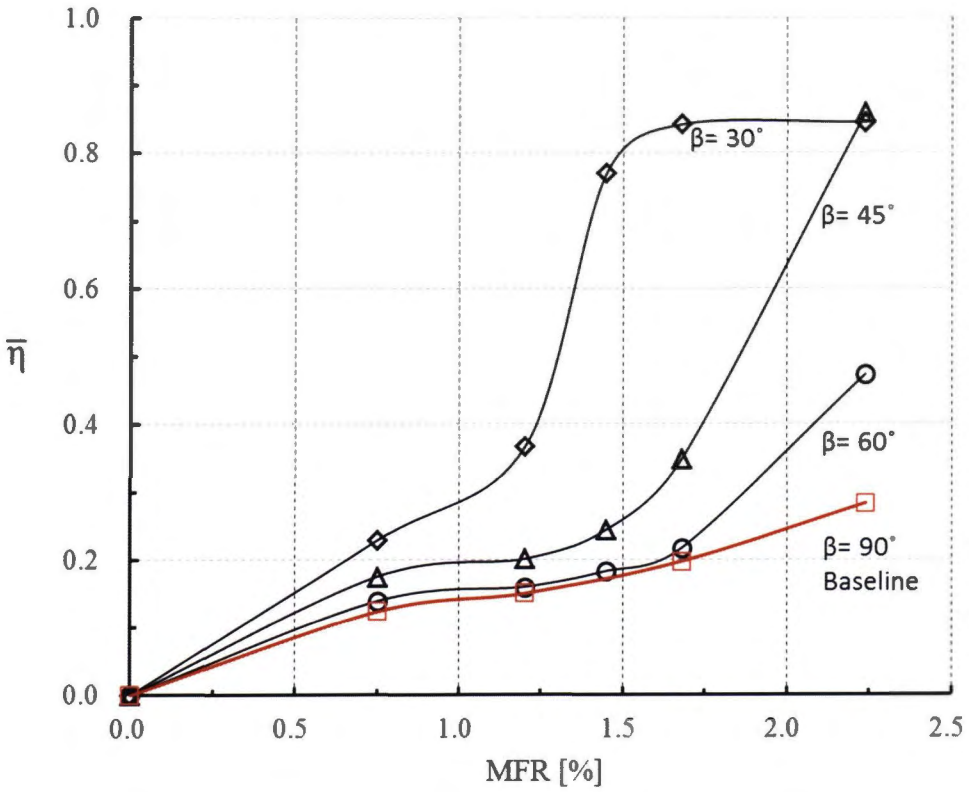

Figure 91 Thermal performance by different β at *l*=-0.63

Thermal performance of the slot based on β is presented in Figure 91 by determine mass-averaged η in comparison with the baseline slot configuration indicated by red line. By β= 60°, there are no significant improvement of η till the MFR was been raised up to 1.75%. At MFR=2.25%, the leakage flow by β= 60°increased the cooling performance approximately 70% relatively to baseline slot configuration. A positive performance trend is predicted when the β was inclined to 45° and 30°. A significant improvement can be observed even though at lower MFR of 0.75% especially approximately 90% of performance increased by β= 30°. At extremely higher injection by MFR=2.25%, slot with β= 30° seems to reach maximum line where the cooling performance is predicted almost the same with β= 45° at $\bar{\eta}$ =0.85. This means the cooling performance increases more than 100% in comparison with the baseline. Since the average has been determined based on fixed endwall area which is starting from x/C_{ax} =-0.63 and ended at x/C_{ax}=1.15 in axial direction, the cooling performance downstream

of fixed area was not counted. Noted that the starting point is actually the position of the slot, l =-0.63. This might be the reason why injection by β= 30°is almost the same with β= 45° as shown in Figure 91.

Figure 92 and Figure 93 present the η contour based on the different β for MFR=1.25% and MFR=2.25%, respectively. The same figure which were presented by Figure 73(a) and 75(a) to illustrates 2 pitches of endwall starting from x/C_{ax} =-0.63 and ended at x/C_{ax}=1.15. Noted that the mass-averaged η presented in Figure 91 was determined based on this area. At MFR=1.25%, no significant increase of the protection layer provided by β= 60° and β= 45° in comparison with baseline injection except the increased level of the η. The leakage injection at this MFR still unable to eliminate or reduce the strength of the PS-HSV which preventing the leakage flow to protect the endwall close to the blade PS region. However, the leakage flow could stay closer to the endwall side due to the less flow separation in comparison with the normal injection case thus resulting higher level of η. By β= 30°, see Figure 92 (c), the level of η further increases and the protection layer has spread towards blade LE and also slightly closer towards blade PS region. This might be due to the reduced strength of the HSV or PS-HSV. As shown in Figure 84~Figure 86, further increases the MFR to 2.25% were predicted to significantly modified the secondary flow structures generated by baseline slot configuration at same MFR. The reduced strength of PS-HSV by β= 60° at MFR=2.25% influenced the leakage flow to further expand the η as shown in Figure 92 (c). Since the strength of PS-HSV has been drastically reduced by β= 45°and β= 30°, the leakage flow can easily reached the blade PS region and whole endwall surfaces was been protected. The higher penetration of leakage flow towards the blade PS by β= 30° compared to β= 45°(see Figure 87) provides slightly higher level of η near this region as shown in Figure 93 (c). Furthermore, higher penetration towards blade PS by β= 30° influenced the leakage flow to stayed closer to the blade PS surface and leave wider protection layer strike as shown in Figure 94. This is also a very interesting thermal performance shown by such slot configuration where this region usually unprotected by normal injection. This caused the endwall region close to the adjacent blade SS obtained lower level of η indicated by a green region since the leakage flow tend to move along the blade PS.

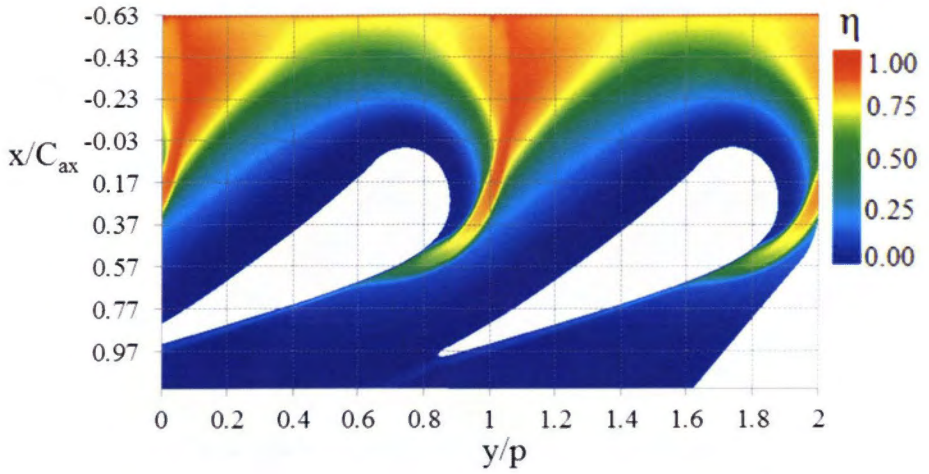

(a) β= 60°

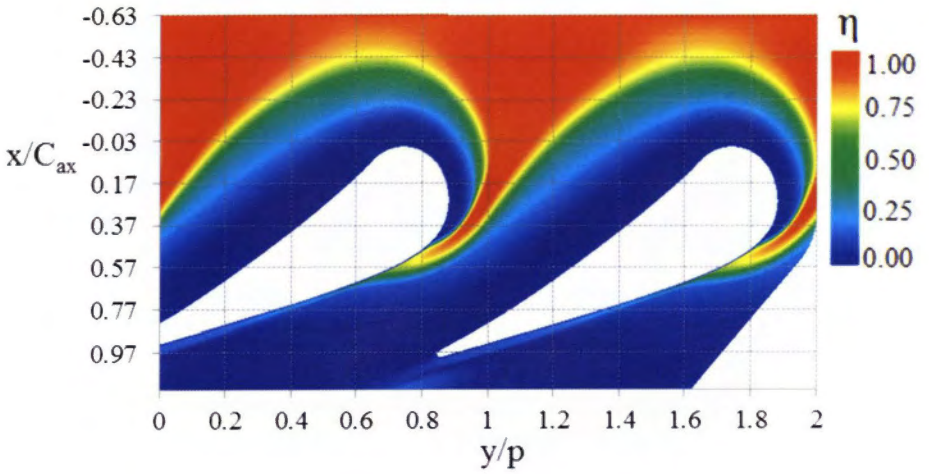

(b) β= 45°

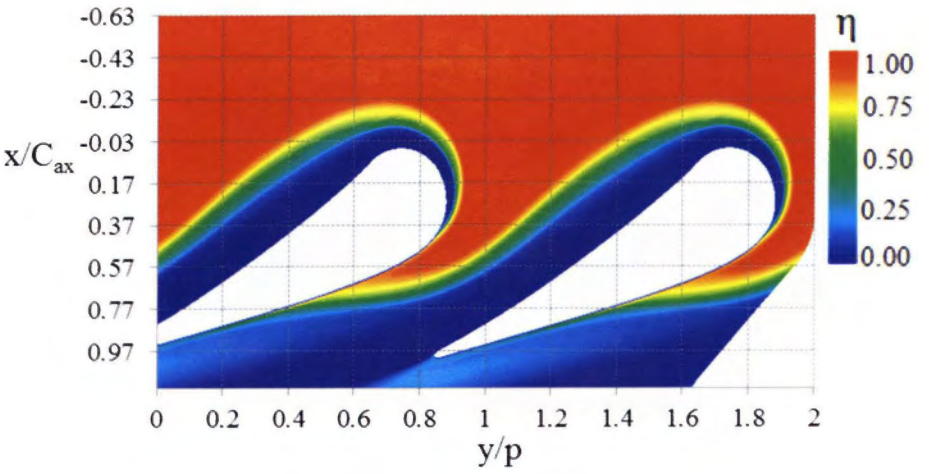

(c) β= 30°

Figure 92 Predicted η contour at MFR=1.25% by three different β

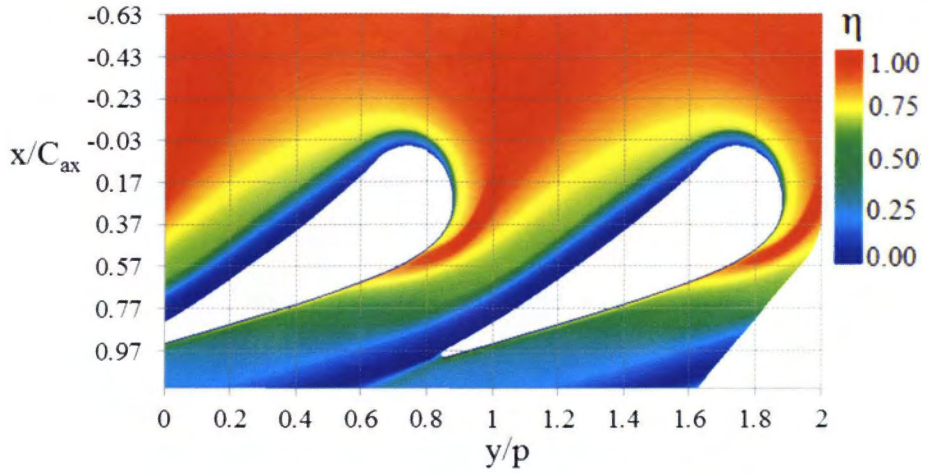

(a)β= 60°

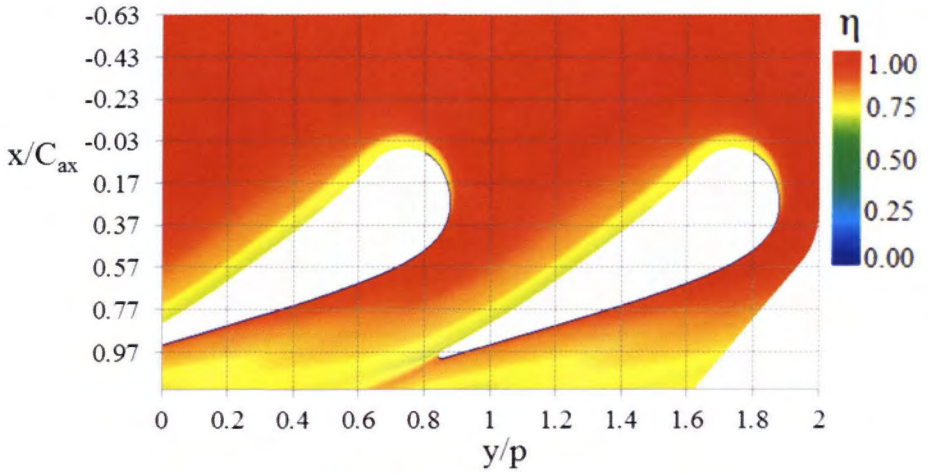

(b)β= 45°

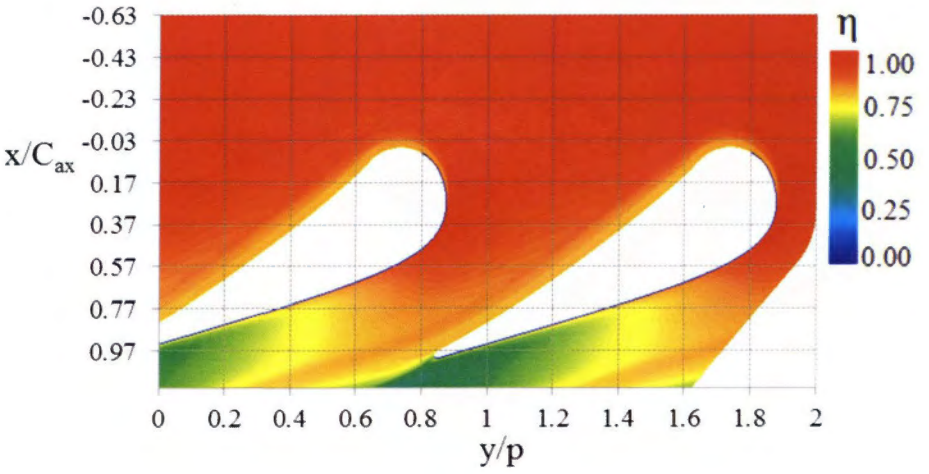

(c)β= 30°

Figure 93 Predicted η contour at MFR=2.25% by three different β

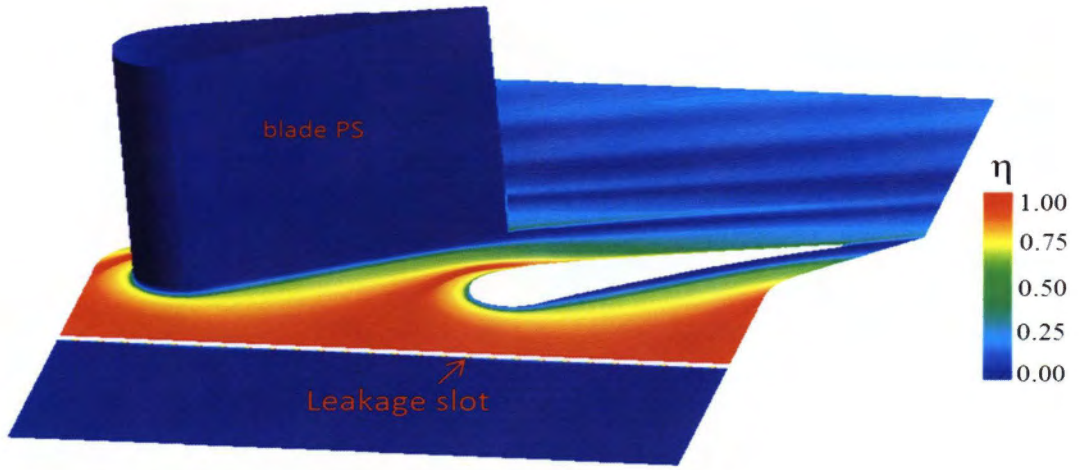

(a) β= 60°

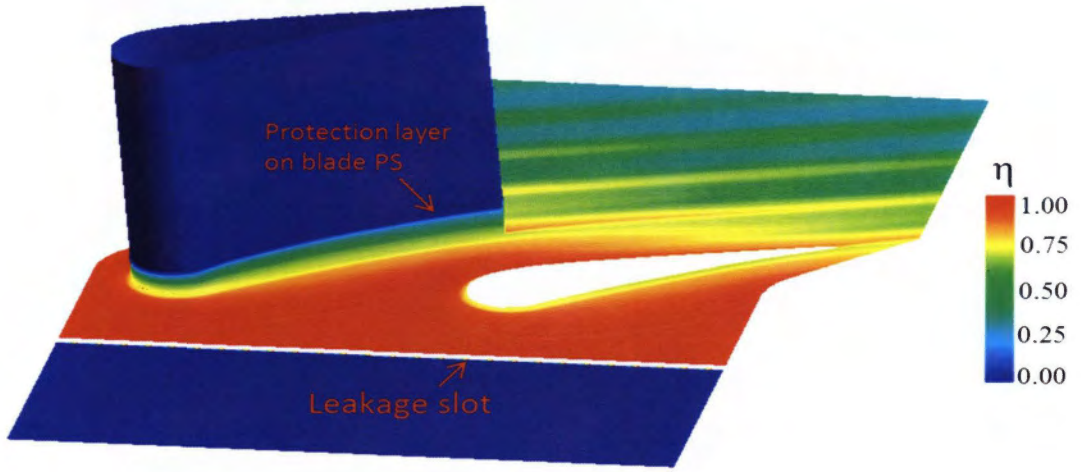

(b) β= 45°

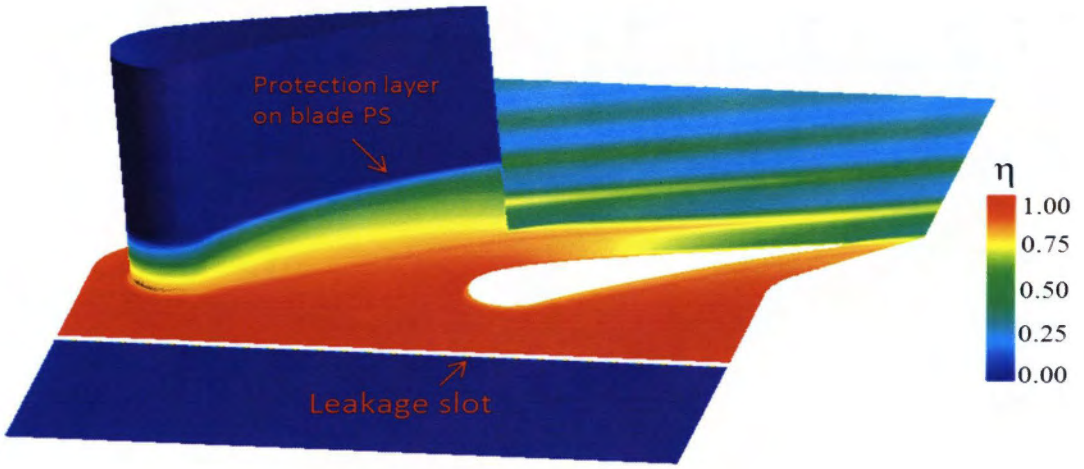

(c) β= 30°

Figure 94 η contour to illustrate the protection layer on the blade PS by different β

4.3 Leakage flow performance influenced by the slot position with $\beta = 90^{\circ}$

4.3.1 Aerodynamics performances

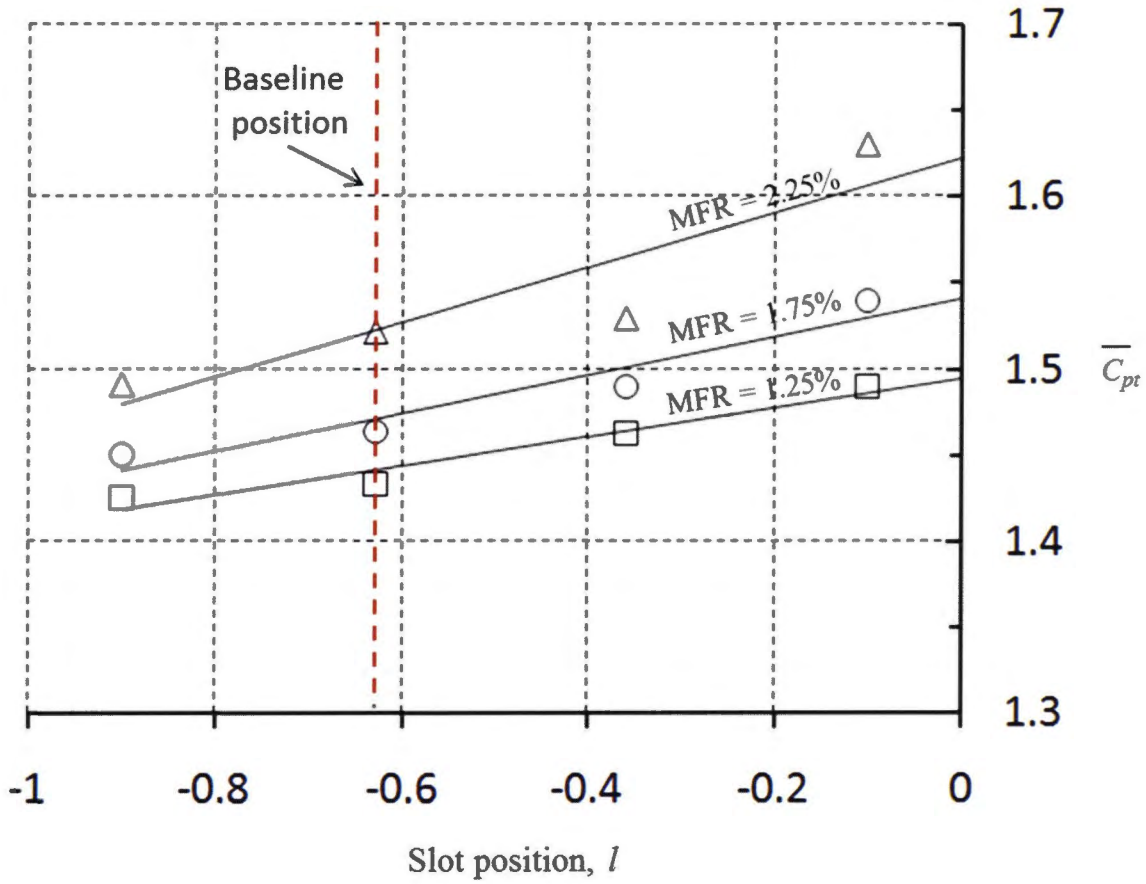

Figure 95 Mass average C_{pt} by the effect of slot location, l

Move the slot away from the blade leading edge had illustrated the increased of cooling performance where the coolant could stay closer to endwall surface thus provided better surface protection [25]. Present study intended to predict the performance of leakage flow injection with a different l from blade LE. l were translated to -0.90, -0.36 and -0.10. Three cases of MFR (1.25%, 1.75% and 2.25%) were predicted at each slot position. Figure 95

presents the loss trend by determined the mass averaged of C_{pt}. The red vertical line illustrates the position of the baseline slot located at l= -0.63. Regardless the l, MFR of 2.25% is always provides the highest loss among the cases. However, as l moved away from the blade LE, the prediction shows that the loss is linearly reduced. This phenomenon also follows by another two cases of MFR=1.75% and 1.25% where the lowest losses were obtained at l= -0.90. This means that l= -0.10 presents the highest loss among the case. The injection of leakage flow closer to the blade LE might be induced to the higher flow blockage which then amplifies the strength of HSV. As a result, the higher loss caused by the secondary flow structures was obtained. Figure 96 presents the C_{pt} contour based on MFR=1.25% in comparison of different l. When the slot moved closer to the blade LE at l= -0.36, the first and third loss cores seem to be increased. Further closer at l= -0.10, see Figure 96 (c), the third core merged with the first loss core resulting wider loss which associated by the PS-HSV. In contrary, in comparison with the baseline slot configuration, see Figure 51 (a), a significant change cannot be seen on the first and third loss cores except the level of C_{pt} slightly reduced.

The details of the secondary flow structure exist in the blade passage are explain by predicted vortex core as shown in Figure 97~Figure 99 for MFR=1.25% by the effect of l. At the same swirling strength level, the strength of the PS-HSV is predicted to be reduced when the slot moved away from the blade LE at l= -0.90 as been shown in Figure 97. In comparison with the baseline slot position, the vortical structures showing by the flow streamline at stagnation plane slightly weaken due to the less flow separation. The leakage flow can easily be penetrated into the mainstream since the slot is far enough from the higher pressure region. As a result, the leakage flow could stayed closer to the endwall surfaces . However, as shown in Figure 100 (a), the leakage flow tends to move towards center of the blade passage further downstream of the slot to generate AFV.

In case for l= -0.36 as shown in Figure 98, the injection near the high pressure region seems preventing the leakage flow to be reattached on the endwall surfaces thus high flow separation occurred just downstream of the slot. A very complicated flow structures has been predicted by the leakage injection at this slot position. To move the slot further downstream at l= -0.10 where the slot is actually located parallel to the higher pressure region at blade LE. Thus, the leakage injection with MFR=1.25% is predicted did not has enough momentum to be penetrated into the stagnation region as being shown by flow streamline at stagnation in

Figure 99. The leakage flow is totally prevented to be penetrated into the higher pressure region thus it tends to swirl inside the slot just upstream of slot exit. They tended to be penetrated near the blade center where the pressure is lower. The formation of the AFV by *l*= -0.36 and *l*= -0.10 cases are also observed in Figure 98 and Figure 99. The secondary flow structures near the blade TE are presented in Figure 101~Figure 103 with the ζ contour plotted on Plane $1.25C_{ax}$. There are almost similar flow structure has been shown by the case at *l*= -0.90 and *l*= -0.36. However the different phenomenon has been shown by *l*=-0.10, the PS-HSV seems to be deflected by the AFV and develop along the passage before be attached on the adjacent blade SS near TE. This is a different phenomenon where in usual case the reattachment of PS-HSV occurs near the blade throat.

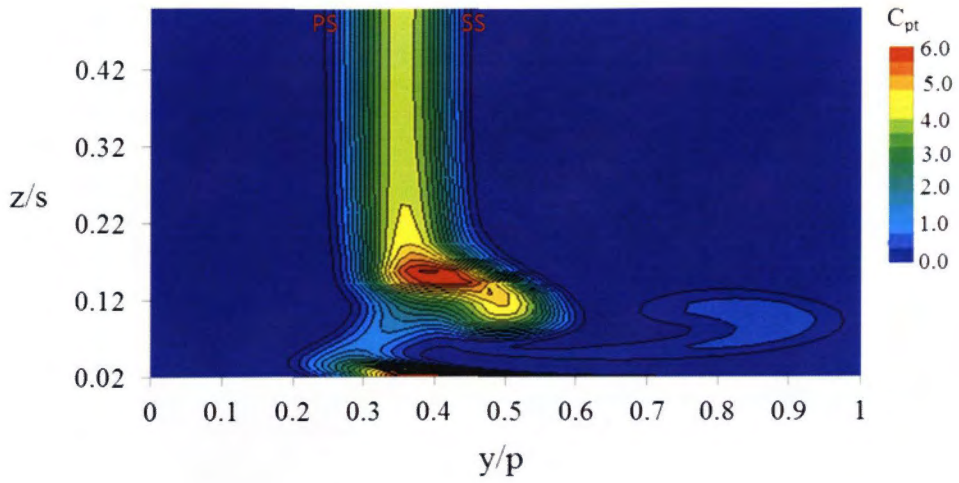

(a) l = -0.90

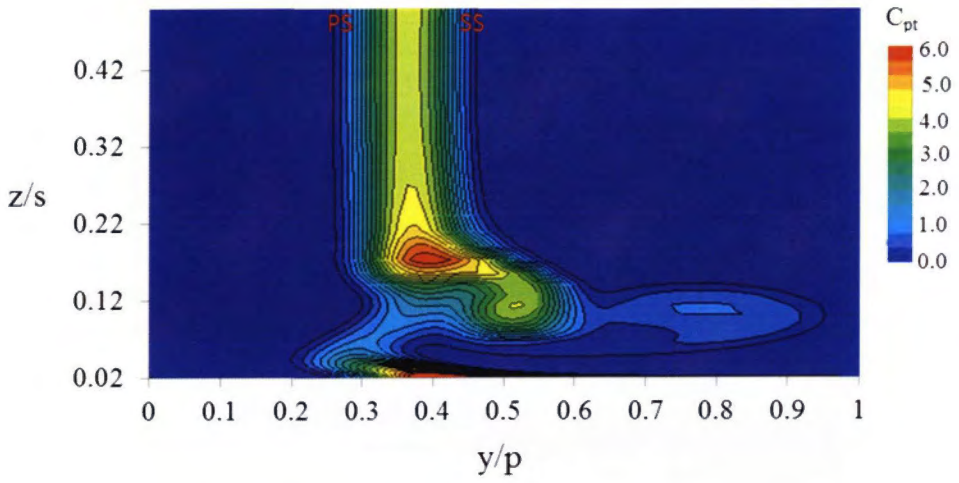

(b) l = -0.36

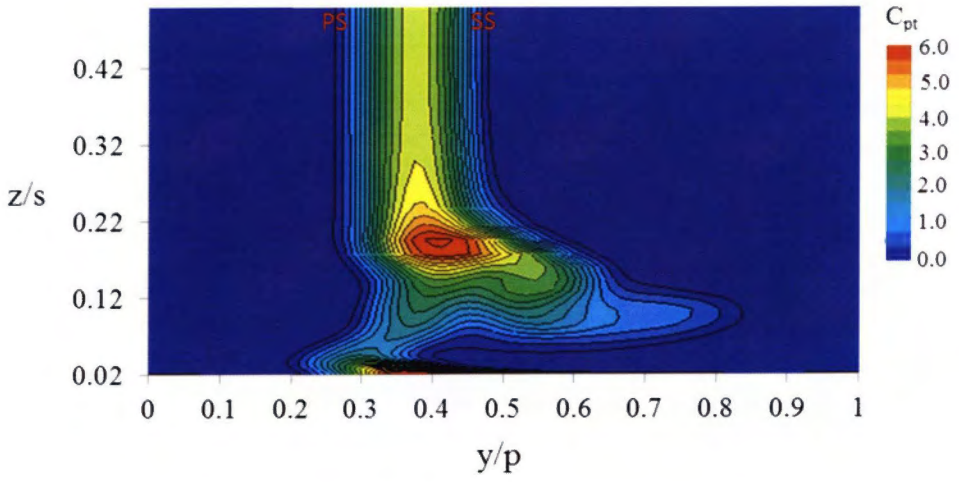

(c) l = -0.10

Figure 96 Predicted C_{pt} contour at MFR-1.25% by three different l

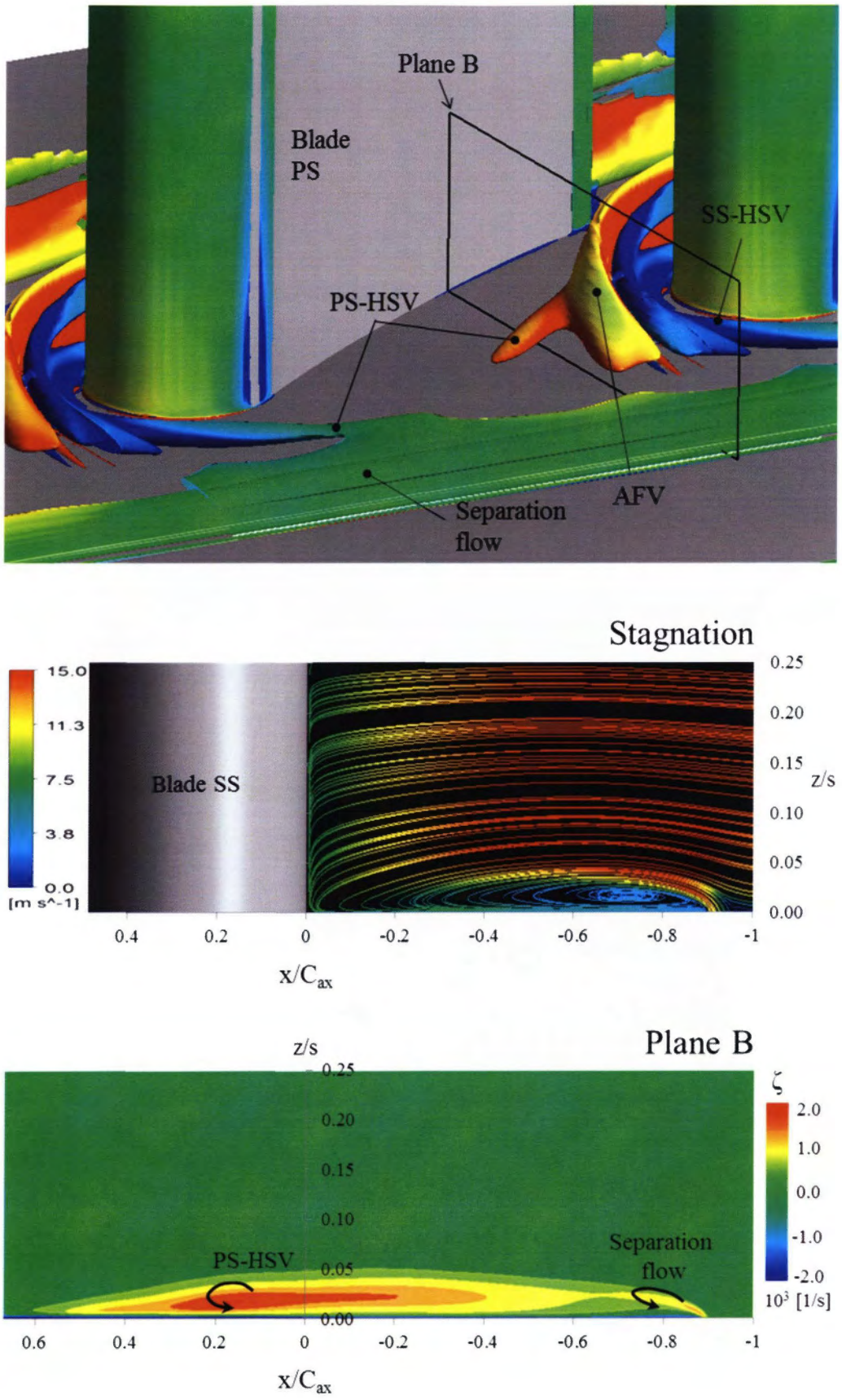

Figure 97 Predicted flow structures near blade LE at MFR=1.25% by i=-0.90

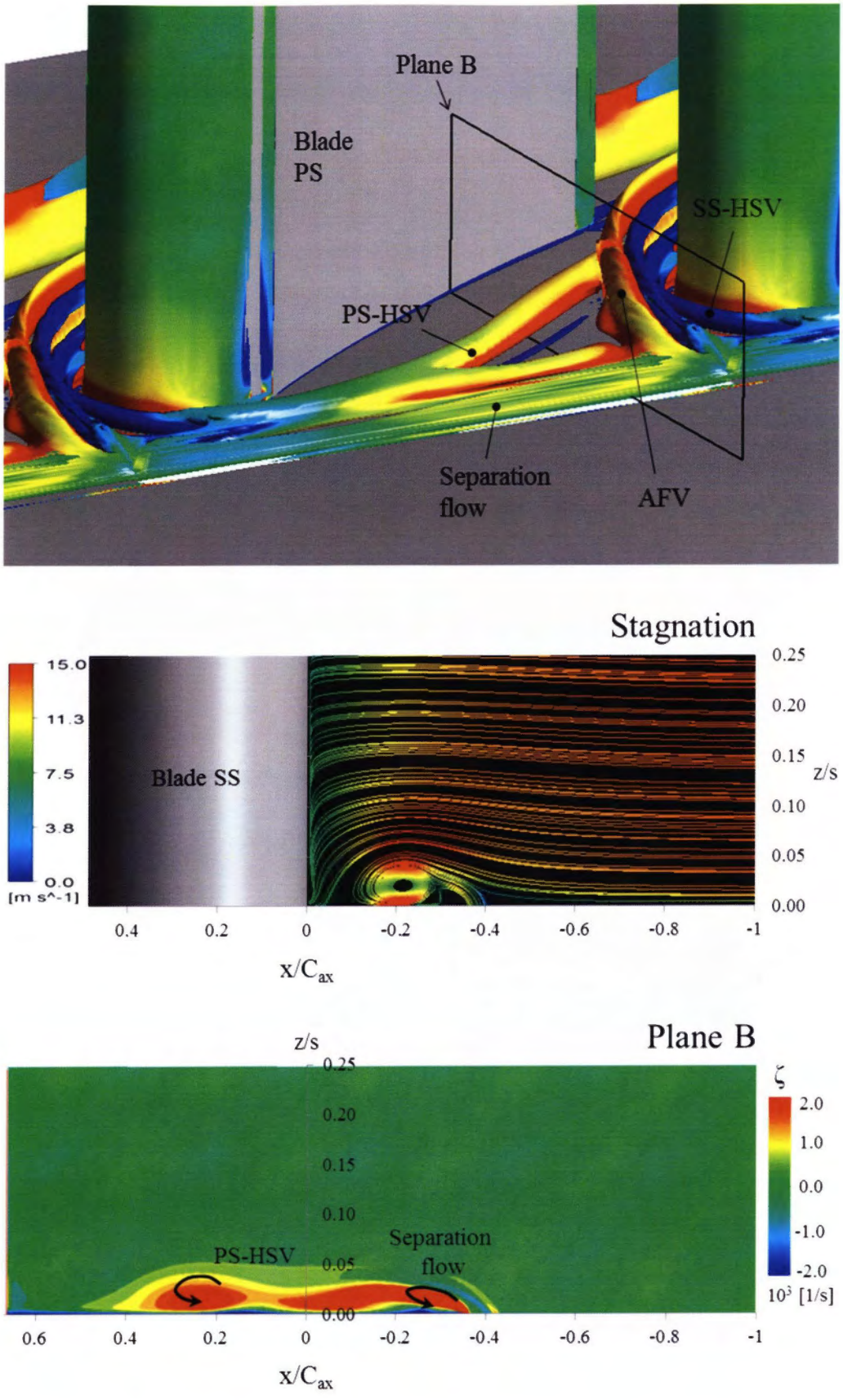

Figure 98 Predicted flow structures near blade LE at MFR=1.25% by l=-0.36

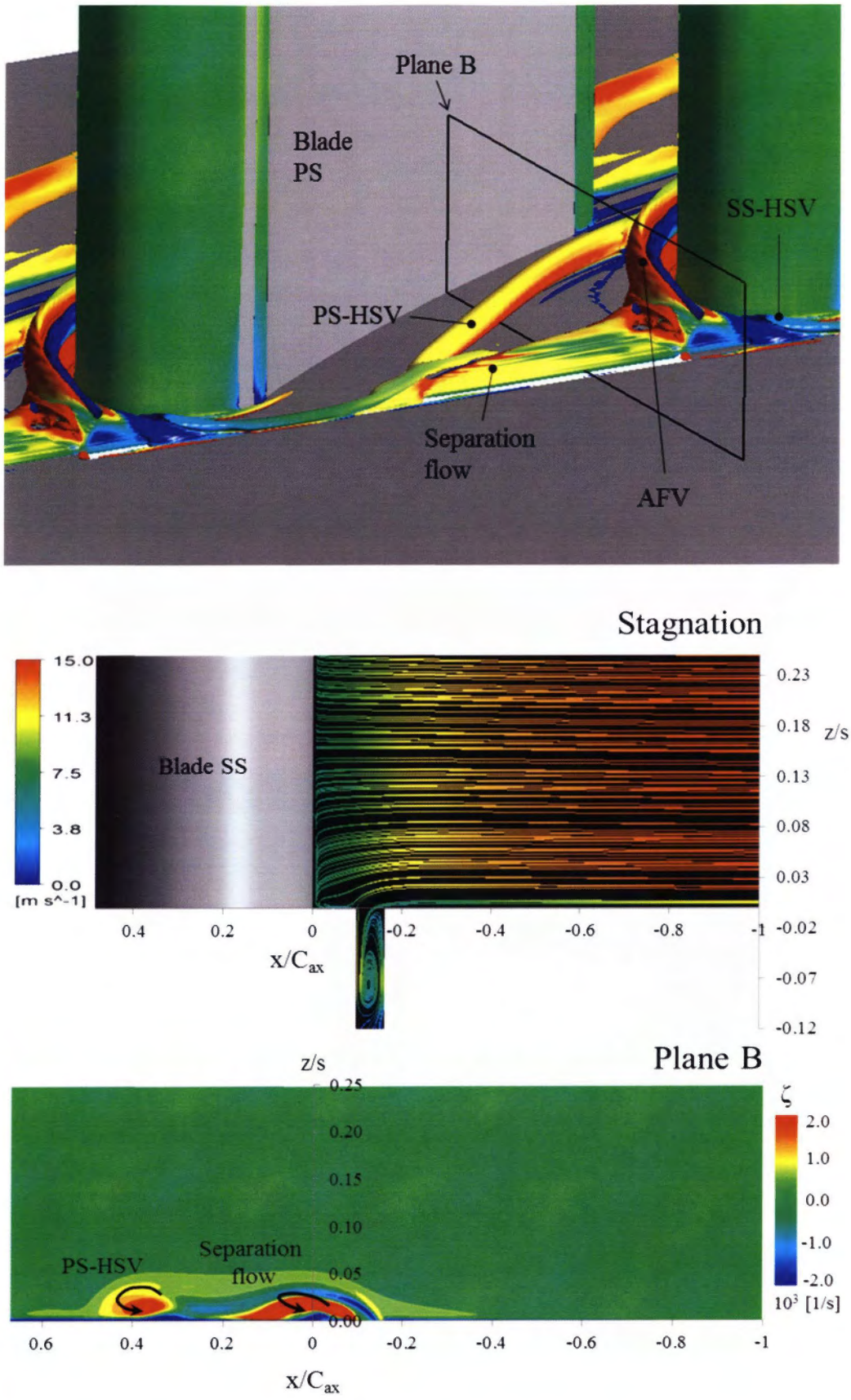

Figure 99 Predicted flow structures near blade LE at MFR=1.25% by i=-0.10

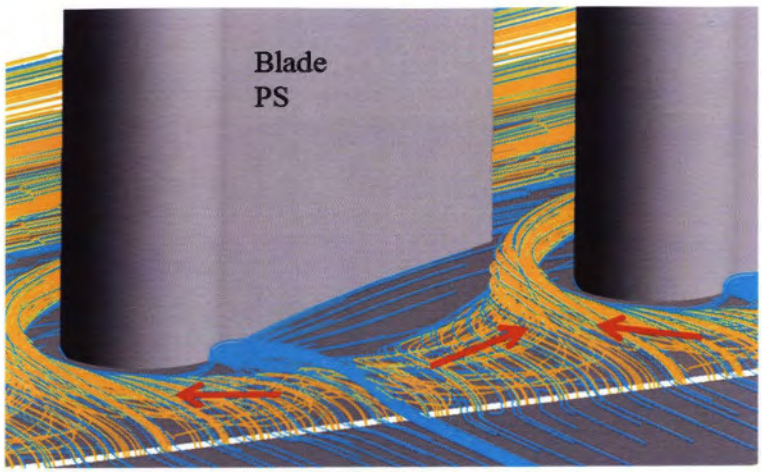

(a) Endwall streamline by l=-0.90

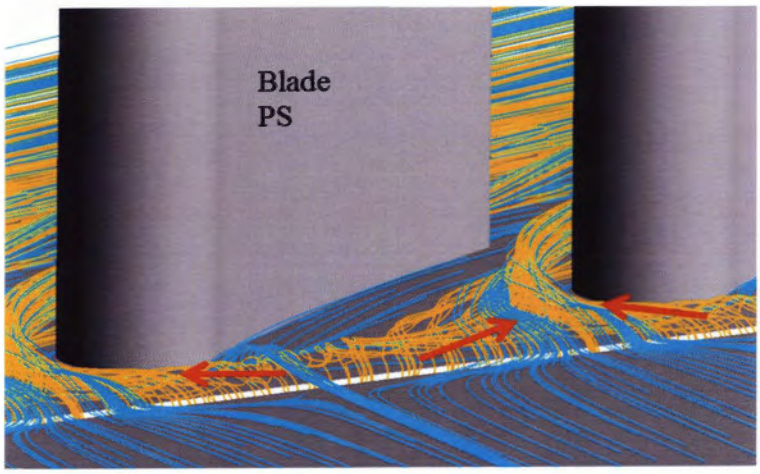

(b) Endwall streamline by l=-0.36

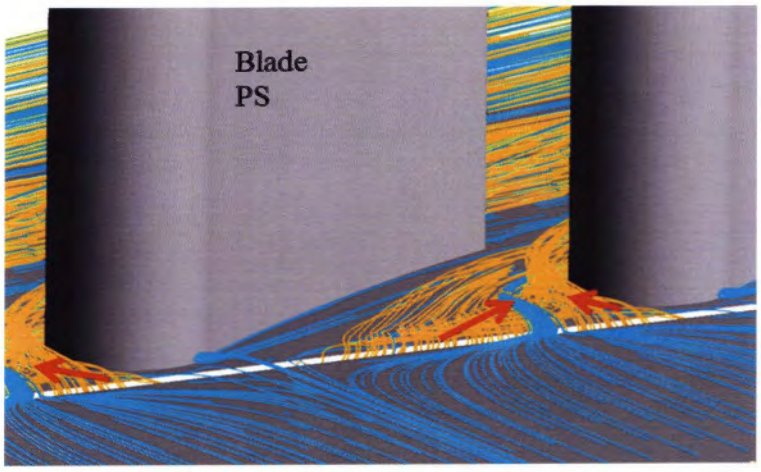

(c) Endwall streamline by l=-0.36

Figure 100 Predicted flow streamline on endwall region by slot position, *l* effect

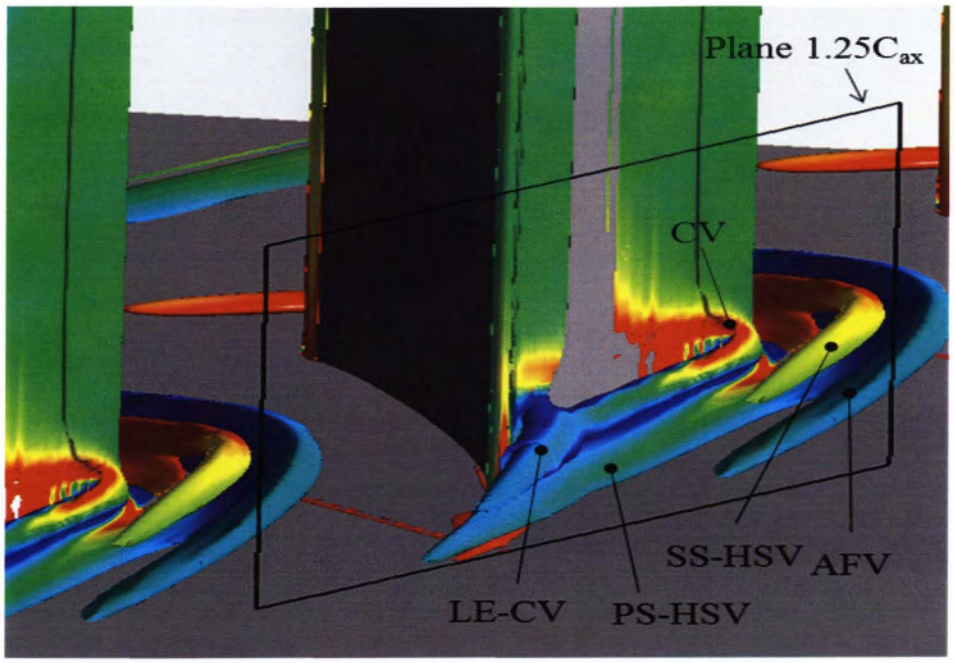

(a) Vortex core

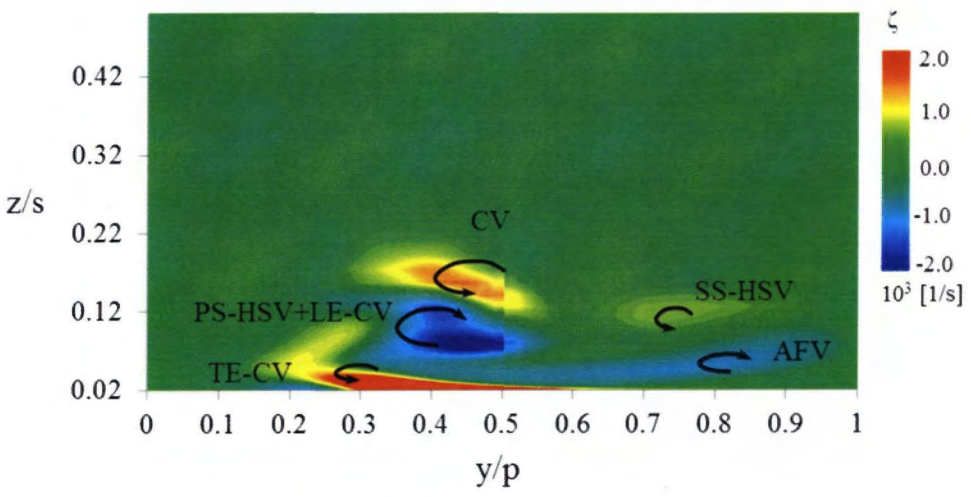

(b) Vorticity at Plane 1.25C$_{ax}$

Figure 101 Predicted flow structures near blade TE at MFR=1.25% by l=-0.90

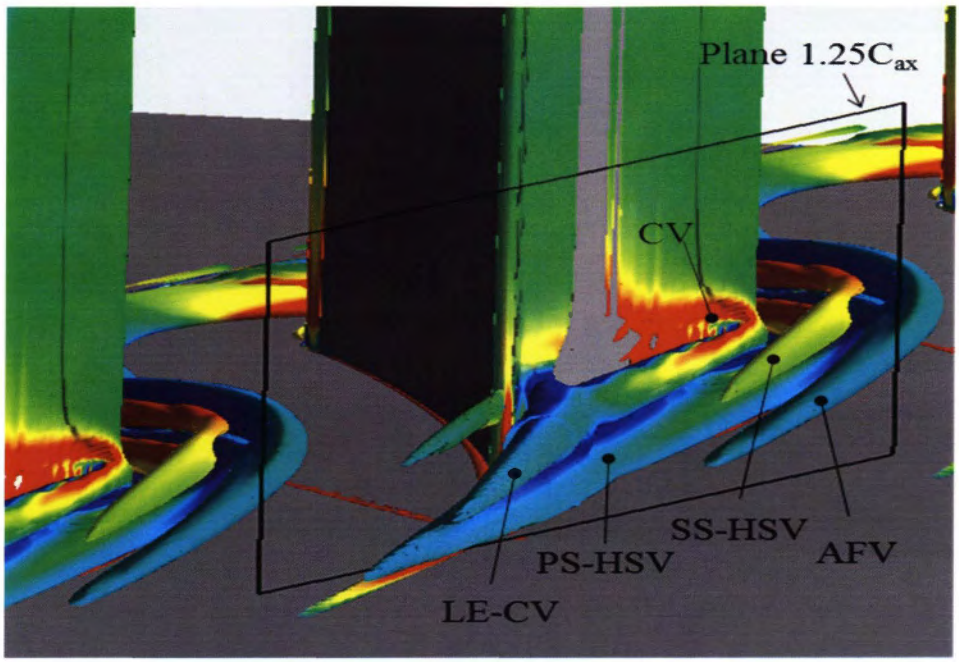

(a) Vortex core

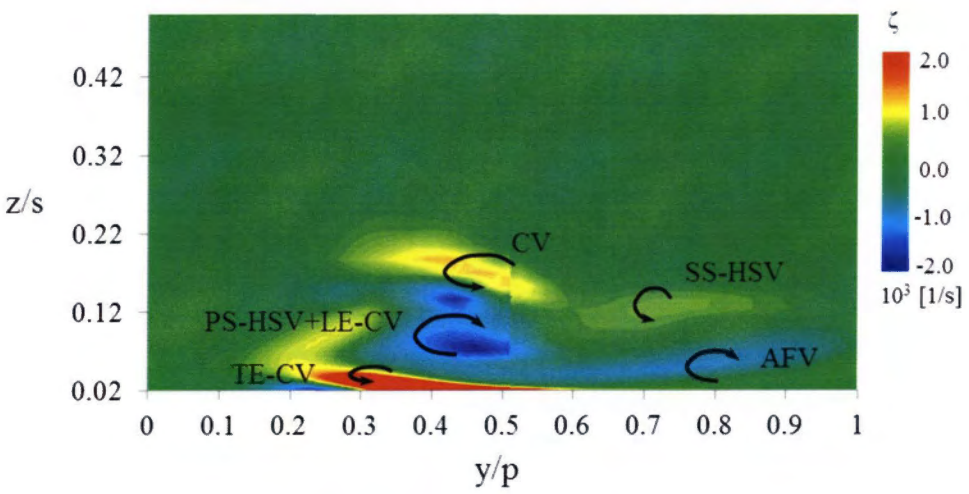

(b) Vorticity at Plane 1.25C$_{ax}$

Figure 102 Predicted flow structures near blade TE at MFR=1.25% by l=-0.36

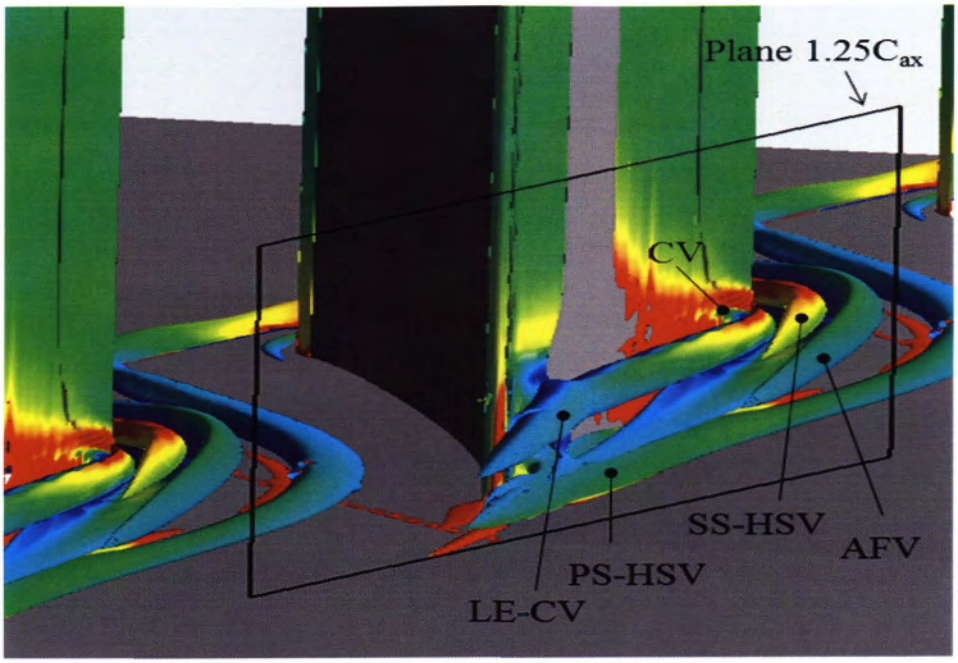

(a) Vortex core

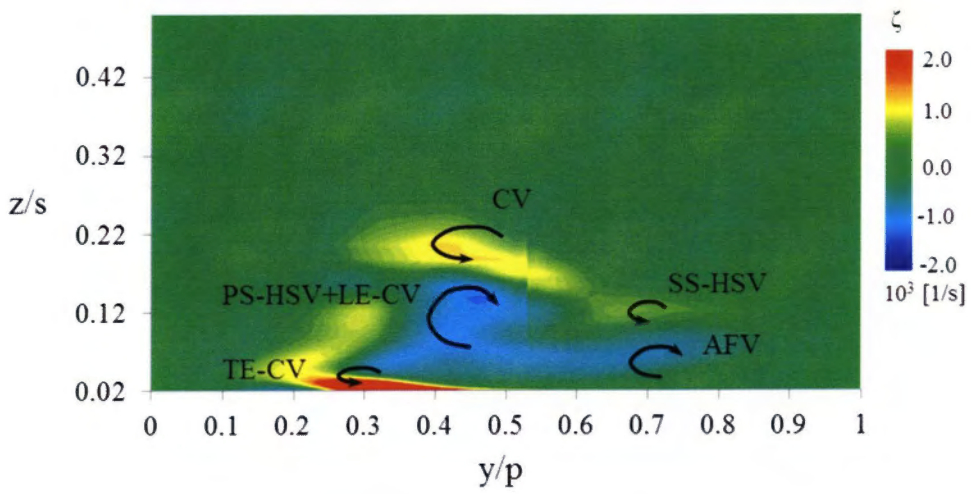

(b) Vorticity at Plane $1.25C_{ax}$

Figure 103 Predicted flow structures near blade TE at MFR=1.25% by l=-0.10

4.3.2 Thermal performances

Figure 104 presents the performance of η at MFR = 1.25% by each slot position, l which is illustrated by the black horizontal line. The change on η contour can clearly be observed. At l=-0.36, η shows slightly lower performance compared to -0.63 where the yellow regions indicates the higher η slightly reduced. Different phenomenon shown by the case of l=-0.10 where the red region indicates a higher level of η became wider near the blade SS. However, the region near to the blade LE almost not be protected by the leakage flow due to the higher blockage caused by the higher pressure in stagnation region. This phenomenon has been shown in Figure 99 where the leakage flow tend to swirl inside the slot instead of the endwall surface resulting unprotected area near this region. This means the leakage flow tends to migrate towards passage center and might be the reason for the higher level of η is observed. In contrast, the level of η clearly increased for the case of, l= -0.90 in comparison with the baseline case. Since the slot located far away from the blade LE compared to other cases, the widest protection region was obtained and the red region which indicates higher η also increases. Moved the slot away from the blade LE allows the coolant to be laterally penetrated and provided much better protection layer. Regardless the position of slot, the region close to the blade PS is remains unprotected even the slot was moved closer. Noted that the higher level of η is presented at the same region where the AFV is generated.

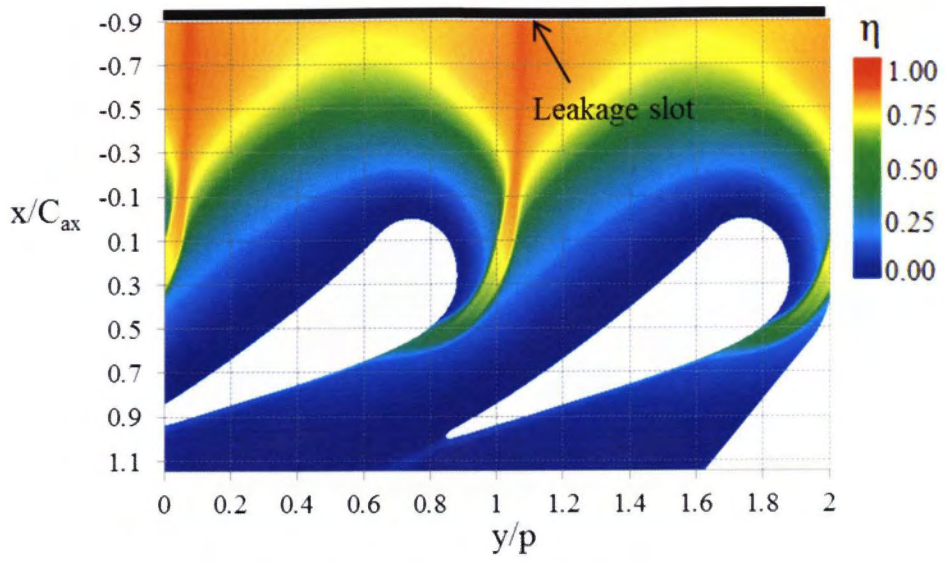
Leakage slot
η
1.00
0.75
0.50
0.25
0.00
x/C_ax
-0.9
-0.7
-0.5
-0.3
-0.1
0.1
0.3
0.5
0.7
0.9
1.1
0
0.2
0.4
0.6
0.8
1
1.2
1.4
1.6
1.8
2
y/p

(a) l = -0.90

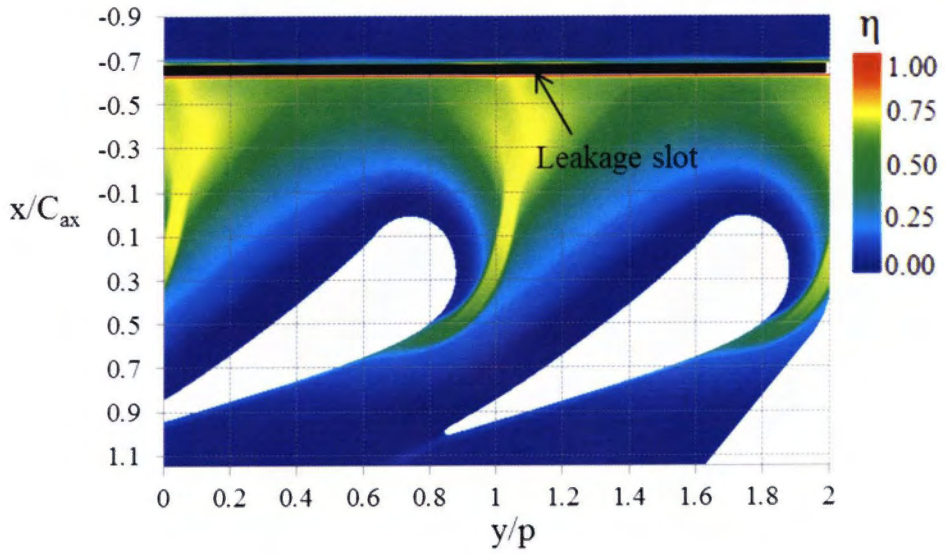
Leakage slot
η
1.00
0.75
0.50
0.25
0.00
x/C_ax
-0.9
-0.7
-0.5
-0.3
-0.1
0.1
0.3
0.5
0.7
0.9
1.1
0
0.2
0.4
0.6
0.8
1
1.2
1.4
1.6
1.8
2
y/p

(b) l = -0.63

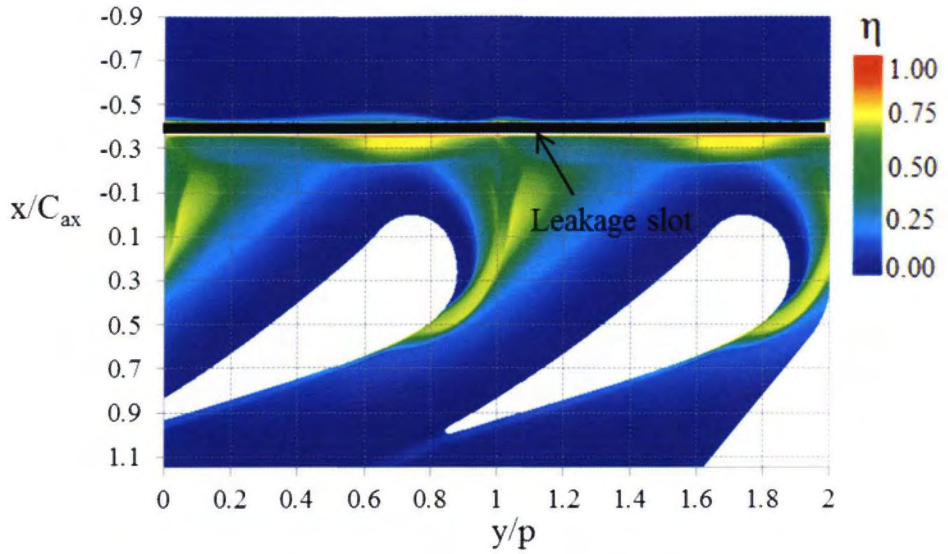

(c) l = -0.36

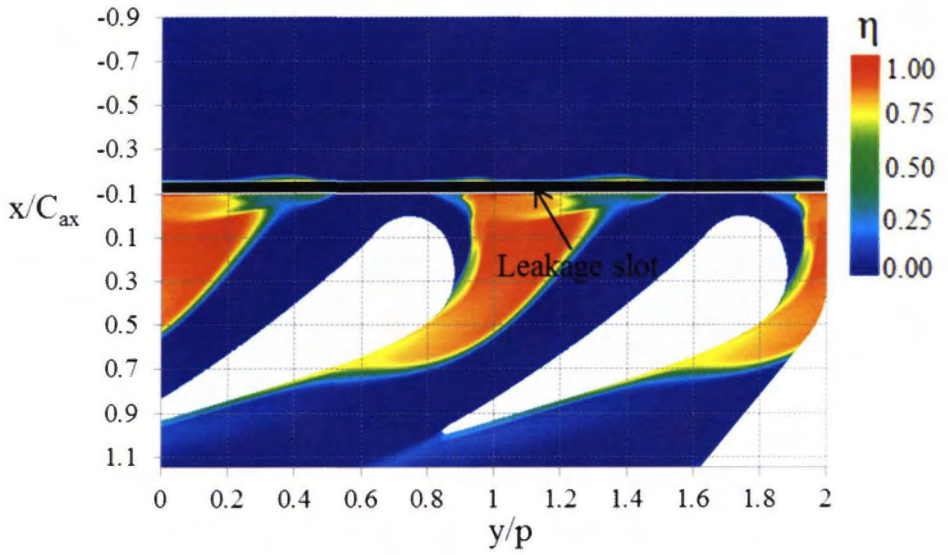

(d) l = -0.10

Figure 104 Predicted film cooling effectiveness contours by slot position effect

4.4 Laterally averaged η by slot modification

The laterally averaged film cooling effectiveness are plotted in Figure 105 by the effect of the slot orientation (β =90° 60°, 45°and 30°) while Figure 106 illustrates the effects of slot position (l=-0.90, -0.63, -0.36 and -0.10). By the effect of β, laterally averaged η significantly increase by the shallower angle. It relatively increases approximately 30% when β is changed to 60°in comparison with normal injection followed by another 20% for β=45°. However, the differences seem to be reduced at further downstream of the passage especially just downstream of blade throat at x/C_{ax}=0.6 where for β =90°, 60°and 45° are almost the same level. Different performance by β =30° where it always higher than others along the passage. At x/C_{ax}=0.6, the performance slightly raised for the whole cases might be due to the vortex core which was mixed out with the leakage flow was deflected towards endwall surface by the LE-CV near the blade throat thus higher η is obtained.

Since the positions of slot are differing in Figure 106, the starting point of the curve is different. If the comparison is made starting from x/C_{ax}=-0.30, the performance illustrated by the case of l=-0.9, -0.63 and -0.36 are almost the same where η is approximately 0.5. Positioned the slot further away from this point continuously increased the performance as shown by the case of l=-0.90 and -0.63. By l=-0.10, relatively higher performance has been shown compared to others. The leakage flow coming from this slot location could provide higher temperature different compared with others which were already mixed out with the mainstream. The mixed out flow would have relatively lower temperature than the leakage flow. Based on the thermal performance show by whole cases, to change the slot injection angle is considered as the most effective way to improve the cooling compared to the slot position. Furthermore, there are very limited space between the combustor and high-pressure turbine endwall if the position of slot is considered

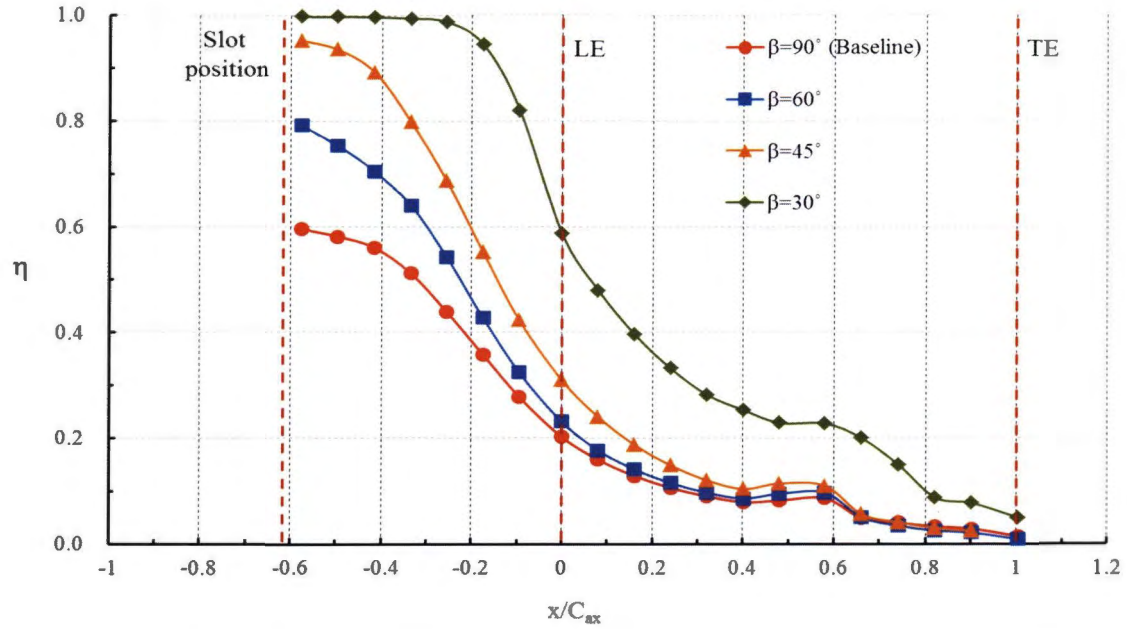

Figure 105 Laterally averaged film cooling effectiveness at MFR=1.25% by slot orientation, β effect

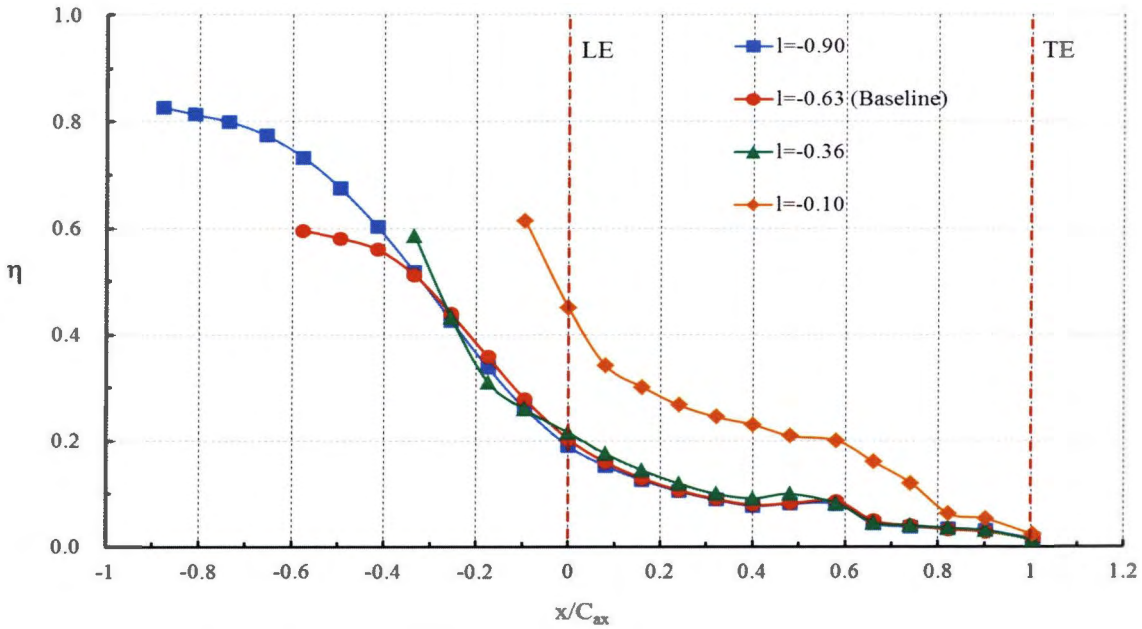

Figure 106 Laterally averaged film cooling effectiveness at MFR=1.25% by slot position, *l* effect

Chapter 5

Conclusions

The potential of leakage flows through a baseline slot configuration (90° injection at l= -0.63) to work as a cooling in order to protect the endwall surfaces in high pressure turbine cascade has been investigated. The measurement by 5-holes Pitot tube enables the clarification of three-dimensional flow behavior with the C_{pt} and ζ contours plotted. As for the thermal investigation, the TLC layer coating on the endwall surfaces allowed the detecting of temperature different and the transient method was applied to determine h and η. The capability of numerical simulation was also investigated by the validation with the experimental results. Authors also have taken the advantage of numerical simulation to predict the effects on aero-thermal performance by changing the slot configuration in terms of positions and orientations. Based on the results obtained, the following conclusions can be drawn:

- Both EFD and CFD represent almost similar trend of performance and enable authors to take advantage of numerical simulation to accurately predict the interaction of ejected leakage flow with the main stream. Leakage flow has significantly affected the secondary flow fields. Based on tested MFR, this loss region expanded approximately 40%-50% of area. MFR=2.25% was contributed to the highest loss among others. The newly generated vortical structures have been captured by the CFD with a higher swirling strength travel along the blade SS, which consequently contributed to the additional losses
- The loss core which was indicated in the baseline case was also affected by the leakage injection. Injecting the leakage flow from the blade upstream was predicted to amplify the strength of PS HSV so that it lifted-off adjacent blade SS with slightly higher position resulting higher loss core position in spanwise direction The mass-averaged

total pressure loss was proportional to the MFR and the graph plotted enable the authors to estimate the loss providing with another case of MFR. CFD over predicted the loss approximately 3% to 5% compared to the measurement.

- The discrepancy between CFD and EFD in terms of shape and position of the loss core was predicted associated by the flow behavior inside the plenum chamber. It was predicted to provide a significant effect of the formation of AFV on the endwall which consequently presented a difference loss contour.
- Film cooling effectiveness increases as to MFR, at the rate of at least 50% of the region for every 0.5% increase of MFR. Area averaged film cooling effectiveness increases approximately 7% whereas CFD predicted about 12% for 1% increase of MFR. This was due to the smaller temperature measurement range and the heat loss phenomenon during the temperature measurement. The thermal performance on the endwall region was also highly influenced the secondary flows behavior in providing the cooling protection area. SST turbulence model captured the presence of flow separation caused a lower HTC region on endwall surface which was also captured by the experimental especially for the MFR = 1.75% case.
- The injection of leakage flow at higher MFR of 2.25% through the inclined slot angle was predicted to reduce the strength of the secondary flow vortices near endwall. As a result, at fixed MFR=2.25%, injection with $\beta=30^{\circ}$ contributed the lowest averaged loss among cases. The performance of leakage flow through a shallow injection angle not only reduce the loss, but also was predicted to provide the wider cooling layer with higher η on the endwall surfaces. Blade PS and SS near the endwall corner were also protected by the slot configuration of $\beta=30^{\circ}$ and 45°
- Positioned the slot at l=-0.90 could provide a better cooling performance with a less secondary loss effects. At MFR=1.25%, the loss was predicted to reduce approximately 1.0% after changing the position of slot from l=-0.63 to -0.90. However, it was increased approximately 2.0% and 4.0% after shifted the slot closer towards blade LE at l=-0.36 and l=-0.10, respectively. Predicted film cooling effectiveness also indicates a positive trend of contour at l=-0.90. The wider protection area has been provided after moved the slot away from blade LE.
- The prediction presented that to change the slot orientation was the most effective way in order to increase both aero and thermal performance of in high-pressure turbine.

References

[1] Denton, J.D. "Loss mechanisms in turbomachines". ASME Paper No. 93-GT-435, 1993

[2] Hawthorne, W.R. "Some formulae for the calculation of secondary flows in cascades." Aero. Research Council, Report No. 17519, 1955.

[3] Sieverding, C. H.; 1984 "Recent Progress in the Understanding of Basic Aspects of Secondary Flows in Turbine Blade Passages", ASME Paper No. 84-GT-78, ASME Journal of Engineering for Gas Turbines and Power, Vol. 107, pp. 248-257

[4] Klein, A. Unterschungen uber den Einfluss der Zustromgrenzschicht auf die Sekundarstromung in den Beschaufelungen von Axialturbinen. Forsch. Ing., Bd 32, Nr 6, 1966; English translation: "Investigation of the entry boundary layer on the secondary flows in the blading of axial turbines. BHRA T 1004, 1966.

[5] Langston, L.S., Nice, M.L. and Hooper, R.M. "Three-dimensional flow within a turbine passage", Journal of Engineering for Power, Vol. 99, pp. 21-28, 1977.

[6] Georgiou, D.P., Papavasilopoulos, V.A. and Alevisos, M. "Experimental contribution on the significance and the control by transverse injection of the horseshoe vortex", ASME Paper No. 96-GT255,1996

[7] Sharma, O.P. and Butler, T.L. "Predictions of endwall losses and secondary flows in axial flow turbine cascades", ASME Paper No. 86-GT-228, 1986.

[8] Goldstein, R.J. and Spores, R.A. "Turbulent transport on the endwall in the region between adjacent turbine blades", Transactions of the ASME, Journal of Heat Transfer, Vol. 110, pp. 862-869, 1988

[9] Sharma, O. P. and Butler, T. L.; 1986 "Prediction of Endwall Losses and Secondary Flows in Axial Flow Turbine Cascades", ASME Paper No. 86-GT-228, Dusseldorf, West Germany.

[10] Wang, H. P., Olson, S. J., Goldstein, R. J. and Eckert, E. R. G.; 1995 "Flow Visualisation in a Linear Turbine Cascade of High Performance Turbine Blades", ASME Paper No. 95-GT-7, Houston, Texas

[11] Gregory-Smith, G.G. and Graves, C.P. "Secondary flows and losses in a turbine cascade", AGARD Paper CP351 No. 17, 1983.

[12] Abdulla-Altaii, A.K. and Raj, R.S. "Secondary flow development downstream of a blade endwall corner", ASME Paper No. 94-GT-459, 1994.

[13] Yamamoto, A., Kaba, K. and Matsunuma, T. "Measurement and visualisation of three-dimensional flows in a linear turbine cascade", ASME Paper No. 95-GT-341, 1995.

[14] Moore, J. and Adhye, R.Y. "Secondary flows and losses downstream of a turbine cascade", ASME Paper No. 85-GT-64, 1985.

[15] Gregory-Smith, D.G. "Secondary flows and losses in axial flow turbines", ASME Paper No. 82-GT19, 1982.

[16] Kang, M. B. and Thole, K.A., 1999 "Flowfield Measurements in theEndwall Region of a Stator Vane", ASME Paper No. 99-GT-188, ASME Journal of Turbomachinery, Vol. 122, pp. 255-262

[17] Radomsky, R. W. and Thole, K. A., 2000, "High Freestream Turbulence Effects on Endwall Heat Transfer for a Gas Turbine Stator Vane ", 122, pp. 699-708.

[18] Sundaram, N. and Thole, K. A., 2009, "Film-Cooling Flow fields with Trenched Holes on an Endwall", Journal of Turbomachinery, 131, pp.

[19] H.J.Rehder, A.Dannhauer, "Experimental Investigation of Turbine Leakage Flows on the Three-Dimensional Flow Field and Endwall Heat Transfer", Journal of Tur bomach, Vol.129, 2007, pp. 608-618

[20] A.A. Thrift,K.A.Thole, S. Hada, 2011,"Effects of Orientation and Position of the Combustor-Turbine Interface on the Cooling of a Vane Endwall", ASME 2011, GT2011-455

[21] Blair, M.F., 1974, "An Experimental Study of Heat Transer and Film Cooling on Large-Scale Turbine Endwalls", ASME Journal of Heat Transfer, Vol. 96, pp. 524-529.

[22] Takeishi, K., Matsuura, M., Aoki, S. and Sato, T.; 1990 "An Experimental Study of Heat Transfer and Film Cooling on Low Aspect Ratio Turbine Nozzles", ASME Paper No. 89-GT-187, ASME Journal of Turbomachinery, Vol. 112, pp. 488-496.

[23] Blair, M. F.; 1992 "An Experimental Study of Heat Transfer in a Large-Scale Turbine Rotor Passage", ASME Paper No. 92-GT-195, Cologne, Germany

[24] Kost, F., and Nicklas, M., 2001. "Film-Cooled Turbine Endwall in a Transonic Flow Field: Part I - Aerodynamic Measurements," ASME J Turbomach 123, pp. 709–719

[25] Kost, F., and Mullaert, A., 2006. "Migration of Film-Coolant from Slot and Hole Ejection at a Turbine Vane Endwall", GT2006-90355

[26] S.P.Lynch,K.A.Thole, "The Effect of Combustor-Turbine Interface Gap Leakage on the Endwall Heat Transfer for a Nozzle Guide Vane", Journal of Turbomachinery,

Vol.130, 2008, pp041019-1-041019-10

[27] Kang, M. B., Kohli, A., and Thole, K. A., 1999, "Heat Transfer and Flowfield Measurements in the Leading Edge Region of a Stator Vane Endwall", Journal of Turbomachinery, 121, pp. 558-568.

[28] J.D.Piggush,T.W.Simon, "Heat Transfer Measurements in a First-Stage Nozzle Cascade Having Endwall Contouring Misalignment and Leakage Studies", Transaction of ASME Vol.129,2007, pp. 782-790

[29] W.G. Aizon, K. Funazaki, 2012, "Aero-Thermal Performance of Purge Flow in Turbine Cascade Endwall Cooling", Applied Mechanics and Material, Vol.229-231,pp.737-741

[30] Funazaki, K., 2000, "Discussion on Accuracy of Transient Heat Transfer Measurement by Use of Thermochromic Liquid Crystal," Journal of the Gas Turbine Society of Japan, Vol. 28, pp. 397-404.

[31] Kline, S.J. (1985a), "The purposes of uncertainty analysis. Journal of Fluids Engineering", Transactions of the ASME, June 1985

[32] Coleman, H.W., and Steele, W.G. (1999). "Experimentation and Uncertainty Analysis for Engineers", 2nd Ed., John Wiley & Sons, New York, pp. 275

[33] Moffat, R.J. (1985)."Using uncertainty analysis in the planning of an experiment", Journal of Fluids Engineering, Vol. 107, No. 6, pp. 173-178.

[34] Alok, D., "Film cooling from a row of holes supplemented with anti-vortex holes", 2007.

[35] http://gehonda.com/products/hf120/explore.html
Last access: September 12, 2013

[36] Genrup, M.; 2005, "On Degradation and Monitoring Tools for Gas and Steam Turbines", Department of Heat and Power Engineering, Lund Institute of Technology, Lund, Sweden, ISRN LUTMDN/TMHP--05/1027--SE.

[37] Han, J.C., Dutta, S., and Ekkad, S. V., 2000, Gas Turbine Heat Transfer and Cooling Technology,

[38] Taylor & Francis, New York. Frank G. R, 2006, "Numerical and Experimental Investigations of Design Parameters Defining Gas Turbine Nozzle Guide Vane Endwall Heat Transfer", pg. 53, Doctoral thesis, Royal Institute of Technology, Stockholm.